STUDIES ON PREPARATION AND CHARACTERIZATION OF SOME YTTERBIUM SUBSTITUTED ZIRCONATES AND THORATES

By

M. BOOTHARAJAN

Enrolment No: CHEM 02 2012 04 003

Indira Gandhi Centre for Atomic Research
Kalpakkam

A thesis submitted to the
Board of Studies in Chemical Sciences
in partial fulfillment of requirements
for the Degree of
DOCTOR OF PHILOSOPHY
of
HOMI BHABHA NATIONAL INSTITUTE

August, 2018

Homi Bhabha National Institute

Recommendations of the Viva Voce Committee

As members of the Viva Voce Committee, we certify that we have read the dissertation prepared by **M. Bootharajan** entitled **"Studies on preparation and characterization of some ytterbium substituted zirconates and thorates"** and recommend that it may be accepted as fulfilling the thesis requirement for the award of Degree of Doctor of Philosophy.

N.V. Chandra Shekar — 22.02.2019

Chairman - Dr. N.V. Chandra Shekar — **Date:**

V. Jayaraman — 22.02.19

Guide / Convener - Dr. V. Jayaraman — **Date:**

22.02.19

Examiner - Roy Ganesh S. Pala — **Date:**

Member 1- Dr. K.I. Gnanasekar — **Date:** 22.02.2019

Member 2- Dr. H.N. Jena — **Date:** 22.02.19

Technology Advisor- Dr. R. Kumar — **Date :** 22.02.19

R. Kumar

Final approval and acceptance of this thesis is contingent upon the candidate's submission of the final copies of the thesis to HBNI.

I/We hereby certify that I/we have read this thesis prepared under my/our direction and recommend that it may be accepted as fulfilling the thesis requirement.

Date: 22.02.2019

Place: Kalpakkam.

V. Jayaraman

Guide

STATEMENT BY AUTHOR

This dissertation has been submitted in partial fulfillment of requirements for an advanced degree at Homi Bhabha National Institute (HBNI) and is deposited in the Library to be made available to borrowers under rules of the HBNI.

Brief quotations from this dissertation are allowable without special permission, provided that accurate acknowledgement of source is made. Requests for permission for extended quotation from or reproduction of this manuscript in whole or in part may be granted by the Competent Authority of HBNI when in his or her judgment the proposed use of the material is in the interests of scholarship. In all other instances, however, permission must be obtained from the author.

22/02/19

M. Bootharajan

DECLARATION

I, hereby declare that the investigation presented in the thesis has been carried out by me. The work is original and has not been submitted earlier as a whole or in part for a degree / diploma at this or any other Institution / University.

22/02/19

M. Bootharajan

List of Publications arising from the thesis

Journal

1. "Behavior of Ytterbium in Calcium and Strontium Zirconate Matrices", **M. Bootharajan**, J. S. Brahmaji Rao, R. Kumar, and V. Jayaraman; ECS Journal of Solid State Science and Technology, 6 (2017) N10-N16.
2. "Synthesis, characterization and electrical conductivity of $BaTh_{1-x}Yb_xO_{3-x/2}$", **M. Bootharajan,** R. Kumar, V. Jayaraman ; Ceramics International 44 (2018) 11172–11179
3. "Electrical conductivity and chemical stability of pure and Zr substituted $BaThO_3$", **M. Bootharajan**, R. Kumar, V. Jayaraman; Ceramics International 44 (2018) 20192 - 20198
4. "Determination of stoichiometry of ytterbium substituted $SrZrO_3$ using neutron activation analysis" **M. Bootharajan**, J. S. Brahmaji Rao, R. Kumar, and V. Jayaraman, Manuscript under preparation.
5. "$SrZr_{0.95}Yb_{0.05}O_{2.975}$ as proton conducting membrane for separation of hydrogen from argon at intermediate temperature" **M. Bootharajan**, R. Kumar, V. Jayaraman, Manuscript under preparation.
6. "Hydrogen retention behaviour in ytterbium substituted zirconates and thorates" **M. Bootharajan**, R. Kumar, V. Jayaraman, Manuscript under preparation.

Conferences

1. "Synthesis and Characterization of $CaZr_{1-x}Yb_xO_{3-\delta}$ - High temperature Proton conductors", **M. Bootharajan**, R. Kumar, V. Jayaraman, DAE-BRNS Theme

Meeting “Chemistry in Nuclear Technology (CHEMNUT 2015).

2. “Evaluation of homogeneous distribution of the dopant Yb in a ABO_3 Pervoskite compound using INAA technique”, **M. Bootharajan**, J.S.Brahmaji Rao, G.V.S. Ashok Kumar, R. Kumar, V. Jayaraman, M. Joseph, International Conference on Recent Advances in Analytical Science (RAAS -2016);

22/02/19

M. Bootharajan

Dedicated to my beloved family

You cannot believe in God until you believe in yourself

…..Swami Vivekananda

ACKNOWLEDGEMENTS

First and foremost, I would like to thank the Almighty for giving me the opportunity, strength, knowledge and ability to undertake this research study and to persevere and complete it satisfactorily. This achievement became possible, only with His blessings.

I express my sincere thanks to my Ph.D supervisor **Dr. V. Jayaraman,** Head, Material Chemistry Division, & MC & MFCG for his valuable guidance, continuous evaluation and constant encouragement. I am deeply indebted to him for his utmost care, special interest, and genuineness towards each and every stage of investigation with sincerity during the course of my thesis work. I owe my deep sense of gratitude for his unimaginable support and inspiration.

I express my profound thanks to Shri. C. R. Venkata Subramani, Former Head, NRCS, and RRF, IGCAR, who provided me this opportunity and also for his valuable advice, excellent guidance and encouragement. I also express my sincere thanks to Shri. K. Swaminathan my former senior officer for his valuable inputs and suggestion towards my thesis work.

I would like to thank my technology Advisor Dr .R. Kumar, Head NRCS, MC & MFCG for his valuable suggestions, strong support and ever willing help in almost all aspects of my Ph.D work.

I would like to express my sincere thanks to Former heads PDD, BARC (Late Shri. B. K. Sen & Shri. S. G. Kulkarni) and former senior officer Dr. R. R. Khandekar,

for their valuable inputs, guidance and constant encouragement during my earlier carrier in PDD, BARC which enabled my subsequent scientific ventures feasible.

It gives me a great pleasure to express a deep sense of gratitude and thanks to the former directors Dr. P.R. Vasudeva Rao, Dr. S.A. Satya Murty and present director, IGCAR, Dr. Arun Kumar Bhaduri for permitting and made the IGCAR facilities available for my Ph. D.

I also thank one former director Dr. M. Joseph and the present director MC& MFCG, Dr. B. K. Panigrahi for permitting and made the RCL facilities available for my Ph.D.

I would like to express my sincere thanks to Dr. K. Ananthasivan, AD MC & MFCG for his constant encouragement, motivating technical advices and valuable suggestions during the course of my Ph. D.

I am pleased to express my gratitude to my doctoral committee chairman, Dr. N.V. Chandra Shekar for his valuable suggestion and critical evaluation of the work progress. I thank my other doctoral committee members Dr. K.I. Gnanasekar and Dr. H.N. Jena for their constant support and valuable suggestions. I thank Dr. N. Sivaraman, Dean chemical sciences, HBNI- IGCAR for all his support and encouragement during my thesis submission.

I express my sincere thanks to Dr. N. Ramanathan & Dr. S. Balakrishnan for their kind help and technical support to accomplish my research work.

I express my humble thanks to Dr. A. Sree Rama Murthy for his kind help, constant encouragement, and inexplicable support to carry out experiments, analysis, and technical discussion in almost all aspects of my Ph.D course.

I wish to express my sincere thanks to Dr. E Prabhu, for his moral support and kind help to carry out experiments and analysis during my thesis preparation. I would like to thanks Mrs. P. C. Clinsha, Shri. Nair Afijith Ravindranath, Shri. Lakshmi gandan, Shri. M. Ravindhra Babu and senior research fellow Ms. Veena for their kind help and technical support to accomplish my research work successfully.

It gives me a great pleasure to express my sincere thanks to my colleagues in my section Dr. G.V. S Ashok Kumar, Shri J.S.Brahmaji Rao and E. Senthilvadivu for their kind help and technical support to carry out experiments during my thesis preparation. I thank my other colleagues in my section Shri Debais Saha, Shri Manish Chand and Mrs. J Vithya for their constant support and valuable technical discussions. I thank my project students Ms. M. Revathi, Ms. R. Rajashree and Ms. E. Haripriya for their help in carrying out various experiments.

I wish to express my sincere thanks to Dr. Sudha, Mrs. Aani, Dr. Kitheri Joseph, Dr. R. Asuvathraman, Shri. R Raja Madhavan, Dr. Binoy Kumar Maji, Shri. S.C Parida, Shri. Dasarath Maji, Shri. Bola Sankar, Shri. Abhiram Senapathy and Shri. G. Jogeswar Rao, for their kind help and technical support to accomplish my research work.

I express my sincere thanks to Shri. V. Suresh Kumar, Shri A Anantha Kumar, Shri. R. Raja Ram, Shri. G. Parthiban, Shri. N. Eswaran, & Shri, A. Praveen for their kind help and mechanical support for the fabrication of equipment to carry out experiments during my thesis preparation.

My acknowledgment would be incomplete without thanking the biggest source of my strength, my family. The blessings of my father, Late Mr. K. Muthiah, and grandmother Late Mrs. A. Ramalakshmi, who always encouraged and supported me from my childhood to reach the current position.

Finally, but not the least, I would like to express my gratitude to my mother Mrs. M. Kanthimathi, wife Mrs. B. Kanthimathi, my son B. Muthusanjai, and all my other family members for their help, support and constant encouragement without which this thesis would not have come to this stage.

CONTENTS

Chapter 1 : Introduction

Chapter 2 : Experimental methods

Chapter 3: Behavior of Ytterbium in Calcium and Strontium Zirconate Matrices

Chapter 4: Preparation & physio-chemical characterization of $BaTh_{1-x}Yb_xO_{3-\delta}$ (x = 0 – 0.2)

Chapter 5: Electrical conductivity and chemical stability of pure and Zr substituted $BaThO_3$

Chapter 6: Demonstration of hydrogen separation using $SrZr_{0.95}Yb_{0.05}O_{2.975}$ as proton conducting membrane

Chapter 7: Summary and conclusions

Chapter-8: Scope for future work

SYNOPSIS

Solid ionic conductors are known as solid electrolytes, transport by means of ions, and exhibit negligible electronic transport. They are mainly crystalline and amorphous inorganic solids as well as ionically conducting polymers. They have rigid framework structure within which one set of ions forms a mobile sublattice. These materials show a wide range of conductivity from 10^{-1} to 10^{-13} Scm^{-1} at ambient temperature [1-2]. The requirements for high ionic conductivity are (i) vacant sites for ions hopping and (ii) small energy barrier for ions to hop between sites. These materials are found to exhibit high cationic (e.g. Li^+, Na^+, Ag^+ Cu^+, H^+, etc.) and anionic (e.g. F^-, O^{2-} , etc.) conductivities [3].

Crystalline electrolytes provide an essentially rigid framework with channels along which one of the ionic species of the solid can migrate. They are divided into two groups namely soft and hard framework crystals and their examples include AgI, CuI, $RbAg_4I_5$, etc and β-alumina, stabilized zirconia, NASICONs, $LiAlSO_4$, etc, respectively [4].

Glassy / amorphous solid electrolytes have advantages over their poly-crystalline counterparts e.g. high isotropic conduction, absence of grain boundary conduction. They can be prepared easily in desirable shapes. These materials have three basic constituent compounds as the generalized compositional formula i.e. MX, M_2O: A_xO_y where MX-dopant salt (AgI, CdI_2 etc), M_2O- glass modifier (Ag_2O, Cu_2O, etc.) and A_xO_y- glass former (B_2O_3, P_2O_5, etc.) [5, 6].

The solid polymer electrolyte as solvent-free material in which, the ionically conducting pathway is generated by dissolving the low lattice energy metal salts in a high molecular weight polar polymer matrix with aprotic solvent as polymers are generally electrical insulators. These electrolytes have applications in electrochemical devices such as fuel cells, sensors, separation membrane, etc. The examples of such compounds are sulfonated fluorocarbon (NAFION) [7, 9], sulfonated polybenzimidazole (S-PBI) [8], sulfonated polyether ether ketone (S-PEEK) [9], etc.

The most of the oxide-ion conducting materials have a crystal structure of fluorite type, AO_2, where A is a tetravalent cation. Typical example is yttria-stabilized zirconia, which exhibits oxide ion conduction at temperatures above 973 K [10]. Shores et al. [11], reported proton conductivity in acceptor-doped ThO_2 for low p_{O_2} (high p_{H_2}) and temperature above 1473 K. Aliovalent cations such as Sc, Gd-doped CeO_2 exhibit superior ionic conductivity at a high temperature typically in the range 1073 – 1273 K [12].

Perovskite-type materials (ABO_3) are projected to be alternative materials to high-temperature oxides and proton conducting AO_2 compounds. This perovskite-type oxide exhibits pure oxide ion, mixed oxide ion / proton and pure proton conductivity in hydrogen or water containing (humid) atmosphere.

The perovskite with the basic formula of $AB_{1-x}M_xO_{3-\delta}$ where, M is Trivalent (e.g. Nd^{3+},Gd^{3+},Y^{3+},Yb^{3+}, etc.) substituted various zirconates and cerates based perovskite oxide (e.g. $SrZrO_3$, $BaCeO_3$, $CaZrO_3$, etc.) have been reported to have reasonable oxide and proton conductivities in the oxygen and hydrogen / water vapour atmosphere [14]. When aliovalent cations (Y^{3+}, Yb^{3+} Gd^{3+}, etc.) are substituted in place of B site, oxygen vacancies are created in order to maintain overall electroneutrality. These vacancies play an important role in ionic (oxide, or proton or mixed ionic) conduction. 5 mole % Yb substituted $SrCeO_3$ have been reported to have proton conductivity of 5 and 18 $mScm^{-1}$ at 1073 and 1273 K respectively [15].

Doping with multivalent cation at B site in the ABO_3 type perovskite is found to exhibit mixed ionic conductivity [16]. Efforts are also continuously made to develop perovskites that can operate especially for proton at intermediate temperature ranges, 573 - 973 K. These materials have a wide range of applications in the field such as, batteries, fuel cells, sensors, and gas separation membranes, etc. Research is underway to find a new class of compounds to use them in the above-mentioned applications at a reasonably low temperature i.e. typically 573 -773 K.

Chapter 1

This chapter provides a brief introduction to solid electrolytes, their types and characteristics, that are classified based on the nature of ion conduction species as cations (e.g. Li^+, Na^+,Ag^+, H^+, etc.) and anion conductors (e.g. F^-, O^{2-}, etc.).The ionic and electronic conduction data are presented for the solid electrolytes such as polymer and high-temperature ceramic oxide (MO_2) based compounds. This chapter also discusses class 1 and 2 type ABO_3 perovskite oxides and their structure, defect chemistry, ionic conduction such as, oxide ion, proton, the transport mechanism of oxide, proton and mixed ion conduction. The stability of perovskites against CO_2 is also presented. This chapter further outlines the oxide and proton conduction of rarely reported compounds such as ytterbium substituted ABO_3 perovskites (A= Ca, Sr and Ba) and the substituent (B= Zr and Th). Finally, the objectives of the present investigations are presented as below:

(i) $CaZr_{1-x}Yb_xO_{3-\delta}$ and $SrZr_{1-x}Yb_xO_{3-\delta}$ - Synthesis, homogenization, solid solubility limit, characterization and electrical conductivity studies in different atmospheres such as air, O_2, and 80 ppm hydrogen in argon. (ii) $BaTh_{1-x}Yb_xO_{3-\delta}$ - Modified solid synthesis, solid solubility limit, characterization and electrical conductivity studies in O_2, 80 ppm H_2 in argon and pure hydrogen. (iii) Retention of H_2 / D_2 in the zirconates and thorates matrices. (iv) Preparation and solid solubility limit of $BaZrO_3$-$BaThO_3$ to improve the stability of $BaThO_3$ against CO_2. (v) Design and fabrication of a facility for studies related to the separation of hydrogen from argon.

Chapter 2

This chapter discusses the use of solid state route in the preparation of $CaZr_{1-x}Yb_xO_{3-\delta}$, $SrZr_{1-x}Yb_xO_{3-\delta}$, $BaTh_{1-x}Yb_xO_{3-\delta}$ (x = 0 - 0.2) and $BaTh_{1-x}Zr_xO_3$ (x = 0 - 0.4). The different physio-chemical characterization adapted during the course of the study is discussed. The principles of different experimental techniques used in the present investigations namely, neutron activation analysis (NAA), X-ray diffraction, scanning electron microscopy (SEM), helium densitometer, attenuated total reflection spectroscopy and impedance spectroscopy are discussed in this chapter. This chapter also includes the design and fabrication of facilities required for carrying out the conductivity and separation studies of the materials taken for investigations.

Chapter 3

This chapter mainly covers the characterization of pristine and ytterbium substituted calcium zirconates. Compositions of $CaZr_{1-x}Yb_xO_{3-\delta}$ (x = 0 - 0.2) were prepared via solid state-reaction method. The homogeneous distribution of Yb^{3+} in the $CaZrO_3$ compound was established using neutron activation analysis. The compounds were characterized using different techniques such as, XRD and SEM. From these studies, the solid solubility limit of ytterbium in calcium zirconate was established for the first time. The electrical conductivity of the sintered pellets was carried out in different atmospheres such as air, O_2, and 80 ppm H_2 in argon in the temperature range of 798-

973 K using AC impedance spectroscopy. No electrical conductivities studies have so far been reported in the literature on the ytterbium substituted $CaZrO_3$. The chapter provides the following outcome: Introduction of ytterbium does not influence grain growth of calcium zirconate. The electrical conductivity decreases as ytterbium concentration increases, and reduces by two orders for the composition $CaZr_{0.9}Yb_{0.1}O_{2.95}$, compared to pure $CaZrO_3$ in air. The conductivity is not influenced by the atmosphere in which the studies were carried out.

Similarly, the compositions of $SrZr_{1-x}Yb_xO_{3-\delta}$ (x = 0 - 0.2) were also prepared via solid state-reaction method. The results of phase formation and surface morphology of the compounds confirmed by XRD, and SEM respectively are discussed in this chapter. The solid solubility limit of ytterbium in strontium zirconate was established by X-ray diffraction studies. AC impedance spectroscopy was used to characterize the total electrical conductivity of the sintered pellets in different atmospheres such as air, O_2, and 80 ppm H_2 in argon in the temperature range of 798 - 973 K. Introduction of ytterbium inhibited the grain growth up to the solid solution formation limit in strontium zirconate. On introduction of ytterbium, the conductivity increases, and reaches the maximum for the composition of $SrZr_{0.95}Yb_{0.05}O_{2.975}$ in all the atmospheres. The activation energy is marginally lessened for ytterbium substituted composition in all the atmospheres in comparison with pristine $SrZrO_3$. The present studies elucidate the contrasting roles played by the ytterbium in the solid solution formation range, grain growth, and electrical conductivity of calcium and strontium zirconate matrices.

Chapter 4

Similar to the earlier chapter, this chapter deals with the characterization of $BaTh_{1-x}Yb_xO_{3-\delta}$ (x = 0 - 0.2), that were synthesized via vacuum aided process followed by argon flow, low-temperature solid state synthesis. This chapter provides the theoretical calculations, which helped to carry out the modified solid state synthesis of the pristine and ytterbium substituted $BaThO_3$. The result reveals that the solid solution is formed up to 15 mole % of Yb substitution in $BaThO_3$ for the first time. The prepared compounds were characterized using XRD, SEM, and the results presented. The lattice parameter of the pristine and the ytterbium substituted compounds were calculated and compared with reported values [18, 19]. The densities of the sintered pellets are determined using helium pycnometer are discussed. AC impedance spectroscopy was used to characterize the total electrical conductivity of the sintered pellets in different atmospheres such as O_2, 80 ppm H_2 in argon and pure H_2 in the temperature range of 573-873 K. The effect of dopant concentration on electrical conductivity in oxygen and hydrogen atmospheres is discussed. The retention of hydrogen / deuterium in the thorate matrix is elucidated in this chapter.

Chapter 5

This chapter discusses the formation of solid solution of Zr substitution in place of Th in $BaThO_3$, which was prepared via modified low-temperature solid state synthesis discussed in chapter-4. The X-ray diffraction results reveal the solid solution of Zr in place of Th in $BaThO_3$ formed up to 20 mole %, and precipitated out further with higher concentration of Zr, which was established for the first time. The grain size is found to decrease for Zr substituted compounds in comparison with the pristine barium thorate, evidenced by SEM. Effect of Zr substitution on the stability of

$BaThO_3$ against carbon dioxide at two different temperatures is discussed in this chapter. The variation in the electrical conductivity, owing to the zirconium substitution in three different atmospheres such as O_2, 80 ppm hydrogen in argon and H_2 were also discussed.

Chapter 6

This chapter deals with the design and fabrication of an experimental facility for separating hydrogen from argon. The home-built apparatus consists of inner and outer chambers with inlet and outlet connections. The two chambers are separated by a disc of solid electrolyte, hermetically sealed. Preliminary separation studies were carried out using a mixture of 1500 ppm hydrogen in argon and the results are discussed.

Chapter 7

This chapter summarises the results obtained in this work on the preparation and physio-chemical characterization of ytterbium substituted zirconates and thorates based perovskite-type oxide materials. Based on the results of these investigations, compositions that can be explored as solid electrolyte membrane materials for separation of hydrogen from the gaseous mixture such as hydrogen in argon and helium are recommended.

Chapter 8

This chapter discusses the scope for the future work, about the application of these compounds in the various fields.

References

[1] A. R. West, Solid State Chemistry, and its applications ISBN 978-1-119-94294-8.

[2] Suresh Chandra, "Super ionic Solids: Principles and applications", North –Holland Publishing Company, Amsterdam (1981).

[3] Peter G. Bruce. Solid state electrochemistry, Cambridge University, Press 1995, ISBN 0-521-40007-4.

[4] C. Julien, G. Nazri. Solid State Batteries: Materials Design and Optimization, Kluwer, Academic Publishers, Boston, 1994.

[5] S. Geller, in Superionic Conductors, G.D. Mahan, W.L. Roth (eds.), Springer-Verlag, US, 1976, pp.171-182.

[6] M.C.R. Shastry, K. J. Rao, Proc. Indian Acad. Sci. (Chem. Sci.)102 (1990) 541-553.

[7] Slade RCT, Barker J, Strange J. H Solid State Ion 35, (1989) 11–15.

[8] Glipa X, El Haddad M, Jones DJ, Roziere J Solid State Ion 97 (1997) 323–331.

[9] Alberti G, Casciola M, Massinelli L, Bauer B J Membr Sci 185, (2001) 73–81.

[10] Lorenzo Malavasi, Craig A. J. Fisher, and M. Saiful Islam Chem. Soc. Rev., 39, (2010) 4370–4387.

[11] David A. Shores and Robert A. Rapp J. Electrochem. Soc 119, (1972) 300-305.

[12] S. P. S. Badwal, F. T. Ciacchi and D. Milosevic, Solid State Ion, 136 – 137 (2000) 91-99.

[13] J. W. Phair. S. P. S. Badwal Ionics 12, (2006) 103–115.

[14] Iwahara H Solid State Ion 86–88, (1996) 9–15.

[15] S.-J. Song, E.D. Wachsman, J. Rhodes, S.E. Dorris, U. Balachandran Solid State Ionics 167 (2004) 99 – 105.

List of Figures

List of Tables

CHAPTER 1

Chapter 1: Introduction

The science of solid electrolytes describes solids which exhibit appreciable high conductivity of cations or anions but are electronic insulators, developed rapidly, in early 1970s. These compounds with high ionic conductivity of the order of 10^{-4} S/cm found their enormous use in various technological applications [1-5]. They are either in the form of solids or liquids. In practical applications, compared to solid electrolytes, liquid electrolytes have more disadvantages such as leakage, corrosion and limited temperature range, etc. [6]. These disadvantages are mitigated by the solid electrolytes. Some of these solids, which exhibits electronic conduction often referred to as “mixed conductors”, while the pure ionic conductors with negligible electronic conductivity are termed as “super ionic conductor or fast ion conductor or solid electrolytes”. This class of compounds find application in electrochemical devices such as batteries, super capacitor, sensors, smart windows, etc. [7-11].

1.1 General characteristics of solid electrolytes

(i) A large number of the ions (cations or anions) are mobile. A large number of empty sites either vacancies or accessible interstitial sites are required for the conduction process.

(ii) The empty and occupied sites have similar potential energies, with low activation energy barrier for jumping between neighboring sites. High activation energy decreases carrier mobility and very stable sites (deep potential energy wells) lead to carrier localization [12].

(iii) The structure have solid framework, preferably 3D, permeated by open channels, etc.

1.2 Classification of various ion-conducting materials

Solid electrolyte materials are classified based on the nature of the ion conduction species as cation conductors (Li^+, Na^+, Ag^+, H^+, etc.) and anion conductors (F^-, O^{2-}, etc.). They are summarized in the following section.

(i) Lithium ion conductors

Since 1970, many research groups have pursued research towards feasible solid state inorganic Li^+ solid electrolytes. These electrolytes have been developed for high density batteries owing to their light weight, ease of handling and high electrochemical potential [13]. This is attributed to the small cationic size and high polarizing power of Li^+ ions as compared to other ions. Various Li^+ conducting systems reported for their practical application in solid state ionic devices are listed below: Li_2O-LiX-M_xO_y (X = Br, Cl; M_xO_y = P_2O_5, B_2O_3), Li_2S-GeS_2, Li-Na-β-alumina, $LiAlSiO_4$, etc. [14-17] and polymer electrolytes: PEO-$LiCF_3SO_3$, PEO-$LiBF_6$, PEO-$LiClO_4$, PPO-$NaCF_3SO_3$, etc. [18].

(ii) Sodium ion conductors

Sodium ion conductors or β-alumina compounds have the general formula $M_2O.nX_2O_3$ where, M is monovalent cation (M = Cu^+, Ag^+, Na^+, K^+), X is a trivalent cation (X = Al^{3+},Ga^{3+}, Fe^{3+}) and n has values in the range of 5 to 11 and they are the most important member of β-alumina family owing to their two-dimensional ionic structure. Among these, sodium-β-alumina exhibits ionic conductivity of the order of 10^{-2} Scm^{-1} at ambient temperature [19].

(iii) Silver ion conductors

Silver ion conductors are the most widely studied class of solid electrolytes with high ionic conductivity at ambient temperature, e.g. $RbAg_4I_5$ and Ag_3SI. α-AgI is a superionic conductor which, exhibits high ionic conductivity due to the structural disorder originating in its crystallographic nature. Fast silver ion conducting systems such as glassy [20-22] and polymer [23] electrolytes have been reported.

(iv) Oxygen ion conductors

The oxide ion conductors have the general formula, MO_2 (where M = Ce, Zr and Th). When these compounds form solid solution with oxides of Ca, Y and Sr, increase in ionic conductivity of about two orders of magnitude was observed [24]. The O^{2-} ion conducting solid electrolytes find main application in the field of fuel cells. Typical conductivity values range from 0.02 to 0.2 Scm^{-1} at 1273 K with an activation energy of about 0.7 -1.2 eV [25].

(v) Fluoride ion conductors

These materials possess fluorite structure that provides an open path for fast ionic conduction. However, high ionic conductivity has been perceived by generating vacancies through doping aliovalent fluoride cations. The solid solution of PbF_2 with SnF_2 i.e. $PbSnF_4$ and CaF_2 with rare earth fluorides such as LaF_3 show conductivity of the order of 10^{-3} Scm^{-1} at ambient temperatures [26, 27]. These materials are used as electrode materials for rechargeable lithium batteries, owing to the high electronegativity of fluorine and their Gibbs energy formation [27].

(vi) Proton conductors

The need for hydrogen storage and various other applications such as fuel cells, separation membranes and sensors have driven a strong research in field of proton conducting materials e.g. stabilized zirconia [28], ceria based materials [29] and sulfonated polymer like poly (ether –ether –sulfone)s (PEESs) [30] etc. Various proton conducting materials including polymeric membrane have been developed for fuel cell and sensor applications. The following sections will deal with oxide and proton conductors in detail.

1.2.1 Organic and inorganic ionic conductors

Solid electrolytes such as polymer and ceramic based materials exhibit ionic conduction and also show reasonable proton conductivity in the temperature range of 373 to 1173 K. These materials have high potential use for the construction of electrochemical devices such as fuel cells, sensors and separation membranes, etc. The electrolytes which find applications in the above-mentioned areas are broadly classified into (a) organic polymer-based and (b) inorganic / ceramic compounds. The following sections provide a brief account of these two classes of compounds.

(a) Polymer / organic based membrane

In general, the proton conducting polymer electrolytes have negatively charged groups attached to the backbone of the polymer. In the absence of water, these electrolytes tend to be rigid or a poor proton conductor. The hydrated polymer electrolytes show higher proton conductivity and reach values of 10^{-2} to 10^{-1} Scm^{-1} [31]. A perfluorinated backbone with strong acidic SO_3H groups terminated in the side chains, referred as NAFION, is the most attractive polymer membrane material, and its structure is shown in Figure 1.1 **[32].**

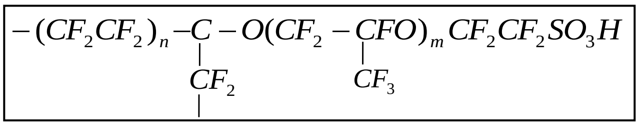

$$-(CF_2CF_2)_n-\underset{\substack{|\\ CF_2\\ |}}{C}-O(CF_2-\underset{\substack{|\\ CF_3}}{C}FO)_m CF_2CF_2SO_3H$$

Figure 1.1 Chemical structure of perfluorinated polymer electrolyte membrane (Nafion)

The oxo acids such as phosphoric acid (H_3PO_4) [33], sulfuric acid (H_2SO_4), perchloric acid ($HClO_4$) and (H_3OClO_4) [34] exhibit appreciable proton conductivity in the anhydrous state, owing to its self-dissociation in aqueous solution, that leads to the generation of hydrated protons.

In the 1960s, the proton-conducting polymer electrolytes based on aromatic polymers in which poly (styrene sulfonic acid) is a basic material and analogous polymers such as phenol sulfonic acid resin and poly (trifluorostyrene sulfonic acid resin) were frequently used. These aromatic polymers such as poly (styrene) [35, 36] poly (1, 4-phenylene) [37-40], etc. are chemically and thermally stable.

Proton conducting polymer membrane should meet the following requirements for its use in high-performance polymer electrolyte fuel cell (PEFCs) [31].

(i) Low-cost

(ii) High proton conductivities over 373 K

(iii) Good water uptakes above 373 K and

(iv) Long durability

Takahashi et al.[41], reported moderate proton conductivity in acids like H_2SO_4 or H_3PO_4 which, form compounds in narrow composition ranges with triethylenediamine ($C_6H_{12}N_2$) and hexamethylenetetramine ($C_6H_{12}N_4$). The polymer-based proton conducting materials are attractive mainly in the field of electrochemical applications such as fuel cells [42].

(b) Ceramic /Inorganic-based membranes

In early 1899, Nernst [43] reported the oxide ion conductivity in ZrO_2 with 15 wt % Y_2O_3 and the stabilized zirconia is denoted as YSZ. From the literature, most of the fluorite-type structure oxides consisting of tetravalent cations have been widely studied as oxide ion conductors. This fluorite-type structure is a face-centered cubic arrangement of cations with anions occupying all the tetrahedral sites with a large number of vacant octahedral interstitial sites. Thus, rapid ion diffusion is achieved owing to the open structure. In addition, the high oxide ion conductivity is achieved by substituting a lower valent cation that leads to the creation of the oxygen vacancies. However, YSZ requires high temperature for higher oxide ion conductivity [44]. Proton transport can occur in these oxides under certain conditions [45-49]. Niagara et al. [46] and Sun et al. [49] confirmed that these fluorite-type oxide materials exhibited low proton conductivity even at high temperature. For example, the proton conductivity of Gd-doped CeO_2 is $1.2x10^{-6}$ Scm^{-1} at 1073 K and also reported proton conductivity in acceptor-doped ThO_2 [50], for low p_{O_2} (high p_{H_2}) and temperature above 1473 K.

The following sections describe various notations used in defect chemistry, mobility, and conductivity of the solid electrolyte.

1.3 Defect chemistry, mobility and conductivity for solid electrolytes

Defect chemistry has been intensively studied since it is an essential tool which, allows to acquire fundamental knowledge of transport properties of the conducting perovskite-type oxides. An ideal condition, at absolute temperature zero kelvin, the perfect crystal may be defined as the one in which all atoms are at rest in their lattice position. The real condition, where $T > 0$ K, all the crystals are imperfect. This imperfection in the crystal can be due to the thermal agitation of the lattice atoms, which results in the creation of defects in the crystal structure. The imperfection can also be obtained by incorporation of impurities or foreign species into the crystal structure.

The various kinds of the possible point imperfections in an ionic crystal MX (M and X are monovalent), considering the charge neutrality, are listed below [10].

(a) Vacancies

A missing of M^+ ion in a pure binary compound MX from its normal site is denoted as V_M' similarly, a vacant anion site is represented as $V_M^{\cdot}$. Here V stands for vacancy and subscript for the missing species and the superscript, prime for effective negative charge and dot for effective positive charge.

(b) Interstitials

When an ion (M^+) or (X^-) occurs in an interstitial site, then the defect is M_i' or X_i'.

(c) Schottky defects

It involves the presence of equivalent amount of cation and anion vacancies ($V_M'\, V_X^{\cdot}$). The overall formation of such defects pair within the crystal involves the transfer of a pair of cations and anions on regular lattice sites from the bulk to the surface.

(d) Frenkel defects

A cation on a normal site is transferred to an interstitial site and no new lattice sites are created in the process.

Lattice diffusion takes place through the movement of point defects. Different types of defects give rise to different diffusion mechanisms, as listed below [51]:

(a) Vacancy mechanism

The diffusion is said to take place by the vacancy mechanism if an atom on a normal site jumps into an adjacent unoccupied lattice site (vacancy). It should be noted that the atoms move in the direction opposite the vacancies.

(b) Interstitial mechanism

If an atom on an interstitial site moves to one of the neighboring interstitial sites, the diffusion occurs by an interstitial mechanism. Such a movement or jump of the interstitial atom involves a considerable distortion of the lattice, and this mechanism is probable when the interstitial atom is smaller than the atoms on the normal lattice positions.

(c) Interstitialcy mechanism

It involves the movement of an interstitial atom from one of its nearest neighbors on a normal lattice site into another interstitial position and itself occupies the lattice site of the displaced atom.

Defects in the crystal structure play a key role to influence and control the properties of solid. Kröger-Vink notation [52] is used to describe the formation of defects in the crystalline solid as shown in Table 1.1

Table 1. 1 Summary of the Kröger-Vink notation

Defect type	Notation
Metal vacancy at metal (M) site	V_M
Impurity metal (A) at metal (M) site	A_M
Interstitial metal (M)	M_i
Neutral metal (M) vacancy	V_M^X
Metal (M) vacancy with negative effective charge	$V_M^{\prime}$
Free electron	$e^{\prime}$
Neutral associated defects (vacancy pair)	$V_M V_Y$
Non-metal vacancy at non-metal (Y) site	V_Y
Impurity non-metal (Z) at non-metal (Y) site	Z_Y
Interstitial non-metal (Y)	Y_i
Neutral non-metal (Y) vacancy	V_Y^X
Non-metal (Y) vacancy with positive effective charge	$V_M^{\bullet}$
Free hole	$h^{\bullet}$

Normally solids are electrically neutral; the defects are compensated either by changing the oxidation state or by replacing them with a different element with a different charge. Non-stoichiometric compounds can be formed by introducing substituents / dopants to the host materials. These defects are known as extrinsic defects. While doping, dopants either occupy interstitial sites or substitute for atoms in the parent lattice. The partial substitution of higher valence cation (guest) in place of lower valence cation (host), cation vacancies, or interstitial anions are formed and the higher valent dopants are called donor dopants. In contrast, the partial substitutions of lower valence host cations with higher valence guest cations create oxygen vacancies (or) electronic holes for charge compensation and the substitutional lower valence cations are called acceptor –dopants.

The conductivity of each ionic species is directly proportional to the density of mobile ions, n with a specific charge q and mobility μ as shown below:

$$\sigma = nq\mu \qquad (1.1)$$

The density of the mobile species can be controlled by defect chemistry, whereas the mobility is a function of the intrinsic properties of the material and temperature. The mobility can be expressed via Nernst-Einstein equation as shown below:

$$\mu = \frac{qD}{k_B T} \qquad (1.2)$$

where k_B is Boltzmann constant and the diffusivity, D for each charge carrier can be described as a function that depends on the average carrier jump frequency and the distance of the jump, λ as shown below:

$$D = \frac{f\lambda^2}{6} \qquad (1.3)$$

In a thermally activated process, the frequency f can be described as follows:

$$f = zw_O e^{-E_a/k_B T} \qquad (1.4)$$

where z is the number of direction in which the jump can occur, w_O is a combination of activation entropy ΔS and lattice vibration frequency V_O, i.e. $w_O = V_O\, e^{\Delta S/k_B}$ and E_a

is the jump activation energy. Substituting the equations 1.2, 1.3 and 1.4 into equation 1.1 the conductivity can be expressed as a function of temperature

$$\sigma T = Ae^{-E_a/k_B T} \qquad (1.5)$$

where A is scaling factor, which is usually constant and is equal to $\frac{znw_O q^2 \lambda^2}{6k_B}$

Moreover the equation 1.5 can be expressed alternatively,

$$\ln(\sigma T) = -\frac{E_a}{k_B}\frac{1}{T} + lnA \qquad (1.6)$$

From equation 1.6, $\ln(\sigma T)$ vs 1/T presents a linear function which signifies the linearity of conductivity as a function of inverse temperature.

The intercept of lnA and a negative slope of $-\frac{E_a}{k_B}$ from which the activation energy of the ionic transport can be easily determined. Among all the solid electrolytes as discussed in section 1.2, the following section deals only with perovskite-type (ABO_3) solid electrolyte, its structure, properties and ionic conduction.

1.4 Perovskites as ionic conductors

Protonic conductors with perovskite structure have drawn much attention over last few years due to their widespread applications in electrochemical devices for energy generation, sensors [53] and hydrogen separation [54]. In 1990s and 2000s, proton solubility and conductivity have been identified in a large number of perovskites. The range of perovskites, ABO_3 covering all combinations of the valence of the A and B cations exhibits proton conductivity. The protonic defects are generally compensated by negative defect, which is mostly created by acceptor substituent.

Among A^{II}-B^{IV} perovskites, the best proton conductors are $BaCeO_3$, $BaZrO_3$, $BaTbO_3$ and $BaThO_3$, exhibit large negative hydration enthalpies and required small activation energies for proton migration. The proton conductivity reaches the maximum value of above 10^{-2} S/cm. $BaZrO_3$ has large grain boundary resistance and has the largest band gap in comparison with others.

Moving to the strontium based perovskites, the similar trend was observed as that of the barium-based perovskites. However, the conductivity is lower than Ba based compounds and in the range between 10^{-3} - 10^{-2} S/cm ($SrZrO_3$ and $SrCeO_3$). One of the best-studied proton conductors is $SrCeO_3$, whose tolerance factor is low and the material is decomposed into binary oxides and also is highly reactive with CO_2.

Further moving to the calcium-based perovskites, only a few materials are available such as $CaZrO_3$ and $CaTiO_3$. It may be noted that $CaCeO_3$ does not exist. However, the conductivity is still lower than that of Sr analogues and lies between 10^{-4} – 10^{-2} S/cm [43].

1.5 History of perovskites

The mineral perovskite was discovered in Ural Mountains, Russia, by Gustav Rose in 1839 and named after the Russian mineralogist Lev. Aleksevich von Petrovski [55]. Although the name perovskite was initially used to describe the mineral $CaTiO_3$, currently it is commonly utilized to name a specific group of oxides with general formula ABO_3 and similar crystal structure. These minerals are usually dark brown to black in colour due to impurities. At present many hundreds of compounds are known, which adopt the perovskite structure. Perovskite-type materials have a wide range of interesting properties, owing to their structural and compositional flexibility; these materials are in use in the fields such as dielectrics or piezoelectric in electronic devices and sensors, electrode and electrolyte materials for fuel cells and gas separation membranes, etc. Similar to the fluorite oxides, the perovskite structure also has a larger free volume and expected to have higher oxide ion conductivity in the intermediate temperature that makes the perovskite oxides as an alternative material to the fluorite-type oxides. In early 1980s, Iwahara et al. opened up a new field of research in which the proton-conducting properties of simple perovskites were vital [56].

In 1980, the systematic studies on the ionic conductivity of compounds with perovskite structure, revealed that several materials exhibit pure oxide ion, mixed oxide ion/proton and pure proton conductivity in hydrogen or water containing atmosphere [57]. The highest proton conductivities were observed in cerates [58]. Indium substituted strontium zirconate is the only proton conducting oxide as a separator material in hydrogen probes which are available commercially [32]. Further proton conductivity in the oxides of the other families has been systematically studied, especially proton conductivity in Ca-doped in rare earth oxide La_2O_3 [59].

1.5.1 Structure of ABO_3 type-perovskites

The general formula of perovskites is ABO_3, where A is a larger ion (Ba^{2+}, Sr^{2+}, La^{3+}, etc.) while B is a smaller ion like, Y^{3+}, Yb^{3+}, Ga^{3+}, etc. The perovskites related compounds can be synthesized with an extremely wide variety of combination of compounds because of the following reasons: (a) the perovskite structure can accommodate the two cations viz. large (A site) and small (B site), (b) distortion of the ideal cubic structure helps further flexibility that accommodates the incorporation of cations of different sizes and (c) the structure is considerably tolerant to vacancy formation. In the perovskites the A site metal ion can be either M (Na^+, K^+, etc.), (Ca^{2+}, Sr^{2+}, Ba^{2+}, etc.) or (La^{3+}, Fe^{3+}, etc.) and B site can be occupied by (Nb^{5+}, W^{6+}, etc.), (Ce^{4+}, Zr^{4+}, etc.), etc. The resulting compounds can be either ionic conductors or semiconductors or superconductors or insulator. The ideal perovskite structure is cubic, such as $SrTiO_3$ with space group (Pm3m), in which the atoms in the cubic unit cell are generally expressed in two ways as follows [55].

Case (1) Sr atoms at the origin

Atom positions:

Sr 1 (a) = 0, 0, 0;

Ti 1 (b) = 1/2, 1/2, 1/2

O 3 (c) = 1/2, 1/2, 0; 1/2, 0, 1/2; 0, 1/2, 1/2

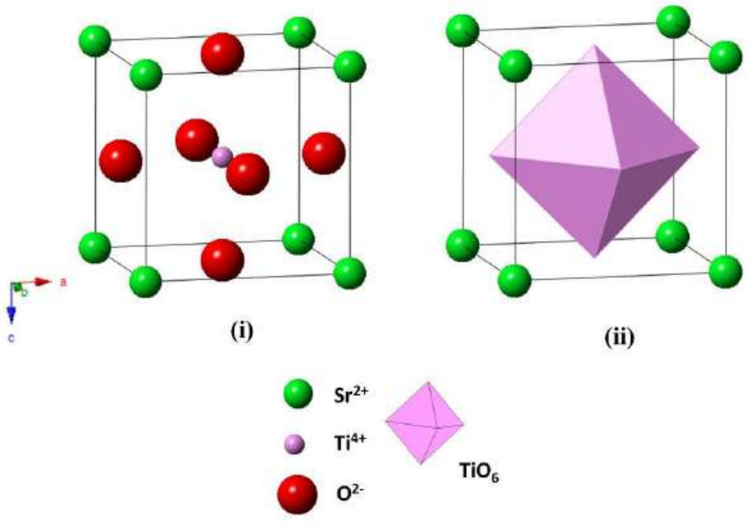

Figure 1.2 The idealised perovskite structure of $SrTiO_3$: (i) atom positions with Sr^{2+} at cell origin; (ii) TiO_6 octahedral coordination polyhedron

The Figure 1.2 [55] (i) and (ii), show the cubic $SrTiO_3$, in which Sr^{2+} ion lies at the corners of the unit cell and Ti^{4+} ion at center and are surrounded by a regular octahedron of O^{2-}.

Case (2) Ti atoms at origin

Atom positions:

Ti 1 (a) = 0, 0, 0;

Sr 1 (b) = 1/2, 1/2, 1/2

O 3 (d) = 1/2, 0, 0; 0, 1/2, 0; 0, 0, 1/2.

The large Sr^{2+} ion is at center and coordinated to 12 O^{2-} ions whereas, Ti^{4+} ion lies at the corner of the unit cell shown in Figure 1.3 [55]. The TiO_6 framework is regular and the octahedra parallel to each other, also, all the Ti^{4+}- O^{2-} bonds are equal & linear (O^{2-}-Ti^{4+}-O^{2-}).

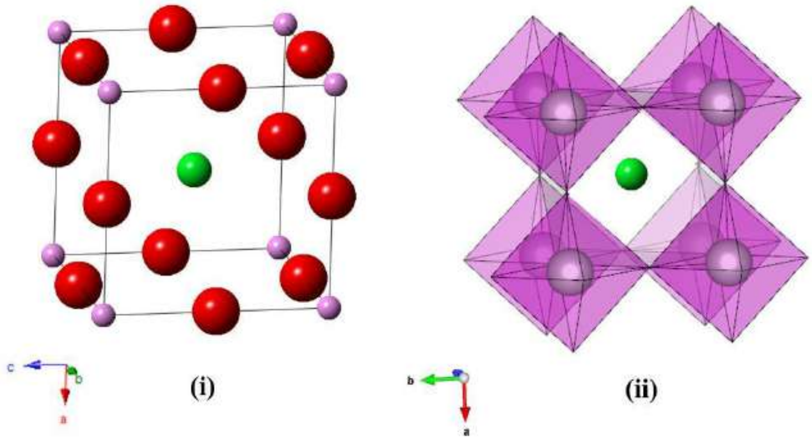

(i) (ii)

Figure 1. 3 The idealised perovskite structure of $SrTiO_3$: (i) atom positions with Ti^{4+} at cell origin; (ii) TiO_6 octahedral polyhedron framework with Sr^{2+} at the cell center

The octahedrally coordinated BO_6 forms a corner shared network, with remaining voids filled by the cation A. BO_6 octahedra can expand / contract and tilt in order to compensate for non-ideal ionic size ratios of A and B site ions.

However, owing to the strict constraints placed on the ionic sizes of A, B and O, the ideal perovskite structure is rarely obtained at ambient temperature / pressure. The distortion of perovskite structure from the ideal configuration was described based on the geometrical packing of charged spheres by the Goldschmidt tolerance factor (t). These compounds find wide applications in ceramics, refractories and electronics as well as possible hosts for nuclear waste. Properties and applications of some commonly investigated perovskites are presented in Table 1.2 [60].

Table 1. 2 Properties and applications of some perovskites

Property	**Application**	**Material**	**Reference**
Proton conductivity	H-SOFC electrolyte, Hydrogen sensor, H_2 production / extraction	$BaCeO_3$, $SrCeO_3$, $BaZrO_3$	[58, 61, 62]
Ionic conductivity	Solid electrolyte	$(La,Sr)(Ga,Mg)O_{3-\delta}$	[63]
Mixed conductivity	SOFC electrode	$La(Sr,Ca)MnO_{3-\delta+}$, $(La,Sr)(Co,Fe)O_{3-\delta}$, $LaCoO_3$	[64-66]
Ferroelectric/ piezoelectric	Piezoelectric transducer Thermistor actuator	$BaTiO_3$, $Pb(Zr,Ti)O_3$, $Pb(Mg,Nb)O_3$	[67, 68]
Catalytic	Catalyst	$LaFeO_3$, $La(Ce,Co)O_3$	[69, 70]
Electrical/dielectric	Multilayer capacitor Dielectric resonator Thin film resistor	$BaTiO_3$, $BaZrO_3$	[71]
Magnetic	Magnetic memory Ferromagnetism	$GdFeO_3$, $LaMnO_3$	[72-74]
Optical	Electro-optical modulator Laser	$(Pb,La)(Zr,Ti)O_3$, $YAlO_3$ KNbO3	[75-78]
Superconductivity	Superconductor	$Ba(Pb,Bi)O_3$, $BaKBiO_3$	[79, 80]

1.5.2 The Goldschmidt tolerance factor and formability of cubic perovskites

From the crystallographic point of view, the ideal perovskite structure is not flexible due to the non-adjustable atomic position parameters. Thus, a change in the lattice parameter results in to accommodate any compositional change. It is a simple sum of anion-cation bond lengths. The cubic (shown in figure 1.2 (i)) unit cell edge, a is equal to twice the $B - O$ bond length

$$2(\mathrm{B} - \mathrm{O}) = \mathrm{a} \tag{1.7}$$

The width of the cuboctahedral cage site,$\sqrt{2}\, a$ is equal to twice the $A - O$ bond length

$$2(\mathrm{A} - \mathrm{O}) = \sqrt{2}\,\mathrm{a} \tag{1.8}$$

The ideal structure is formed when the ratio of the bond length is given by

$$\frac{(\mathrm{A}-\mathrm{O})}{(\mathrm{B}-\mathrm{O})} = \sqrt{2} \tag{1.9}$$

or

$$\frac{(\mathrm{A}-\mathrm{O})}{\sqrt{2}(\mathrm{B}-\mathrm{O})} = 1 \tag{1.10}$$

In 1926, Goldschmidt has first exploited the above equation [55]. This equation could be used to predict the pair of ions that would form perovskite structure. When this was proposed initially, only a few crystal structures had been determined and later the ionic radii were used as a substitute for measured bond length and the relationship is shown as below

$$\mathrm{t} = \frac{(\mathrm{r_A}+\mathrm{r_O})}{\sqrt{2}(\mathrm{r_B}+\mathrm{r_O})} = 1 \tag{1.11}$$

where, t is called the tolerance factor, r_A is the radius of cage site cation (A), r_B is the radius of the octahedrally coordinated cation (B) and r_O is the radius of oxygen,140 pm. The ideally packed perovskite structure is simple cubic, with t = 1. However, many perovskite structures are distorted to orthorhombic, rhombohedral or tetragonal that can be approximated as cubic with t deviated from 1. The variation in the t lies in between 0.75 and 1. Knight [81] , proposed the four possible mechanisms for the distortion in the perovskites: (1) distortion of the BO_6 octahedra, (2) displacement of the B-site cation within the octahedron, (3) displacement of the A-site cation and (4) tilting of the octahedral relative to one another. The t factor is calculated for the compound based on their coordination number (CN) of ionic radii values reported already [82].

The pure perovskites exhibit non-stoichiometry, and this can be classified as anion or cation non-stoichiometry. Deficiency or excess of oxygen and deficiency or excess of A or B site cations are referred to anion and cation non-stoichiometry respectively. Generally, oxygen deficiencies are mostly found in the perovskite-type oxides and expressed by the general formula as $A_nB_nO_{3n-\delta}$, where δ denotes the oxygen deficiency. However, excess in oxygen stoichiometry, is rare and the incorporation of extra oxygen into the lattice structure as interstitial is energetically unfavorable. Chonghe Li et al. reported the criteria for the formability of cubic perovskites. The boundary conditions for the perovskite and non- perovskite compounds were arrived from the equations as below [83].

$$\frac{r_B}{r_O} = 0.425 \qquad (1.12)$$

$$\frac{(r_A + r_O)}{\sqrt{2}(r_B + r_O)} = 1 \qquad (1.13)$$

$$\frac{-4.317(r_A + r_O)}{\sqrt{2}(r_B + r_O)} + 3.912 = \frac{r_B}{r_O} \qquad (1.14)$$

1.5.3 Factors influencing electrical conductivity of perovskites

The structural parameters governing electrical conductivity of perovskites are given below [84]

- Goldschmidt tolerance factor
- Specific free volume of lattice
- Oxygen deficiency
- Critical radius of the pathway for oxide ion movement
- Average metal-oxide bond energy
- Lattice distortion due to mismatch in ionic radii
- Nature of dopant and oxygen vacancy

(i) Goldschmidt tolerance factor:

This was discussed already in earlier portion 1.5.2

(ii) Specific free volume:

The lattice free volume is defined as the unit cell volume minus the total volume of all the constituent ions. Here, we use the specific free volume rather than the free volume because it is convenient to compare various kinds of perovskite-type oxides.

Specific free volume = free volume / unit cell volume

= (V - total volume of the constituent ions) / V

For high oxide ion conductivity, the specific free volume of the lattice should be high providing open path to oxide ion with less energy for activation (E_a). It is inversely related to tolerance factor.

(iii) Oxygen deficiency:

The oxygen deficiency (δ) of the doped perovskites expressed by $ABO_{3-\delta}$ is calculated using the electrical neutrality condition.

(iv) Critical radius:

For an oxide ion to jump between two oxygen sites, it must pass through a gap called saddle point bordered by 2 A site cations and 1 B site cation, whose radius is called critical radius (r_{cri}). Generally r_{cri} (<105 pm) is significantly smaller than r_O (140 pm) (Figure 1.4) [85].

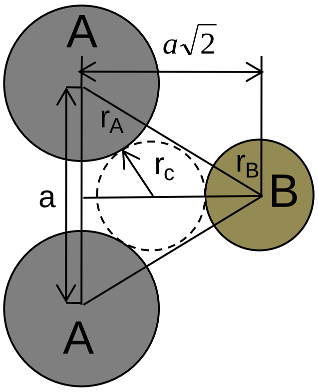

Figure 1. 4 Schematic representation of critical radius in a cubic perovskites

The thermal vibration of the cations (phonons) must play a role to facilitate the oxide ion to migrate through the gap, whose amplitude is inversely related to the square root of the ion mass. Hence, lower the mass of the vibrating cations, higher the conductivity of the material ($\sigma_i \alpha 1/m$) where, σ_i and m are conductivity and mass of the ions respectively.

1.5.4 Defects and ionic conduction in perovskites

$A^{II}B^{IV}O_3$ is perovskite-type structure, whose B site is substituted with trivalent cation viz. M^{3+}. As a result of the substitution, oxygen vacancies are created as charge-compensating species in order to maintain the electrical neutrality. This can be expressed by the Kröger-Vink notation, as shown below.

$$2B_B^X + O_O^X + M_2O_3 \rightarrow 2M_B' + V_O^{\bullet\bullet} + 2BO_2 \qquad (1.15)$$

Figure 1.5 shows the pictorial representation of substitution process which leads to the creation of oxygen vacancies that are distributed in the crystalline lattice in ABO_3 type perovskites.

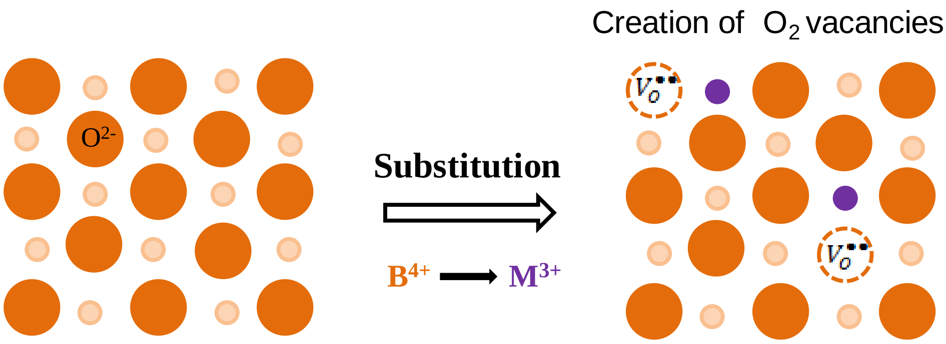

Figure 1. 5 Schematic representation of oxygen vacancies created in ABO_3 perovskites
(Reproduction from [86])

Ionic conductivity is the transport of cation or anion across the perovskite structure under the influence of electric field. The basic criteria for ionic conductivity in the perovskite to occur, the structure must contain either open regions or more population of vacancies on the appropriate sublattice to the ionic movement. In general the vacancies are created by substitution, and the higher ionic conductivity can be obtained by substitution in the cubic structure of perovskites. The essential requirement for pure ionic conductivity, the cation should not have any variable valence. In case, the variable valence cations are present, invariably, electronic conduction will also be associated with the ionic conductivity.

(a) Oxide ion conduction

When a cation of A or B in the perovskite-type oxide ABO_3 is partially substituted by a cation M of lower valence, it leads to the creation of a larger number of oxygen ion vacancies in the lattice so as to maintain the electrical neutrality of the crystal. The chemical composition of the oxide compound can be expressed as $A_{1-x}M_xBO_{3-\delta}$ or $AB_{1-x}M_xO_{3-\delta}$, where δ is an average number of oxygen deficiencies per unit formula. At elevated temperature, appreciable oxide ion conduction may be expected from these crystals, provided the energy needed for oxygen ions to jump from their original sites to the adjacent site is not very high. The highest oxide ion conductivity (0.14 Scm^{-1}) was reported for Sr and Mg-doped $LaGaO_3$ [87]. The transport mechanism involves thermally activated hopping of oxide ions from one vacant site to neighboring vacant site of equivalent energy in lattice, as shown in Figure 1.6. The energy required for this ion migration must be less than 1 eV.

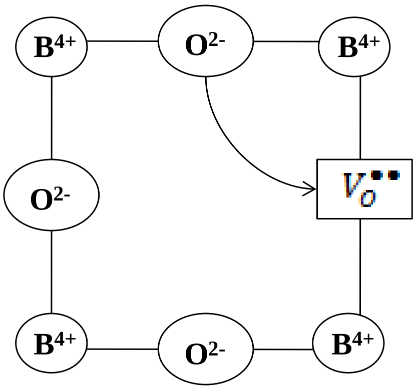

Figure 1. 6 Typical oxygen transport mechanism

(b) Proton conduction

Protons can exert a significant polarizing potential on any molecule or ion in its environment, owing to their positive charge and smaller size, whose radius is in the order of magnitude of 897 pm [88]. Protons form a covalent bond with electronegative atoms/ions and it can be shared between two electronegative atoms O-H [44]. In the perovskite-type oxides, a proton is located in the electron cloud of an oxide ion, such that the species is a hydroxide ion that occupies the site of an oxide ion and having effectively positive charge, denoted by Kröger-Vink notation as $OH_O^{\bullet}$. The protonic conduction can occur through the incorporation of protonic defect into the perovskite structure as a result of trivalent ion substitution at tetravalent B site ion. Incorporation of proton in the perovskite-type oxides can be expressed in two different atmospheres viz. water vapour (wet) and dry hydrogen H_2.

(i) Water vapor atmosphere

Figure 1.7 shows the water incorporation into the lattice structure of perovskite-type oxides. At equilibrium condition, in presence of water-saturated atmosphere the interaction of water vapour at oxygen vacancies leads to the formation of protonic defects in the form of hydroxide ion, which represents an interstitial proton strongly associated with surrounding oxygen ions. Water incorporation can be expressed by the defect equation as follows:

$$H_2O(g) + O_O^X + V_O^{\bullet\bullet} \leftrightarrow 2OH_O^{\bullet}. \tag{1.16}$$

The concentration of $OH_O^{\bullet}$ is determined by the doping level, while the oxide is completely protonated [89].

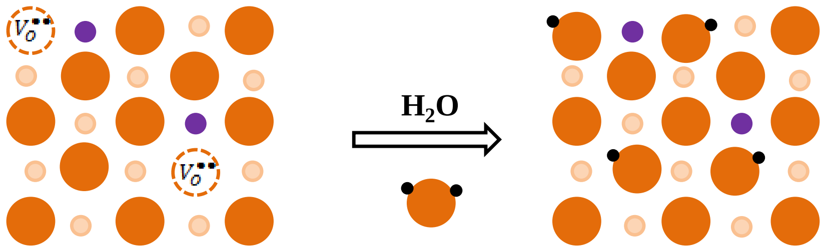

Figure 1. 7 Incorporation of water into the lattice structure of perovskite-type oxides (Reproduction from [86])

(ii) Hydrogen atmosphere

Proton incorporation can occur, when the materials are exposed to hydrogen-containing (dry) atmosphere, in which the equilibrium should exist between the hydrogen and the oxides. However, to maintain the charge neutrality, electronic defects are created (electronic conductivity) along with the formation of protons. This result in the electronic conductivity of the materials in dry hydrogen (reducing) atmosphere [90] as expressed below:

$$\frac{1}{2}H_2(g) + O_O^X \rightarrow OH_O^\bullet + e' \qquad (1.17)$$

(iii) Proton transfer mechanism

Proton transport can be described by two well known mechanisms namely, vehicle mechanism and Grotthuss mechanism [91, 92] that deal with the transport of protons (H^+) or transport of any donor-acceptor bonding that carries protons such as H_3O^+, NH_4^+ or OH^-.

a) Vehicle mechanism

Figure 1.8 shows the vehicle mechanism, which is mainly observed in compounds such as HF, HCl, Nafion and $SnO_2.nH_2O$ [32, 93] where, protons move as a passenger on a larger ion like O^{2-} forming OH^- or water molecule forming, H_3O^+.

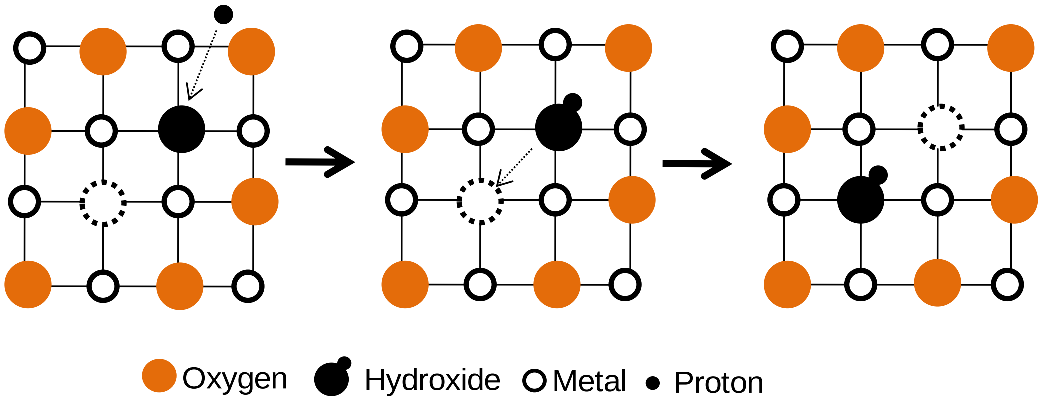

Figure 1.8 Schematic representation of Vehicle mechanism

(Reproduction from [94])

b) Grotthuss mechanism

Figure 1.9 shows the schematic representation of Grotthuss mechanism. Proton diffuses by a combination between a molecular re-orientation around the oxygen and jump of the proton from oxygen to the nearest neighbor ion. The orientation of the O-H group guides the H^+ close to the adjacent oxygen ion. The time taken for the rotation period to a complete revolution is ~10^{-12} s and jumping time is about 10^{-9} s, which is considered as the limiting step in the conduction mechanism [91, 95]. This mechanism occurs in solid acid salts (CsH_2PO_4), hydrogen uranyl phosphate (HUP), $HUO_2PO_4.4H_2O$ [1] and perovskites such as $BaCeO_3$ and $BaZrO_3$ [60]. During the proton jump, the O-H bond of the site is withheld, while coincidently the O-H bond is formed with adjacent oxygen ion and the length of the bond is ~ 90 pm [96]. This mechanism involves the formation of one bond, which is followed by breaking of another one. The extra energy needs to break O-H bond, can be avoided by the strong interaction between the proton and the two oxygen neighbors [97].

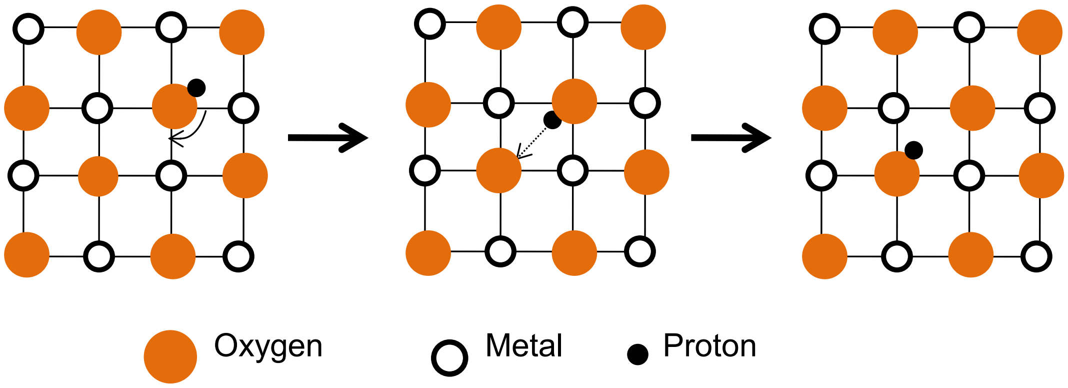

Figure 1. 9 Schematic representation of Grotthuss mechanism

(Reproduction from [94])

Kreuer [98] reported the diffusion coefficient of the proton to be orders of magnitude higher than that of oxygen thus, indicating that the proton diffusivity must involve a combination of proton transfer between oxygen ions and hydroxide ion reorientation in the perovskite-type oxide. Further, the isotope effect (H^+/D^+) measurement was perceived and the results showed that the conduction mechanism is due to proton hopping between adjacent oxygen ions which is in accordance with the Grotthuss mechanism suggested for the transport of protons [99].

1.5.5 Mixed conductivity in perovskites

The perovskite-types compounds exhibit complex conductivity and the nature of the conductivity depend on operating conditions, i.e. atmospheres and / or temperature range. The oxygen partial pressure (low or high) plays a key role that leads to either reduction or oxidation under equilibrated oxygen-containing atmosphere [100].

At low oxygen partial pressure, reduction can be considered in which the oxygen ions leave their sub-lattice generating oxygen vacancies and electrons. Further, at high oxygen partial pressure, oxidation can occur in which the oxygen vacancies tend to react with gaseous oxygen to produce oxygen ions located in the sub-lattice and electron holes. Thus, ionic conductivity involves the transport of ions (i.e. oxygen/proton) and electronic conductivity in which the transport of electron (n-type) or electron hole (p-type). Hence, the total electrical conductivity of perovskite-type oxides is a sum of the partial conductivity of each charge carrier [90].

1.5.6 Aliovalent substituted perovskites

Many perovskite-type materials are considered to be predominantly proton conductors, whereas only a few oxides are known to be mixed protonic and electronic conductors. The acceptor substituted perovskites exhibit mixed protonic-electronic conductivity in the humidified or reducing atmosphere. However, the electronic component of the total conductivity is significantly lower compared to the protonic part that limits its scope for some applications. Thus, increasing the electronic conductivity will enhance the scope of its application. The electronic conductivity may exist only under specific conditions. There are two types of electronic conductivities namely, p-type and n-type. The p-type appears as a consequence of oxygen incorporation that produces the holes. The magnitude of this p-type electronic conduction depends on the following factors:

1. Valence states: The presence of dopant elements having multivalent oxidation states (M^{n+} / $M^{(n+1)+}$ / $M^{(n-1)+}$,etc.) can enhance the electronic conductivity.

2. Polarizability: The larger the difference in electronegativity between the dopant cation and the oxygen anion, the higher the frequency of successful electron jumps between neighboring multivalent dopant ions.

On the other hand the n-type conduction can occur under sufficiently reducing conditions. To achieve this, the compounds should contain an easily reducible cation. Proton conductors are charge compensated with a proton, oxygen vacancies, and minority electronic defects as a result of acceptor substitution. The resultant electronic conductivity can be either n-type or p-type based on whether electron or hole is created. The perovskites exhibit a mixed protonic-electronic conductivity in which the protonic conduction is provided by rare-earth or transition metal substitution in $SrCeO_3$ and $BaCeO_3$ and the electronic conduction is achieved by multivalent rare-earth dopants such as $Sm^{(+2\ \&+3)}$, $Eu^{(+2\ \&+3)}$ and $Yb^{(+2\ \&+3)}$ in $SrZrO_3$, $BaCeO_3$ and $BaZrO_3$. Potter et al. [101] reported, the mixed electrical conductivity of 5 % Yb doped $SrCeO_3$ in various atmospheres in the temperature range of 573 -1123 K.

1.5.7 Chemical Stability of perovskites

The alkaline-earth zirconates such as $CaZrO_3$, $SrZrO_3$ and $BaZrO_3$ are chemically more stable than alkaline – earth cerates. However, the latter have relatively higher proton conductivity when compared to former ones at high temperature. The cerate based compounds lead to form the alkaline metal carbonates (1.18) and hydroxides (1.19) in presence of CO_2 and H_2O atmospheres, respectively and the corresponding reactions are expressed as below:

$$\mathrm{BaCeO_3 + CO_2 \rightarrow BaCO_3 + CeO_2} \qquad (1.18)$$

$$\mathrm{BaCeO_3 + H_2O \rightarrow Ba(OH)_2 + CeO_2} \qquad (1.19)$$

This reactivity may lead to the degradation of the electrolyte, limiting to its application in electrochemical devices that act under severe conditions like, solid oxide fuel cells (SOFCs), sensors and catalytic membrane reactor. Scholten et al. [102] reported that $BaCeO_3$ reacts with CO_2 at high-temperatures. However, to keep the stability of the electrolyte materials, the operation temperature should be maximum and the partial pressure of CO_2 should be sufficiently low enough to minimize the electrolyte reaction. To commercialization of the material, different processes and changes in the electrolyte have been investigated to solve the problem of low stability without sacrificing its high proton conductivity. Ryu et al. [103] reported an alternative method in which the replacement of Ce^{4+} (87 pm) by ions of different sizes such as Nd^{3+} (98.3 pm), Gd^{3+} (93.8 pm) and Zr^{4+} (72 pm) was effected in order to minimize the effects of cerate reactivity in the CO_2 rich atmosphere. It has been observed that addition of cations to the ABO_3 system like barium cerate contributes significantly to improve the chemical stability in CO_2 saturated atmospheres. The variation in the lattice parameter of the unit cell volume was observed owing to the influence of different ionic radii. The chemical stability can be increased with the addition of different dopant is also followed, which leads to significant reduction of proton conductivity. Considering this point of view, a proper manipulation of chemical species and dopant concentration, it is possible to get a specific chemical composition that results in to an electrolyte with higher conductivity and improved chemical stability. Liu et al.[104] reported that the replacement of Ce^{4+} in the B sites by Zr^{4+}ions in the $BaZr_{0.1}Ce_{0.7}Y_{0.1}Yb_{0.1}O_{3-\delta}$ composition and also inserting Y^{3+} and Yb^{3+} cations as part of defect formation mechanism were quite satisfactory for high ionic conductivity (10^{-2} Scm^{-1}) in the water vapour saturated atmosphere at 723 K.

1.5.8 Types of proton conducting perovskites

From the reported literature, the proton conducting materials operating in the temperature range of 873 - 1073 K are broadly classified into two classes [105] i.e.

Class I – Materials requiring an external circuit for electronic conduction

Class II – Materials exhibiting both electronic and protonic conduction

The following section briefs the class I and II proton conducting materials and their applications.

(i) Class I conductors (773 – 1173 K)

Class I proton conductors are particularly II-IV type oxide such as $(Ca,Sr,Ba)(Ce,Zr,Ti)O_3$ though the perovskites of type I-V like ($KTaO_3$), II_2-(III/V) (e.g. Sr_2ScNbO_6), II_3-(II/V_2) (e.g. $Ba_3CaNb_2O_9$) etc. have been studied as well. The roman number and the subscripts denote the column in the periodic table to which the element belongs to and stoichiometry of the chemical formulae respectively. These compounds show good proton conductivity i.e. in the order of 10 $mScm^{-1}$ in the temperature range 773-1173 K. The simple perovskites (I-V, II-IV, etc.) must be doped with an element of lower valency than the B site atom, (e.g. Y in Ce of $BaCeO_3$) that results to make these proton conducting materials. The size of the atom at A site has an influence in the mobility of proton, which again depends on the softness of the lattice and is therefore, favoured by large atom on the A site of the perovskite e.g. Ba. Figure 1.10 shows the proton conductivities of various oxides as calculated on basis of proton mobility and hydration thermodynamic parameters.

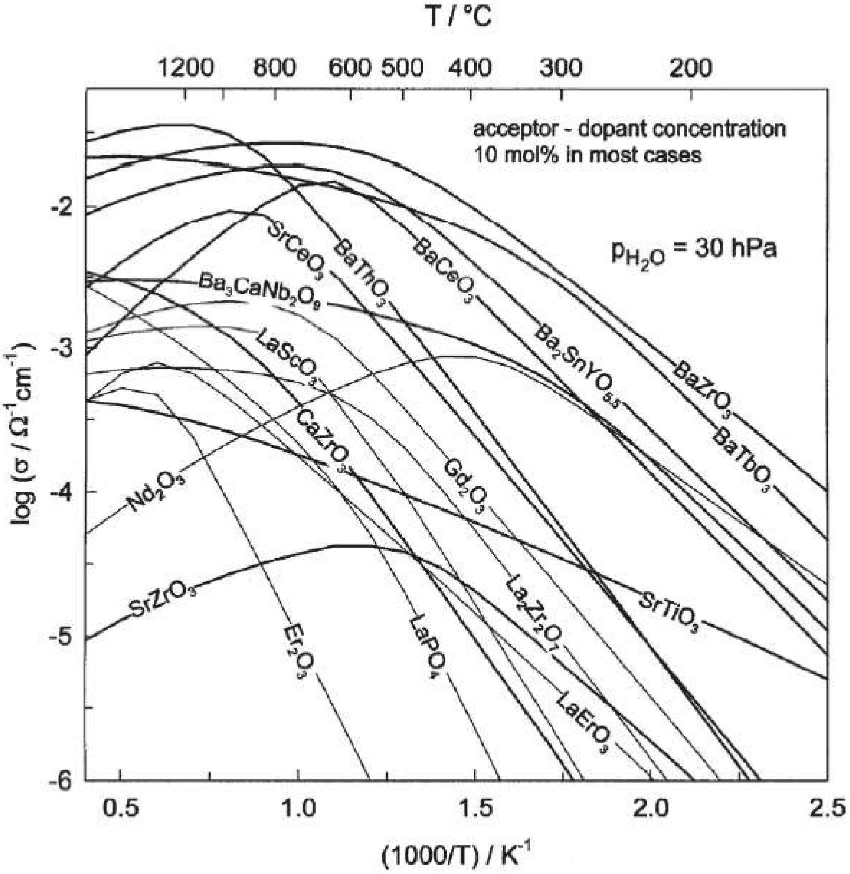

Figure 1. 10 Proton conductivities of various oxides as calculated on basis of proton mobility and hydration thermodynamics parameters

(Reproduction from [106])

It is also reported [107] that the other compounds with oxygen tetrahedra have also exhibited proton conduction, such as gallates e.g. ($Ln_{1-x}Ba_{1+x}GaO_{4-x/2}$) and $Ln_{1-x}Sr_{1+x}GaO_{5-x/2}$, (Ln-lanthanides). Tungstates with fluorite – related structure exhibits mixed conduction at low temperature. Undoped La_6WO_{12} shows the proton conductivity of 0.5 mScm^{-1} at 673 K [105].

Literature survey revealed the overview of class 1 proton conducting materials, in which some compounds are shown in Table 1.3 [105].

Table 1. 3 List of class I proton conducting compounds

Structure	Typical example	T (K)	σ_{tot} (mScm^{-1})	Reference
Perovskite	$BaCe_{0.8}Y_{0.2}O_{3-\delta}$	873 - 1173	2-3*	[108]
	$BaCe_{0.6}Zr_{0.2}Y_{0.2}O_{3-\delta}$	773 - 1173	30	[106]
Gallate	$Pr_{0.8}Sr_{2.2}GaO_{4.9}$	773 - 1173	0.13	[107]
Fluorite	$La_{26}O_{27}(BO_3)_8$	573 - 1023	1	[109]

*calculated from measured electrolyte resistance in a fuel cell, thus including contact resistances with electrodes

Applications:

The principal drive for research on class I conductors is attributed to their applications in solid oxide fuel cells (SOFCs) and electrolytic cells. This material allows to operate at lower temperature and cheaper stack construction materials than oxygen ion conducting electrolytes. In addition, that the perovskite-based materials have been tested for other applications such as H_2 pumps and H_2 sensors.

(i) Fuel cell

The electrochemical reactions that occur at both electrodes in a fuel cell are as follows [105].

Anode : $H_2 \rightarrow 2H^+ + 2e^-$ (1.20)

Cathode : $2H^+ + 2e^- + {}^1\!/_2\, O_2 \rightarrow H_2O$ (1.21)

Overall reaction : $H_2 + {}^1\!/_2\, O_2 \rightarrow H_2O + \text{Elecrical energy} + \text{Heat energy}$ (1.22)

A fuel cell is a device in which the chemical energy is directly converted in to electric energy and heat. The most common fuel is hydrogen, but other compounds such as methanol, methane and natural gas, etc. can also be used. The design of fuel cell is composed of three main components; anode, cathode and electrolyte, shown in Figure 1.11. All the components are interconnected and considered as a single cell.

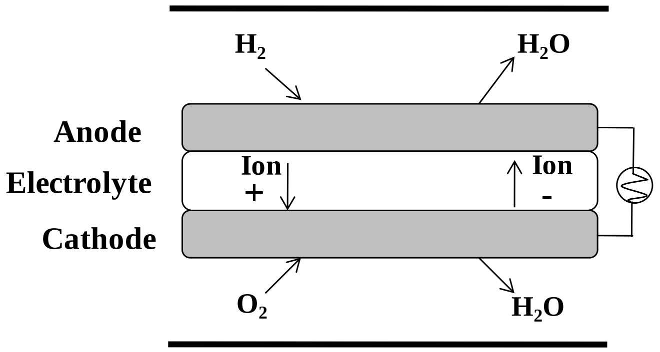

Figure 1. 11 General operation scheme of a Fuel cell with H_2

The by-product water can be produced either in the cathode or anode depending on the nature of electrolyte material as in the case of using pure hydrogen. i.e. water is formed in cathode for the electrolyte being a catonic conductor whereas the same is formed in anode for the electrolyte being an anionic conductor. The class I conducting compounds are used in the fuel cell when the cell operates in the temperature range of 873-1073 K.

(ii) Membrane reactor

In a chemical reactor, proton conducting materials can be used as a membrane for several catalytic processes. The reaction can be written as follows [105].

$$A \leftrightarrow mB + nH_2 \tag{1.23}$$

(iii) Hydrogen pump

Proton conducting materials can be widely used in the application of hydrogen pump. The electrochemical hydrogen pump is capable of pumping the hydrogen when the voltage is applied using an external DC source. Figure 1.12 shows the operation principle of a hydrogen pump.

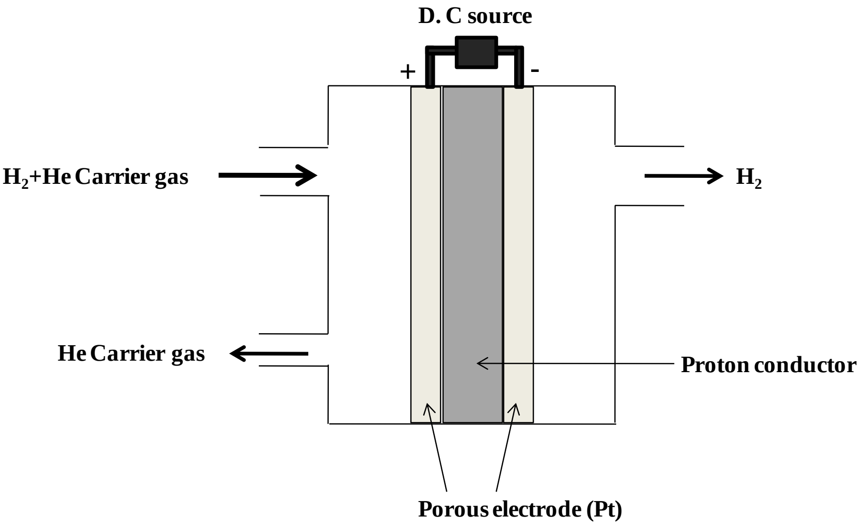

Figure 1. 12 A schematic of electrochemical hydrogen pump using the proton conductor membrane

The electrochemical hydrogen pumps consist of a proton conducting membrane material as a solid electrolyte, which is sandwiched between two porous electrodes. When a voltage is applied between anode and cathode, the electric current appears with the migration of protons from the anode to the cathode through proton conductor membrane. Matsumoto et al. [110] demonstrated the hydrogen pump using $SrCe_{0.95}Yb_{0.05}O_{3-\delta}$ as electrolyte.

Recently, the proton conducting ceramics have drawn our attention by their applications in the field of nuclear science and engineering. The electrochemical hydrogen pump using proton conductor finds an application for the recovery of tritium from the vacuum exhaust gas as well as from the blanket purge gas for recycling as fuel in a nuclear fusion reactor [111]. The electrochemical pump in which the solid electrolyte is a proton conductor finds its application in nuclear processes to recover hydrogen from water vapour (or) hydrocarbons, hydrogen sensors etc. Proton conducting materials are used in the field of sensors especially for hydrogen. The sensor element typically consists of 0.45 mm thick solid electrolyte sandwiched between two platinum electrodes. It was also reported [112] that high-temperature hydrogen sensors use proton conducting oxide such as $BaZr_{0.4}Ce_{0.4}In_{0.2}O_{3-\delta}$. For low-temperature sensors, layered perovskites are preferred. Thangadurai et al. [113] reported, perovskite layers separated by alkali metal ions have high proton conductivity at low temperature e.g. the conductivity of $KCa_2Nb_3O_{10}$ is 0.34 $mScm^{-1}$ at 317 K

(ii) Class II conductors (873-1273 K)

Class II proton conductors are prepared by two different approaches as follows:

(i) Cermet is a composite of class I proton conductor and a metal (e.g. Ni and Pd) that provide the electronic conduction. Balachandran et al. [114] reported mixed (proton/electron) conducting ceramic oxide based membranes. In cermet membrane, cermet matrix can allow the metal phase to expand and contract as the temperature and hydrogen concentration fluctuate, due to this cermet are less susceptible to crack formation compared to the hydrogen permeable metal or alloys [105].

(ii) The second approach is,

while forming the class I proton conductor, doping with multivalent cations such as Eu^{3+}, Yb^{3+}, Ti^{4+}, etc. leads to the promotion of n-type conduction. Equimolar mixture of $BaCe_{0.8}Eu_{0.2}O_{2.9}$ and $Ce_{0.8}Y_{0.2}O_{2.9}$ showed high hydrogen permeability and stability [105].

Applications:

(i) Hydrogen separation

The class II proton conductor is the most important material for separation or purification of hydrogen or hydrogen-containing gas mixtures. Song et al.[105] reported the multivalent Eu^{3+} doped barium cerate based materials for purification of hydrogen. Hydrogen permeation properties of membrane based on dense $SrCe_{0.95}Yb_{0.05}O_{3-\delta}$ thin films were reported [115].

In recent years, high-temperature applications are favoured for hydrogen separation using inorganic based membrane instead of organic-based membrane, due to the higher chemical stability of the latter one. The important type of membrane and mechanism for separation of hydrogen are shown in table 1.4 [116].

Table 1. 4 Types of hydrogen separation membranes and their mechanism

Hydrogen separation membranes	Transport Mechanism
Polymer (Glassy, Rubbery) Carbon (Molecular sieving) Microporous ceramic (Silica, Zeolite)	Molecular
Metal (Pd/Pd alloys)	Atomic
Metal Dense ceramic (protonic, Mixed protonic/electronic	Ionic

(ii) Other application

The proton conductors are found their application in the fields such as hydrogen sensors for process control and monitoring and leak detector for safety concern [116].

1.6 Scope and objective of the thesis

Literature studies reveal the availability of a few reports for the ytterbium substituted in zirconium matrix especially, $SrZrO_3$ and $BaZrO_3$ in the high temperature. However, no literature is available for ytterbium substituted $CaZrO_3$ and $BaThO_3$. This observation provides a scope to investigate the ytterbium substitution in $CaZrO_3$, $SrZrO_3$ and $BaThO_3$ and its effect on the electrical conductivity in the intermediate temperature range of 573-973 K. The overall objective of the present study is to effectively gain a good understanding of the phenomena and mechanism of the electrical conduction in some ytterbium substituted zirconates and thorates by using the physico-chemical characterization techniques. The present experimental investigations are focused on the synthesis, solubility limit of the ytterbium substituted zirconates of calcium and strontium. $CaZrO_3$ and $SrZrO_3$ exhibit good chemical stability, because of which, it necessitates the exploration of the substitution of multivalent cation (Yb^{2+}/Yb^{3+}) at B site and the impact of the substituent in the electrical conductivity of these compounds in the intermediate temperature.

A series of ytterbium substituted barium thorates is prepared via modified low temperature solid state route, which involves two different conditions such as heating under vacuum, followed by heating in argon atmosphere. The solid solubility of ytterbium in $BaThO_3$ is described. The compounds are characterized by various techniques. The electrical conductivity of these compounds is studied under different atmospheres such as O_2, 80 ppm hydrogen in argon and pure hydrogen using A.C impedance spectroscopy. Conductivity studies reveal the retention of hydrogen/deuterium in the thorate matrix, which is also elucidated the samples using infrared spectroscopy. To improve the stability of $BaThO_3$, against CO_2, Zr substituted $BaThO_3$ is prepared via modified solid state method. The solid solubility of the ZrO_2 in $BaThO_3$ is presented. The stability of the pristine and zirconium substituted $BaThO_3$ against CO_2 at different temperatures is described. The electrical conductivity of these compounds is studied and presented.

Hydrogen separation from the gas mixture (H_2/Argon) is demonstrated using one of the above discussed compounds as solid electrolyte membrane.

1.7 Layout of the research work

The dissertation is organized into 7 chapters as follows:

Chapter 1 introduces the general characteristics of various solid electrolytes and their ionic conduction, defect chemistry, perovskites and their structure and properties. Further, classification of proton conductors and their mechanism are presented. The objectives of the study are also systematically described, followed by the outline of the research work.

Chapter 2 presents the overview of the various solid state synthesis and the appropriate physico-chemical characterization techniques.

Chapter 3 discusses the behavior of Yb in calcium and strontium ziconate matrices.

Chapter 4 provides the synthesis and physico-chemical characterization of ytterbium substituted barium thorate.

Chapter 5 deals with electrical conductivity and chemical stability of pure and zirconium substituted barium thorate.

Chapter 6 discusses the preliminary experiments on the separation of hydrogen from argon using one of the above- mentioned compounds as solid electrolyte membrane.

Chapter 7 summary and conclusion of the results obtained in the current study.

Chapter 8 proposes the scope for future studies.

1.8 References

[1] A. R. West, Solid state chemistry and its applications, John Wiley & Sons Inc, Singapore, 2003.

[2] W. H. Meyer, Adv. Mater., 10 (1998) 439-448.

[3] M. Armand, J.M. Tarascon, Nature., 451 (2008) 652-657.

[4] M. B. Armand, Ann. Rev. Mater. Sci. , 16 (1986) 245-261.

[5] J. W. Fergus, J. Power Sources, 195 (2010) 939-954.

[6] M.Z.A. Munshi (ed.), Handbook of Solid State Batteries and Capacitors, World Scientific Pub. Co. Inc, 1995.

[7] W.A. Van Schalkwijk , B.S. (Ed.), Advances in Lithium-ion Batteries, Kliwer / Plenum., New York, 2002.

[8] P. Knauth, H. L. Tuller, J. Am. Ceeam. Soc, 85 (2002)1654-1680.

[9] J. S.E. M. Svensson, C.G. Granqvist, Appl. Phys. Lett. , 45 (1984) 828-830.

[10] E.C.S. (Ed). Solid Electrolytes and Their Applications, Plenum Press,, New York, 1980.

[11] B.E.Conway, Electrochemical Supercapacitors: Scientific Fundamentals and technological Application, Kluwer-Plenum Press, New York, 1999.

[12] F.M. Gray, Polymer electrolytes. , Springer Verlag, 1997.

[13] G.P.E. G. Nazri, Lithium batteries-Science and Technology, , Kluwer Academic Publishers, London,, 2004.

[14] J.P. Malugani, G. Robert, Preparation and electrical properties of the 0,37 Li_2S-0,18 P_2S_5-0,45 LiI glass, Solid State Ionics, 1 (1980) 519-523.

[15] R. Mercier, J.P. Malugani, B. Fahys, G. Robert, Superionic conduction in Li_2S - P_2S_5 - LiI - glasses, Solid State Ionics, 5 (1981) 663-666.

[16] J.L. Souquet, A. Kone, M. Ribes, Glass forming region, structure and ionic conduction of glasses in the SiO_2 Li_2O Li_2SO_4 system, Journal of Non-Crystalline Solids, 38-39 (1980) 307-310.

[17] I.D. Raistrick, C. Ho, R.A. Huggins, Lithium ion conduction in Li_5Al0_4, Li_5GaO4 and Li_6ZnO_4, Materials Research Bulletin, 11 (1976) 953-957.

[18] R C Agrawal, G.P. Pandey, Solid polymer electrolytes: materials designing and all-solid-state battery applications: an overview, J. Phys. D: Appl. Phys, 41 (2008) 223001-223019.

[19] Y. Yung-Fang Yu, J.T. Kummer, Ion exchange properties and rates of ionic diffusion in beta-alumina, Journal of Inorganic and Nuclear Chemistry, 29 (1967) 2453-2475.

[20] S. Chandra, Superionic Solids:Principles and Applications, North Holland, , Amsterdam, , 1981.

[21] K.P. Padmasree, D.K. Kanchan, Conductivity and dielectric studies on $20CdI_2$–$80[xAg_2O–y(0.7V_2O_5–0.3B_2O_3)]$ super ion conducting system, Journal of Non-Crystalline Solids, 352 (2006) 3841-3848.

[22] H. Eliasson, I. Albinsson, B.E. Mellander, Dielectric and conductivity studies of a silver ion conducting polymer electrolyte, Electrochimica Acta, 43 (1998) 1459-1463.

[23] S.A. suthanthiraraj, R. Kumar, B.J. Paul, Impact of ZrO_2 nanoparticles on ionic transport and electrochemical properties of nanocomposite gel polymer electrolyte: PPG(4000)–$AgCF_3SO_3$:ZrO_2, International Journal of Nanoscience, 10 (2011) 241-246.

[24] C. Singhal, K. Kendall, High temperature Solid oxide fuel cells: fundamental, design and applications,, Elsevier Advanced Technology, , U.K. , 2003.

[25] R. Collongues, A Kahn, D. Michel, Superionic Conducting Oxides, Annual Review of Materials Science, 9 (1979) 123-150.

[26] N.I. Sorokin, P.P. Fedorov, O.K. Nikol'skaya, O.A. Nikeeva, E.G. Rakov, E.I. Ardashnikova, Electrical Properties of $PbSnF_4$ Materials Prepared by Different Methods, Inorganic Materials, 37 (2001) 1178-1182.

[27] L.N. Patro, K. Hariharan, Fast fluoride ion conducting materials in solid state ionics: An overview, Solid State Ionics, 239 (2013) 41-49.

[28] M. Arab Pour Yazdi, P. Briois, S. Georges, A. Billard, Electrical and structural investigations of perovskite structure reactively sputter deposited coatings, Solid State Ionics, 180 (2009) 1246-1251.

[29] D. Perez-Coll, G.C. Mather, Electrical transport at low temperatures in dense nanocrystalline Gd-doped ceria, Solid State Ionics, 181 (2010) 20-26.

[30] J. Benavente, A. Cañas, M.J. Ariza, A.E. Lozano, J. de Abajo, Electrochemical parameters of sulfonated poly(ether ether sulfone) membranes in HCl solutions determined by impedance spectroscopy and membrane potential measurements, Solid State Ionics, 145 (2001) 53-60.

[31] M. Rikukawa, K. Sanui, Proton-conducting polymer electrolyte membranes based on hydrocarbon polymers, Progress in Polymer Science, 25 (2000) 1463-1502.

[32] K.-D. Kreuer, Proton Conductivity: Materials and Applications, Chemistry of Materials, 8 (1996) 610-641.

[33] T. Dippel, K.D. Kreuer, J.C. Lassègues, D. Rodriguez, Proton conductivity in fused phosphoric acid; A 1H/31P PFG-NMR and QNS study, Solid State Ionics, 61 (1993) 41-46.

[34] A. Novak, Proton transfer and superionic conduction in solids and gels, Journal of Molecular Structure 177 (1988) 277-308.

[35] B. Gupta, F.N. Büchi, G.G. Scherer, A. Chapiró, Materials research aspects of organic solid proton conductors, Solid State Ionics, 61 (1993) 213-218.

[36] S.D. Flint, R.C.T. Slade, Investigation of radiation-grafted PVDF-g-polystyrene-sulfonic-acid ion exchange membranes for use in hydrogen oxygen fuel cells, Solid State Ionics, 97 (1997) 299-307.

[37] Z. Qi, Novel supported catalysts: platinum and platinum oxide nanoparticles dispersed on polypyrrole/polystyrenesulfonate particles, Chemical Communications, (1998) 15-16.

[38] T.I. Wallow, B.M. Novak, In aqua synthesis of water-soluble poly(p-phenylene) derivatives, Journal of the American Chemical Society, 113 (1991) 7411-7412.

[39] A.D. Child, J.R. Reynolds, Water-Soluble Rigid-Rod Polyelectrolytes: A New Self-Doped, Electroactive Sulfonatoalkoxy-Substituted Poly(p-phenylene), Macromolecules, 27 (1994) 1975-1977.

[40] T. Kobayashi, M. Rikukawa, K. Sanui, N. Ogata, Proton-conducting polymers derived from poly(ether-etherketone) and poly(4-phenoxybenzoyl-1,4-phenylene), Solid State Ionics, 106 (1998) 219-225.

[41] T. Takahashi, S. Tanase, O. Yamamoto, S. Yamauchi, Proton conduction in triethylenediamine- and hexamethylenetetramine-sulfate, Journal of Solid State Chemistry, 17 (1976) 353-361.

[42] J. Kerres, A. Ullrich, F. Meier, T. Häring, Synthesis and characterization of novel acid–base polymer blends for application in membrane fuel cells, Solid State Ionics, 125 (1999) 243-249.

[43] T. Ishihara, Perovskite Oxide for Solid Oxide Fuel Cells, Springer 2008.

[44] N. Kochetova, I. Animitsa, D. Medvedev, A. Demin, P. Tsiakaras, Recent activity in the development of proton-conducting oxides for high-temperature applications, RSC Advances, 6 (2016) 73222-73268.

[45] H. Yokokawa, T. Horita, N. Sakai, K. Yamaji, M.E. Brito, Y.P. Xiong, H. Kishimoto, Protons in ceria and their roles in SOFC electrode reactions from thermodynamic and SIMS analyses, Solid State Ionics, 174 (2004) 205-221.

[46] Y. Nigara, K. Kawamura, T. Kawada, J. Mizusaki, Hydrogen permeability in $Ce_{0.8}Yb_{0.2}O_{1.9}$ at high temperatures, Solid State Ionics, 136-137 (2000) 215-221.

[47] Y. Nigara, K. Yashiro, T. Kawada, J. Mizusaki, Hydrogen permeability in $(CeO_2)_{0.9}(GdO_{1.5})_{0.1}$ at high temperatures, Solid State Ionics, 159 (2003) 135-141.

[48] W. Sun, Z. Shi, W. Liu, Considerable Hydrogen Permeation Behavior through a Dense $Ce_{0.8}Sm_{0.2}O_{2-\delta}$ (SDC) Asymmetric Thick Film, Journal of The Electrochemical Society, 160 (2013) F585-F590.

[49] W. Sun, S. Fang, L.Y. and, W. Liu, Investigation on Proton Conductivity of $La_2Ce_2O_7$ in Wet Atmosphere: Dependence on Water Vapor Partial Pressure, Fuel Cells, (2012).

[50] D.A. Shores, R.A. Rapp, Hydrogen Ion (Proton) Conduction in Thoria-Base Solid Electrolytes, Journal of The Electrochemical Society, 119 (1972) 300-305.

[51] R.J.D. Tilley, Defects in Solids, A John Wiley & Sons , INC., Publication2008.

[52] F.A. Kro¨ger, H.J. Vink, J.v.d. Boomgaard, Z. Phys. Chem (Leipzig), 203 (1954).

[53] T. Yajima, K. Koide, H. Takai, N. Fukatsu, H. Iwahara, Application of hydrogen sensor using proton conductive ceramics as a solid electrolyte to aluminum casting industries, Solid State Ionics, 79 (1995) 333-337.

[54] H. Matsumoto, T. Shimura, H. Iwahara, T. Higuchi, K. Yashiro, A. Kaimai, T. Kawada, J. Mizusaki, Hydrogen separation using proton-conducting perovskites, Journal of Alloys and Compounds, 408-412 (2006) 456-462.

[55] R.J.D. Tilley, Perovskites Structure–Property Relationships, John Wiley & Sons, Ltd, United Kingdom, 2016.

[56] Proton-Conducting Ceramics From Fundamentals to Applied Research Taylor & Francis Group, LLC, Boca Raton, FL, 2016.

[57] T. Takahashi, H. Iwahara, Rev. Chim. Miner, 17 (1980) 243-253.

[58] H. Iwahara, T. Esaka, H. Uchida, N. Maeda, Proton conduction in sintered oxides and its application to steam electrolysis for hydrogen production, Solid State Ionics, 3-4 (1981) 359-363.

[59] T. Norby, O. Dyrlie, P. Kofstad, Protons in Ca-doped La_2O_3, Nd_2O_3 and $LaNdO_3$, Solid State Ionics, 53-56 (1992) 446-452.

[60] E.C.C.d. Souza, R. Muccillo, Properties and applications of perovskite proton conductors, Materials Research, 13 (2010) 385-394.

[61] H. Uchida, N. Maeda, H. Iwahara, Relation between proton and hole conduction in $SrCeO_3$-based solid electrolytes under water-containing atmospheres at high temperatures, Solid State Ionics, 11 (1983) 117-124.

[62] H. Iwahara, H. Uchida, K. Ono, K. Ogaki, Proton Conduction in Sintered Oxides Based on $BaCeO_3$, Journal of The Electrochemical Society, 135 (1988) 529-533.

[63] F.M. and, G. JB., A superior oxide-ion electrolyte, European Journal of Solid State and Inorganic Chemistry, 31 (1994) 663-672.

[64] Y. Teraoka, H.M. Zhang, K. Okamoto, N. Yamazoe, Mixed ionic-electronic conductivity of $La_{1-x}Sr_xCo_{1-y}Fe_yO_{3-\delta}$ perovskite-type oxides, Materials Research Bulletin, 23 (1988) 51-58.

[65] S. Carter, A. Selcuk, R.J. Chater, J. Kajda, J.A. Kilner, B.C.H. Steele, Oxygen transport in selected nonstoichiometric perovskite-structure oxides, Solid State Ionics, 53-56 (1992) 597-605.

[66] T. Fukui, S. Ohara, S. Kawatsu, Conductivity of $BaPrO_3$ based perovskite oxides, Journal of Power Sources, 71 (1998) 164-168.

[67] D. Dimos, C.H. Mueller, PEROVSKITE THIN FILMS FOR HIGH-FREQUENCY CAPACITOR APPLICATIONS, Annual Review of Materials Science, 28 (1998) 397-419.

[68] T.M. Shaw, S. Trolier-McKinstry, P.C. McIntyre, The Properties of Ferroelectric Films at Small Dimensions, Annual Review of Materials Science, 30 (2000) 263-298.

[69] R. Spinicci, A. Tofanari, A. Delmastro, D. Mazza, S. Ronchetti, Catalytic properties of stoichiometric and non-stoichiometric $LaFeO_3$ perovskite for total oxidation of methane, Materials Chemistry and Physics, 76 (2002) 20-25.

[70] L. Forni, I. Rossetti, Catalytic combustion of hydrocarbons over perovskites, Applied Catalysis B: Environmental, 38 (2002) 29-37.

[71] Hiroshi Kishi, Y.M. and, H. Chazono, Base-Metal Electrode-Multilayer Ceramic Capacitors: Past, Present and Future Perspectives, Japanese Journal of Applied Physics 42 (2003) 1-15.

[72] G.H. Jonker, Magnetic compounds with perovskite structure IV Conducting and non-conducting compounds, Physica, 22 (1956) 707-722.

[73] Y. Moritomo, A. Asamitsu, H. Kuwahara, Y. Tokura, Giant magnetoresistance of manganese oxides with a layered perovskite structure, Nature, 380 (1996) 141.

[74] J.M.D. Teresa, M.R. Ibarra, P.A. Algarabel, C. Ritter, C. Marquina, J. Blasco, J. García, A. del Moral, Z. Arnold, Evidence for magnetic polarons in the magnetoresistive perovskites, Nature, 386 (1997) 256-259.

[75] Optical properties of $PbTiO_3$, $PbZr_xTi_{1-x}O_3$, and $PbZrO_3$ films deposited by metalorganic chemical vapor on $SrTiO_3$, Journal of Applied Physics, 92 (2002) 468-474.

[76] F. Jona, G. Shirane, R. Pepinsky, Optical Study of $PbZrO_3$ and $NaNbO_3$ Single Crystals, Physical Review, 97 (1955) 1584-1590.

[77] K.S. Rao, K.H. Yoon, Review: Review of electrooptic and ferroelectric properties of barium sodium niobate single crystals, Journal of Materials Science, 38 (2003) 391-400.

[78] M.J. Weber, M. Bass, G.A. deMars, Laser Action and Spectroscopic Properties of Er^{3+} in $YAlO_3$, Journal of Applied Physics, 42 (1971) 301-305.

[79] J. Ihringer, J.K. Maichle, W. Prandl, A.W. Hewat, T. Wroblewski, Crystal structure of the ceramic superconductor BaPb0.75Bi0.25O3, Zeitschrift für Physik B Condensed Matter, 82 (1991) 171-176.

[80] T.S. Sampathkumar, S. Srinivasan, T. Nagarajan, U. Balachandran, Properties of $YBa_2Cu_3O_{7-\delta}$-BaBiO3 composite superconductors, Applied Superconductivity, 2 (1994) 29-34.

[81] K.S. Knight, Structural phase transitions, oxygen vacancy ordering and protonation in doped $BaCeO_3$: results from time-of-flight neutron powder diffraction investigations, Solid State Ionics, 145 (2001) 275-294.

[82] R. D. Shannon, Acta acta Crystallographica, A32, (1976) 751-767.

[83] C. Li, S.K.C. Soh, P. Wu, Formability of ABO3 perovskites, Journal of Alloys and Compounds, 372 (2004) 40-48.

[84] Z.L. Wang, Z.C. Kang, Functional, and Smart Materials: Structural Evolution and Structure Analysis, 1998.

[85] J.A. Kilner, R.J. Brook, A study of oxygen ion conductivity in doped non-stoichiometric oxides, Solid State Ionics, 6 (1982) 237-252.

[86] V. Mao, Novel mixed protonic-electronic materials:Development of selective membranes devoted for hydrogen separation, Development of selective membranes devoted for hydrogen separation, Montpellier, France, 2016.

[87] M. Mogensen, D. Lybye, N. Bonanos, P.V. Hendriksen, F.W. Poulsen, Factors controlling the oxide ion conductivity of fluorite and perovskite structured oxides, Solid State Ionics, 174 (2004) 279-286.

[88] P.G. Blunden, I. Sick, Proton radii and two-photon exchange, Physical Review C, 72 (2005) 057601-057602.

[89] N. Bonanos, A. Huijser, F.W. Poulsen, H/D isotope effects in high temperature proton conductors, Solid State Ionics, 275 (2015) 9-13.

[90] X. Qi, Y.S. Lin, Electrical conduction and hydrogen permeation through mixed proton–electron conducting strontium cerate membranes, Solid State Ionics, 130 (2000) 149-156.

[91] N. Agmon, The Grotthuss mechanism, Chemical Physics Letters, 244 (1995) 456-462.

[92] Kreuer KD, Dippel Th, Hainovsky N, M. J, Proton conductivitycompounds and their structural and chemical Berichte der Bunsengesellschaft für Physikalische Chemie, 96 (1992) 1736-1742.

[93] C. Chipot, L.G. Gorb, J.L. Rivail, Proton Transfer in the Mono- and the Dihydrated Complexes of HF and HCl: An MP2/6-31+G ab Initio Study in the Self-Consistent Reaction Field Model of Solvation, The Journal of Physical Chemistry, 98 (1994) 1601-1607.

[94] K. Swierczek, W. Skubida, E3S Web of Conferences Energy and Fuels, 2017, pp. 01044.

[95] W. Münch, G. Seifert, K.D. Kreuer, J. Maier, A quantum molecular dynamics study of the cubic phase of $BaTiO_3$ and $BaZrO_3$, Solid State Ionics, 97 (1997) 39-44.

[96] I.M. S, Ionic transport in ABO(3) perovskite oxides: a computer modelling tour, Journal of Materials Chemistry, 10 (2000) 1027-1038.

[97] M. Cherry, M.S. Islam, J.D. Gale, C.R.A. Catlow, Computational studies of proton migration in perovskite oxides, Solid State Ionics, 77 (1995) 207-209.

[98] K.D. Kreuer, On the development of proton conducting materials for technological applications, Solid State Ionics, 97 (1997) 1-15.

[99] Lorenzo Malavasi, C.A.J.F. and, M.S. Islam, Oxide-ion and proton conducting electrolyte materials for clean energy applications: structural and mechanistic features, Chemical Society Reviews, 39 (2010) 4370–4387.

[100] S.J. Stokes, M.S. Islam, Defect chemistry and proton-dopant association in $BaZrO_3$ and $BaPrO_3$, Journal of Materials Chemistry, 20 (2010) 6258-6264.

[101] A.R. Potter, R.T. Baker, Impedance studies on Pt|$SrCe_{0.95}Yb_{0.05}O_3$|Pt under dried and humidified air, argon and hydrogen, Solid State Ionics, 177 (2006) 1917-1924.

[102] M.J. Scholten, J. Schoonman, J.C. van Miltenburg, H.A.J. Oonk, Synthesis of strontium and barium cerate and their reaction with carbon dioxide, Solid State Ionics, 61 (1993) 83-91.

[103] K.H. Ryu, S.M. Haile, Chemical stability and proton conductivity of doped $BaCeO_3$–$BaZrO_3$ solid solutions, Solid State Ionics, 125 (1999) 355-367.

[104] L. Yang, S. Wang, K. Blinn, M. Liu, Z. Liu, Z. Cheng, M. Liu, Enhanced Sulfur and Coking Tolerance of a Mixed Ion Conductor for SOFCs: Science, 326 (2009) 126-129.

[105] R. Reijers, W. Haije, Literature review on high temperature proton conducting materials, Energy research Centre of Netherland, 2008.

[106] K.D. Kreuer, Proton-Conducting Oxides, Annual Review of Materials Research, 33 (2003) 333-359.

[107] E. Kendrick, M.S.I. and, P.R. Slater., Investigation of Proton Conduction in Novel Gallates, 7th European Solid Oxide Fuel Cell Forum,Lucerne, 2006.

[108] Y.a. Yoo, N. Lim., Development of Proton Conductor-Based Reversible SOFCs, 8th European Solid Oxide Fuel Cell Forum, Lucerne, 2008.

[109] S. Noirault, S.Celerier, O.Joubert, M.T.C. and, Y.Piffard., Incorporation of water and fast proton conduction in the inherently oxygen-dericient compound $La_{26}O_{27}(BO_3)_8$, Adv.Mat, 19 (2007) 867-870.

[110] H. Matsumoto, M. Okubo, S. Hamajima, K. Katahira, H. Iwahara, Extraction and production of hydrogen using high-temperature proton conductor, Solid State Ionics, 152–153 (2002) 715-720.

[111] M. Tanaka, K. Katahira, Y. Asakura, T. Uda, H. Iwahara, I. Yamamoto, Hydrogen Extraction Using One-end Closed Tube Made of $CaZrO_3$-based Proton-conducting Ceramic for Tritium Recovery System, Journal of Nuclear Science and Technology, 41 (2004) 61-67.

[112] N. Taniguchi, T. Kuroha, C. Nishimura, K. Iijima, Characteristics of novel $BaZr_{0.4}Ce_{0.4}In_{0.2}O_3$ proton conducting ceramics and their application to hydrogen sensors, Solid State Ionics, 176 (2005) 2979-2983.

[113] V. Thangadurai, W. Weppner, Mixed potential protonic–electronic conductivity in the Dion–Jacobson-type layered perovskites in hydrogen-containing atmosphere and their application in ammonia sensors, Solid State Ionics, 174 (2004) 175-183.

[114] U. Balachandran, T.H. Lee, S.E. Dorris, Hydrogen production by water dissociation using mixed conducting dense ceramic membranes, International Journal of Hydrogen Energy, 32 (2007) 451-456.

[115] S. Hamakawa, L. Li, A. Li, E. Iglesia, Synthesis and hydrogen permeation properties of membranes based on dense $SrCe_{0.95}Yb_{0.05}O_{3-\alpha}$ thin films, Solid State Ionics, 148 (2002) 71-81.

[116] J.W. Phair, S.P.S. Badwal, Review of proton conductors for hydrogen separation, Ionics, 12 (2006) 103-115.

CHAPTER 2

Chapter 2: Experimental methods

This chapter provides a brief summary of the preparation methodologies for bulk ceramics, synthesized via conventional solid state and novel vacuum-aided solid state reaction methods. This chapter also deals with the characterization of the compounds prepared for their structural, homogeneity of the dopant introduction, morphological and electrical properties. This chapter, in addition furnishes the design of the hydrogen separation set up built in-house.

2.1 Powder synthesis techniques

2.1.1 Solid state reaction (SSR) or ceramic method

The simplest and most common way of preparing solids is the ceramic method, [1] which involves grinding powders of oxides, carbonates, oxalates or other compounds containing the relevant metals and heating the mixture at the desired temperature, generally after pelletizing the material. The process comprises stoichiometric composition and the homogenization by grinding of solid precursors using pestle and mortar, aided with a volatile solvent such as acetone or isopropyl alcohol. The dried homogeneous mix is pelletized using a hydraulic press to improve the number of crystallite faces in direct contact mutually. The thermal treatments of the precursor pellets with intermediate grindings bring some surfaces in contact and thus accelerate the reaction rate to result into an enchanced yield of the products [2, 3].

The solid-state reaction between the constituent components is initiated by the transport of reactants to the interface and phase boundary reaction at the point of their mutual contact. Thermodynamic and kinetic aspects play a key role in the reaction progress [2]. The three factors that influence the rate of the reaction are

1) area of contact between the reacting solids (surface area)
2) rate of nucleation of the product phase and
3) rates of diffusion of ions through the various phases and especially through the product phase

As the reaction is in progress while heating, reactants react to form a layer of product nuclei. Further, nucleation is rather difficult, probably due to a large amount of structural reorganization such as bond cleavage / reformation involved during the product formation. In the present studies, all the pristine and ytterbium substituted zirconates of calcium and strontium perovskites were prepared by this conventional method, expressed by the general equation 2.1 as shown below.

$$MCO_{3(s)} + (1-x)ZrO_2 + \frac{x}{2}Yb_2O_{3(s)} \rightarrow MZr_{(1-x)}Yb_xO_{3-x/_2} + CO_{2(g)} \qquad (2.1)$$

where M= Ca, Sr ; x= 0 – 0.2

2.1.2 Modified solid state reaction (MSSR) method

The conventional solid-state reactions are generally suitable for the synthesis of oxide compounds, which is insensitive to the ambient i.e. CO_2, H_2O, etc. in the atmosphere. To process such kind of sensitive compounds, a novel vacuum-aided solid state method is developed. This method ensures the favorable condition for the forward reaction by continuous removal of the gaseous by-product i.e. CO_2 in the preparation of $BaThO_3$ using the precursors such as $BaCO_3$ and ThO_2 (equation 2.2). In the present study, modified solid state reaction (MSSR) method is followed to synthesize the pristine, ytterbium substituted barium thorate and zirconium substituted barium thorate, using the precursor such as barium carbonate, thorium oxalate and ytterbium oxide.

$$BaCO_{3\,(s)} + ThO_{2\,(s)} \rightarrow BaThO_{3\,(s)} + CO_{2\,(g)} \qquad (2.2)$$

2.2 Materials characterization techniques

Different physiochemical techniques used for characterizing the aforementioned powder samples are discussed below.

2.2.1 Neutron Activation Analysis (NAA)

In 1934 I. J. Curie and F. Joliot discovered the nuclear activation by bombarding naturally occurring alpha particles with Al, Mg and B. Neutron activation analysis is an effective non-destructive radio analytical technique for qualitative as well as quantitative analysis of various elemental isotopes in a compound or samples especially for trace level analysis with detection limit as low as ppm to ppb range [4]. The high sensitivity can be attributed to irradiation at high neutron flux (10^{11} to 10^{15}cm^{-2}s^{-1}) available from research reactors and measurements of radiation especially, like gamma rays from the sample using high efficiency and high resolution high purity germanium (HPGe) detector coupled to multichannel analysers (MCA). Neutron activation analysis technique is based on irradiation of sample with neutrons, available from different neutron sources and subsequent measurement of the induced radioactivity (β, γ) for the determination of the concentration of an element by the measurement of (i) prompt gamma NAA (PGNAA) and (ii) delayed gamma NAA [5]. The NAA can be carried out without or with chemical separation [5, 6]. If the elements can be determined without any chemical treatment, the method is called instrumental neutron activation analysis (INAA). This method requires minimal sample handling and has no reagent blank correction. When an element has good nuclear properties and experiences negligible interferences, the INAA method is chosen, owing to its simplicity.

NAA can be carried out by three different methods viz. (i) Absolute method, (ii) Relative method and (iii) k_0 NAA method. In this study the relative method is used to evaluate the homogeneous distribution of low concentrations of Yb_2O_3 in $CaZr_{1-x}Yb_xO_{3-\delta}$ (where x = 0.001) using INAA, appropriate proportion of $CaCO_3$, ZrO_2 and Yb_2O_3 was ground and made into slurry in ethanol medium. It was completely dried under IR and ground again. An attempt was made to dissolve the compound $CaZr_{1-x}Yb_xO_{3-\delta}$ (x=0.1), and found to be insoluble, even in HF, due to the presence of zirconium in it. Under this condition, estimation of ytterbium by other techniques (ICP-OES) was not possible. Thus, neutron activation analysis was selected, in which the powder sample can be directly used as such for irradiation, followed by subsequent measurement of induced radioactivity for the determination of the concentration of an element.

Around 25–50 mg samples were accurately weighed in triplicate in cellophane paper and taken in cleaned polythene covers with heat sealing. A solution of Yb (1000 ppm) was taken as relative standard in a filter paper with polythene cover, dried and heat sealed. The samples and standards were irradiated simultaneously at 20 kW for 6 h at pneumatic fast transfer system (PFTS) position of Kalpakkam Mini reactor (KAMINI) at IGCAR, Kalpakkam. This method is simple and does not need the nuclear and reactor based parameters. The concentration of Yb was calculated by the relative method of INAA using the Equation 2.3 as given below:

$$m_{x,sample} = m_{x,std} \cdot \frac{[C_P]_{x,sample}}{[C_P]_{x,std}} \cdot \frac{D_{std}}{D_{sample}} \qquad (2.3)$$

where, $m_{x,std}$ is mass of the element in standard, $[C_P]_{x,std}$ and $[C_P]_{x,sample}$ are the activities of standard and sample respectively and D is the decay correction factor (exp $(-\lambda t_d)$), λ is the decay constant, and t_d is the decay time.

Neutron activation analysis has the following advantages:

NAA is powerful isotope specific nuclear analytical technique for simultaneous determination of elemental composition of major, minor and trace elements in diverse matrices. This technique is capable of yielding high analytical sensitivity, precision and low detection limits (ppm –ppb). Due to high penetration power of neutrons and gamma rays, NAA experiences negligible matrix effects in the samples of different origins.

2.2.2 X-ray Diffraction (XRD)

X-ray diffraction is the most powerful technique used for the characterization of crystalline materials to determine the crystal structures, based on the diffraction of characteristic X-ray beam on the crystalline solid [2, 3, 7-9]. Crystalline solid is solid materials whose constituents i.e. atoms or ions are arranged in highly ordered manner with inter-planar spacing in the order of angstrom. Because of the periodic nature of the internal structure, it is possible for the crystals to act as three dimensional grating to radiation. The high intense and very narrow characteristic X-rays are used for diffraction experiments. In general, K_α lines are used for XRD. The most common target metal in X-ray tube is copper whose characteristic wavelength for K_α radiation is 1.5418 Å. Other metal targets used in X-ray generating tubes include Cr (K_α = 2.29 Å), Fe (K_α = 1.94 Å), Co (K_α = 1.79 Å) and Mo (K_α = 0.71 Å).

Constructive interference of X-rays scattered by parallel planes of atoms will produce a diffraction peak when Bragg's law is satisfied [10, 11]. The relation between the wavelength of electromagnetic radiation (λ) to the diffraction angle (θ) and the spacing between these parallel planes (d) in a crystalline sample is given by Bragg's law, as shown in the equation 2.4

$$n\lambda = 2d\sin\theta \tag{2.4}$$

where *n* is order of diffraction, λ is wavelength of the incident X-ray, *d* is inter-planar spacing and θ is angle of incidence. The schematic representation of Bragg condition of diffraction of X – rays by a crystal is shown in Figure 2.1 [12]

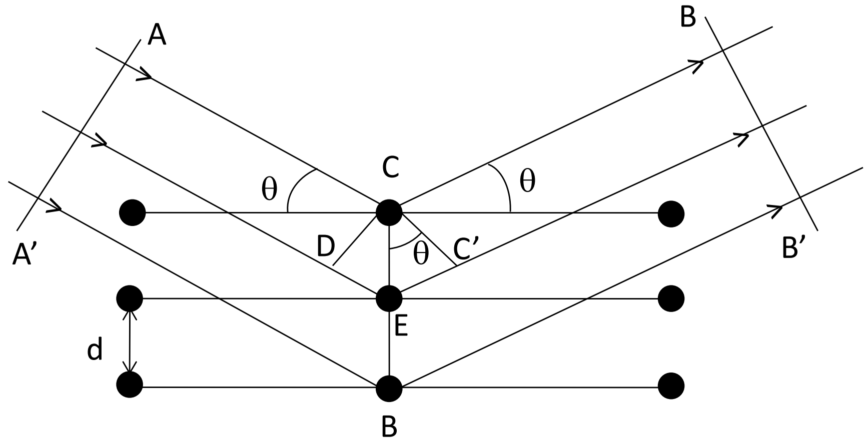

Figure 2. 1 Schematic diagram of diffraction of X-rays by a crystal (Bragg Condition)

Typical X- ray diffractometer consists of X-ray tube, a sample holder and detector. Samples can be analyzed in both single crystal and powder form. The collimated X-rays are directed to the sample, and the diffraction occurs, which can be detected by a movable detector. The detector records and processes the X-ray signal and converts into a count rate, which is finally fed to the computer.

The scattered X-rays by an atom as a resultant of wave scattered by each electron in the atom. Thus, the scattering factor of an atom is proportional to its atomic number, which is proportional to the intensity of the scattered X-rays.

The X-ray diffraction pattern obtained is a fingerprint of that particular compound. Pure or different phases present in the sample can be identified by comparing the diffraction pattern with the standard patterns known as Powder Diffraction Files (PDF) collected and maintained by Joint Committee of Powder Diffraction Standards (JCPDS).

In the present work, the room temperature diffraction patterns of all nominal compositions of $CaZr_{1-y}Yb_yO_{3-\delta}$ (y = 0 - 0.2) and $SrZr_{1-y}Yb_yO_{3-\delta}$ (y =0 - 0.2) samples were recorded at a step size of 0.01° using Cu K_α radiation (1.5418 Å) of M/s Siemens # D 500, Germany diffractometer. The diffraction patterns of nominal composition of pristine, $BaTh_{1-y}Yb_yO_{3-\delta}$ (y = 0 - 0.2), $BaTh_{1-x}Zr_xO_3$ (x = 0 - 0.4) and $BaTh_{1-x-y}Zr_xYb_yO_{3-\delta}$ (y = 0.1 and x = 0.05) samples were recorded at 0.01° using Cu K_α radiation (1.5418 Å) of M/s GNR Explorer, Italy.

2.2.3 Scanning electron microscopy (SEM)

Scanning electron microscopy is one of the most versatile techniques for the examination and analysis of the microstructure morphology of solid samples. It enables to observe and characterize materials on nanometer to micrometer scale [13, 14].

An accelerated electron beam is used to scan the surface of the specimen. Interaction of electron beam with specimen, phenomena such as absorption, reflection, backscatter, diffraction, and emission of low energy secondary electron and X-rays occur. The emission of backscattered electrons and secondary electrons is characteristic of the specimen under study and depend upon its topography and composition. Electrons are collected owing to these effects converted into electrical signals, amplified and displayed as modulations of brightness on the cathode ray tube. The resultant image is determined by the ratio of the distance travelled by the recording beam in a given time interval to that travelled by the synchronously deflected scanning beam in the same time interval.

The elemental composition at the surface of the specimen can be determined by SEM coupled with energy dispersive X-ray spectroscopy (EDS). Interaction of electron beam with the surface atoms of the specimen causes ejection of electrons from the inner shells of the atoms. The resultant vacancies in the inner shells are filled up by the fall of electron from the outer shells, with emission of characteristic X-rays. The elemental composition can be determined by measuring the characteristic X-rays. As the penetration depth of the electron beam is very low, it can interact only with the surface atoms and hence the information obtained by this method corresponds to very narrow surface dimensions. In the present study, SEM analysis was performed to study the surface morphology of pristine and ytterbium doped $CaZrO_3$, $SrZrO_3$ and $BaThO_3$ samples using SEM-EDS (M/s. Philips, Netherlands, Model No. XL30).

2.2.4 Helium densitometry for density measurements

A gas pycnometer is the device used for measuring the density or more accurately the volume of the solids [15-18]. This is working based on the gas displacement method, and a well known relationship between the pressure and volume (Boyle's Law). Gas expansion pycnometer is generally known as constant volume gas pycnometer. It consists of two chambers; one to hold the sample and a second chamber of fixed known internal volume referred to as the reference volume or added volume. Figure 2.2 shows the schematic diagram of helium pycnometer. The method involves measuring the change in the pressure required to increase or decrease a given volume of gas by a known amount and repeating the measurement when a portion of the gas volume is occupied by a known weight of the powdered solid. The volume of the sample is calculated using the relation as follows

$$V_s = V_c + \frac{V_r}{1-\frac{P_1}{P_2}} \qquad (2.5)$$

where ,V_s – Sample volume

V_c – Empty sample chamber volume (known from prior calibration step)

V_r – Reference chamber volume (known from prior calibration step)

P_1 – Initial pressure (sample chamber only) and

P_2 – Final pressure (after expansion of the gas in to the combined volumes of sample and reference chamber)

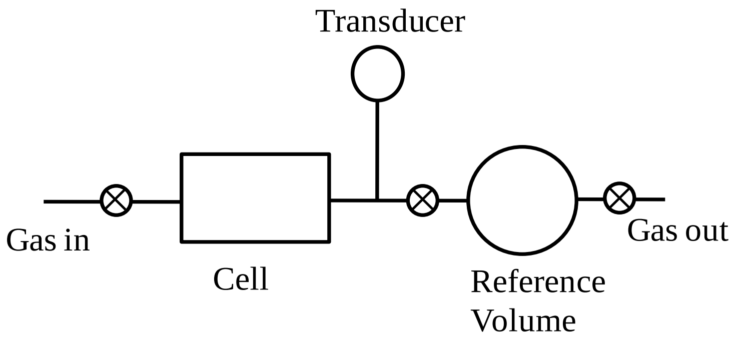

Figure 2. 2 Schematic diagram of helium pycnometer

In the present study, the densities of the sintered pellets of $BaTh_{1-x}Yb_xO_{3-\delta}$ (x = 0–0.2) were obtained by helium pycnometer method (Model Ultra Pycnometer 1000 of M/s Quantachrome Instruments, USA) by gas diffusion.

2.2.5 Attenuated total reflection spectroscopy

Infrared spectroscopy is a study of the interaction of radiation with molecular vibrations which can be used for a wide range of sample types either in bulk or in microscopic amounts over a wide range of temperatures and physical states. Beside the conventional IR spectroscopy of measuring light transmitted from the sample, the reflection IR spectroscopy was developed using a combination of IR spectroscopy with reflection theories. In the reflection spectroscopy techniques, the absorption properties of a sample can be obtained from the reflected light. Attenuated total reflection spectroscopy utilizes total internal reflection phenomenon [19]. An internal reflection occurs when a beam of radiation enters from a more dense medium (with a higher refractive index, n_1) into a less-dense medium (with a lower refractive index, n_2), the fraction of the incident beam reflected increases with the rise of the angle of incidence. When the angle of incidence is greater than the critical angle θ_c (where θ_c is a function of refractive index of two media), all incident radiations are completely reflected at the interface, which results in total internal reflection, as shown in Figure 2.3 [19]. In ATR spectroscopy a crystal with a high refractive index and excellent IR transmitting properties is used as internal reflection element (IRE, ATR crystal) and is placed in close contact with the sample. The beam of radiation propagating in IRE undergoes total internal reflection at the interface IRE sample and provided the angle of incidence at the interface that exceeds the critical angle θ_c. Total internal reflection of the light at the interface between two media of different refractive index creates an "evanescent wave" that penetrates into the medium of lower refractive index [19].

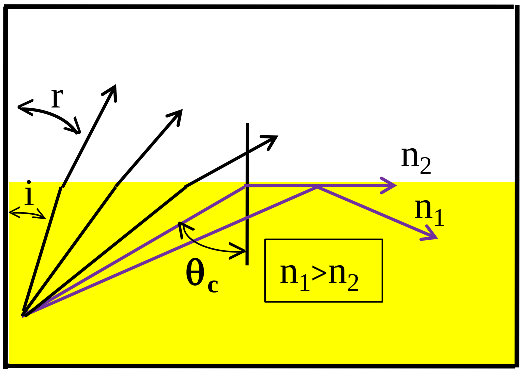

Figure 2. 3 Schematic illustration of total internal reflection

An ATR spectrum can be obtained by measuring the interaction of the evanescent wave with the sample. If an absorbing material is placed in contact with ATR crystal, the evanescent wave will be absorbed by the sample and its intensity is reduced (attenuated) in regions of the IR spectrum where the sample absorbs, thus, less intensity can be reflected (attenuated total reflection). The resultant attenuated radiation as a function of wavelength produces an ATR spectrum which is similar to the conventional absorption spectrum except for the band intensities at longer wavelengths. This difference is attributed to the dependency of the penetration depth (dp) on wavelength: at longer wavelength, the evanescent wave penetrates deeper into the sample, thus, the absorption bands at longer wavelengths are relatively more intense than those of shorter wavelengths. This results into a greater absorption on the longer wavelength side of an absorption band, contributing to band distortion and band broadening. In the present study deuterium and carbon dioxide exposed samples were analyzed using IR spectroscopy (M/s Bruker, Model-Tensor-II ATR).

2.2.6 Impedance spectroscopy

Impedance spectroscopy is a powerful technique for characterizing electrical properties of the materials and their interfaces with electronically conducting electrodes. It is a perturbation technique in which the system is perturbed by applying a small amplitude sinusoidal alternating voltage as a function of frequency and the response of the system is measured [20-22]. The applied potential and the output current from the system are given by equations:

$$E = E_0 \sin(\omega t) \tag{2.6}$$

$$I = I_0 \sin(\omega t + \emptyset) \tag{2.7}$$

The output current has the same angular frequency ω but, differs in amplitude and phase from the voltage signal. Impedance (Z) can be defined as the resistance to the flow of current and it can be obtained as the ratio of applied voltage to the resultant current.

$$Z = \frac{E}{I} = \frac{E_0 \sin(\omega t)}{I_o \sin(\omega t + \phi)} = Z_0 \frac{\sin(\omega t)}{\sin(\omega t + \phi)} \qquad (2.8)$$

Using Euler's relationship,

$$\exp(j\phi) = \cos\phi + j\sin\phi \qquad (2.9)$$

it is possible to express impedance as a complex function. The potential is described as:

$$E = E_0 \exp(j\omega t) \qquad (2.10)$$

and the current response as

$$I = I_0 \exp(j\omega t - \phi) \qquad (2.11)$$

Impedance can be then represented as a complex number,

$$Z(\omega) = \frac{E}{I} = Z_0 \exp(j\phi) = Z_0(\cos\phi + j\sin\phi)$$

$$= Z_0 \cos\phi - jZ_0 \sin\phi = Z^{'} - jZ^{''} \qquad (2.12)$$

where, $Z^{'} = Z_0 \cos\phi$, $Z^{''} = Z_0 \sin\phi$ and $j = \sqrt{-1}$. $Z^{'}$ and $Z^{''}$ are known as the real and imaginary parts of the impedance. The phase difference (ϕ) is given by

$$\phi = \tan^{-1}\left(\frac{Z^{''}}{Z^{'}}\right) \qquad (2.13)$$

Typical electrical systems consist of elements that can be described by various combinations of resistors, capacitors and inductors. When the material with magnetic properties, inductor can be envisaged, otherwise electrical systems normally behaves between a capacitor and a resistor. The contributions of the capacitive and resistive components vary with frequency.

For a pure resistor, impedance is equal to its resistance R, i.e.

$$|Z| = R \tag{2.14}$$

There is no phase shift and the impedance value is independent of frequency.

Impedance of a capacitor (C) is 90° out of phase and it is given by:

$$|Z| = \frac{-j}{\omega C} \tag{2.15}$$

Impedance of a capacitor is dependent on frequency and it is larger for a lower frequency. The resistive and capacitive components of an electrochemical system can be correlated to structural and chemical features of the system. Study of impedance therefore, can provide information on the electrical behavior. As the contribution of capacitance and resistance vary with frequencies, impedance measurements at a range of frequencies are performed and data thus obtained are used to determine the components of the system.

For a circuit that consists of a resistor and a capacitor connected in parallel (RC parallel), total impedance of the circuit can be obtained as follows:

$$\frac{1}{Z_{total}} = \frac{1}{Z_R} + \frac{1}{Z_C} = \frac{1}{R} + \frac{\omega C}{-j} \tag{2.16}$$

Thus, $Z_{total} = \dfrac{-jR}{\omega RC - j}$ (2.17)

The above expression can be rearranged to get

$$Z_{total} = \frac{1 - j\omega R^2 C}{1 + \omega^2 R^2 C^2} \tag{2.18}$$

From this equation, the real and imaginary parts of impedance can be resolved and hence,

$$Z_{\mathrm{Real}} = \frac{R}{1+\omega^2 R^2 C^2} \tag{2.19}$$

$$Z_{imaginary} = \frac{R^2 C\omega}{1+\omega^2 R^2 C^2} \tag{2.20}$$

By rearranging the impedance results for the RC parallel circuit, it can be shown that

$$(Z_{real} - \frac{R}{2})^2 + Z^2{}_{imaginary} = \frac{R^2}{4} \tag{2.21}$$

which is an equation of a circle, with the center at (0, R/2) and the radius equal to R/2.

By plotting the real part of impedance along the X-axis and imaginary part along the Y-axis, one gets a Nyquist plot as shown in Fig. 2.4. As long as the axes are of equal scale, the appearance of the semicircle in the Nyquist plot signifies the existence of a parallel RC circuit. Again, ω which corresponds to the frequency at the apex of the semicircle is inversely proportional to RC, where RC is the time constant. A semicircle is characteristic of a single time constant. The value of the resistance R can be determined easily and directly from the diameter of the semicircle.

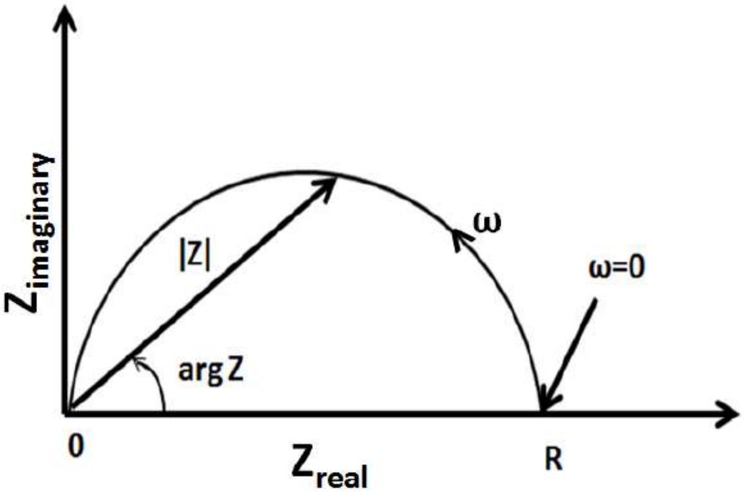

Figure 2. 4 Typical representation of Nyquist plot

Another popular representation method is the "Bode plot”. Here the impedance is plotted with log frequency (log ω) on the X-axis and both the absolute value of the impedance ($|Z| = Z_0$) and phase-shift on the Y-axis. Unlike the Nyquist plot, the Bode plot explicitly exhibit the behavior of R, C and L components of a material as a function of frequency. A typical representation of Bode plot is shown in Figure 2.5.

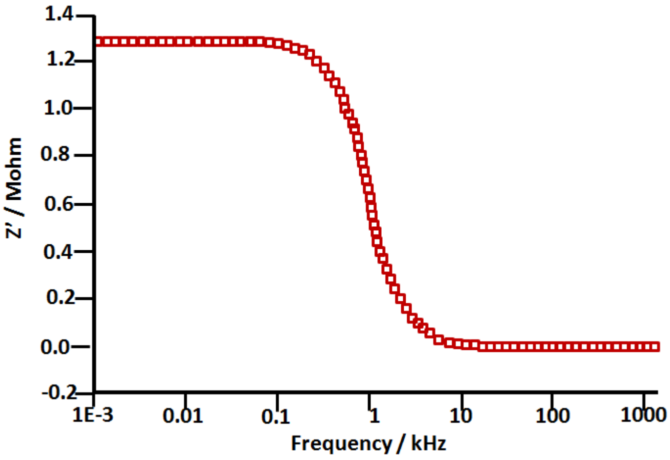

Figure 2. 5 Typical representation of Bode plot

At an applied ac voltage, charge transfer across a sample consists of various processes at the electrode-sample interfaces and in the bulk of the sample. Processes at the electrode-sample interface could involve adsorption, diffusion and dissociation of adsorbed species and charge transfer to or from the electrode. Charge transport across the bulk of a polycrystalline sample can be a combination of transport through grains and grain boundaries and could involve different ions also. The charge transport processes have different time constants individually and hence during an ac measurement of conductivity, they get separated in the frequency domain. The ordering of the semicircles depends on their time constants. The circle with the shorter time constant appears on the left side of the Nyquist plot. Each arc in the measured impedance can be correlated to the various elementary processes occurring in the material which can be appreciated by means of equivalent electrical circuits. The equivalent electrical circuit of a ceramic electrolyte, consisting of a series combination of parallely connected resistors (R) and capacitors (C) is shown in Figure 2.6. The corresponding impedance spectrum is shown in Figure 2.7. The first arc (bulk) is usually observed at low and medium temperatures and proportional to the sample length and density. It is attributed to the bulk or grain interior process. The low frequency arc (interface) is observed at high temperatures. This is inversely proportional to the electrode area and is attributed to the electrode-sample interfacial process. The impedance due to this is termed as Warburg impedance and is observed as a spike in the impedance spectrum. The intermediate arc (grain boundary) which is observed at low and medium temperatures is associated with the conductance and microstructural effects at the grain boundary.

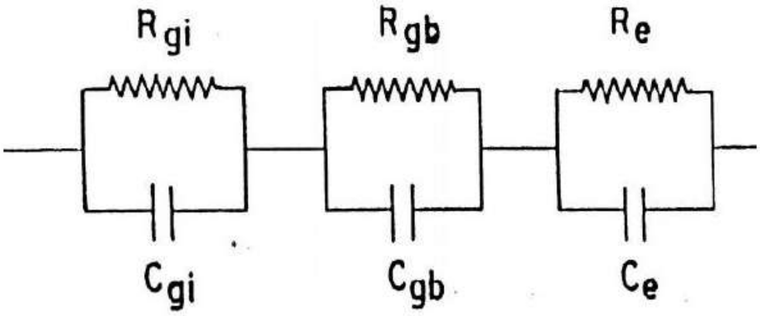

Figure 2. 6 Equivalent electrical circuit of a ceramic electrolyte, consisting of a series combination of parallely connected resistors (R) and capacitors (C)

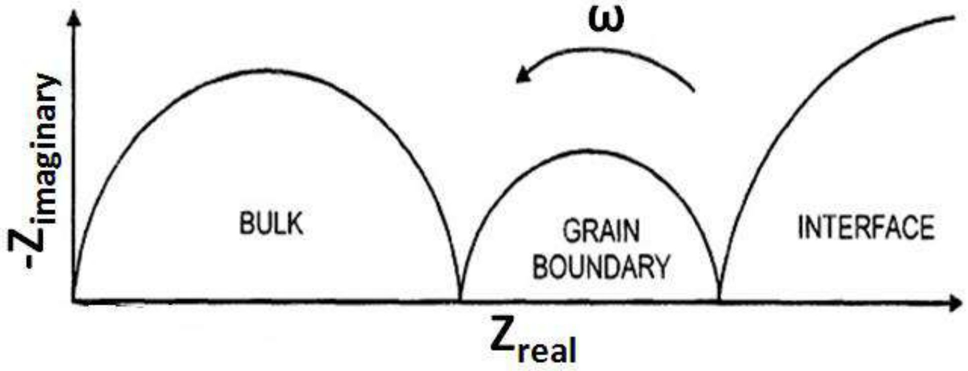

Figure 2. 7 Impedance spectrum of a solid ionic conductor

In the present study, the variation of conductivity with temperature for the pristine and Yb substituted $CaZrO_3$, $SrZrO_3$, $BaThO_3$ and $BaTh_{1-x}Zr_xO_3$ were carried out by impedance measurements in different ambience i.e. air, oxygen, argon containing 80 ppm hydrogen and hydrogen using the conductivity cell schematic and digital photograph as shown in Figure 2.8 & 2.9 respectively.

2.2.7 The apparatus built in-house

(i) Conductivity cell

The conductivity cell consisted of two platinum electrical leads which were welded to platinum discs of identical dimension. The sintered sample pellet of known dimension was placed between the platinum discs by a spring loading arrangement. A K- type thermocouple was positioned close to the sample pellet, so that sample temperature could be accurately measured. Entire assembly was accommodated in a quartz chamber which, in turn was positioned in a furnace for heating. Electrical conductivity was measured using a frequency response analyzer (Model SI 1225, Solartron, M/s Schlumberger, UK) coupled with an electrochemical interface (Model

1286, Solartron, M/s Schlumberger, UK) in the frequency range of 1 MHz to 100 Hz and the temperature range from 573 -973 K under aforementioned ambient conditions (section 2.2.7).

The impedance data obtained at each temperature was fitted using the software Zview® [23]. The bulk resistance of the material was obtained by fitting a semicircle to the experimentally obtained Nyquist plot. By incorporating the geometrical dimensions of the sample pellet, conductivity (σ) of the sample at the experimental temperature (T) was determined. Arrhenius plot for conductivity was then obtained by plotting $\log\sigma$ as a function of reciprocal temperature (1/T). Activation energy was deduced from the slope. A change in the slope in Arrhenius plot indicates the difference in the conduction mechanism and / or a phase change.

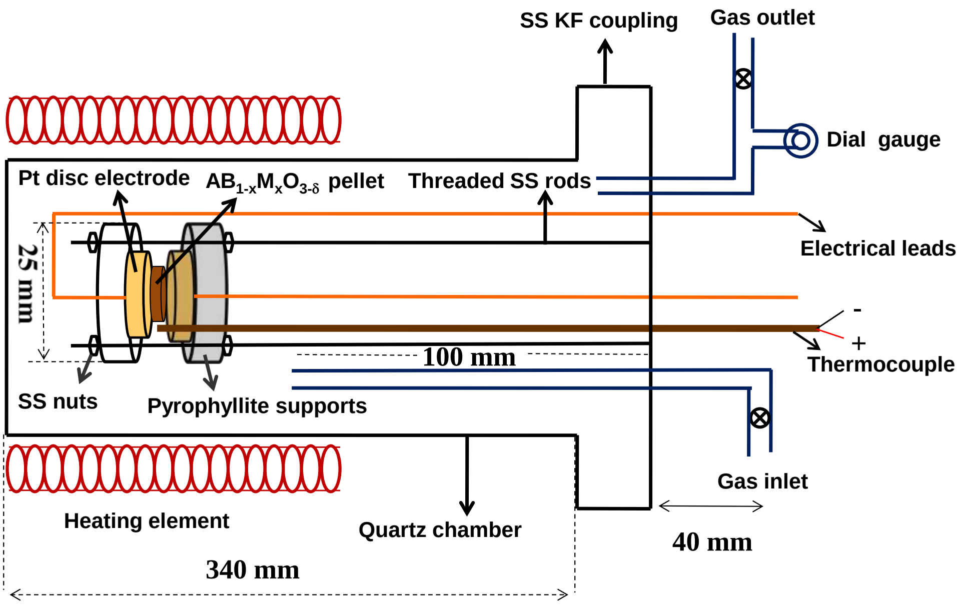

Figure 2. 8 Schematic of the conductivity cell

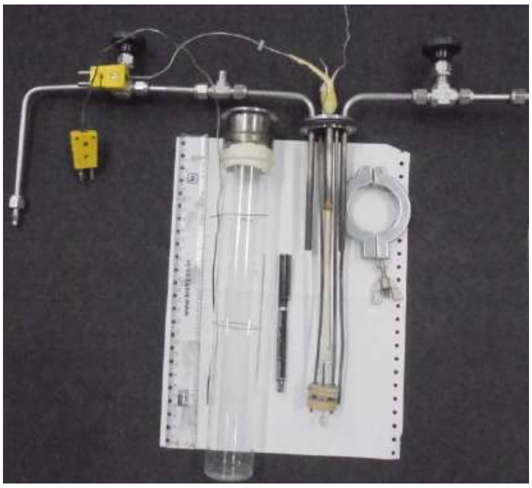

Figure 2. 9 Digital photograph of the conductivity cell

(ii) Hydrogen pumping set up

Figure 2.10 & 2.11 respectively, shows the schematic and digital photograph of hydrogen pumping apparatus, in-house fabricated using stainless steel and welded with knife edge flanges. This apparatus consists of outer and inner chambers. The pellet (dimension 2.5 mm thickness and ~12 mm diameter) was placed into the ferni alloy and sealed using glass sealant. The sealing was performed by heating at 1123 K for 15 minutes under ultra pure argon atmosphere with controlled heating rate of 2 K / min. The pellet attached ferni alloy was welded into the inner chamber. The apparatus was leak tested by helium leak detector. The platinum leads are contact in with pellet outside (anode) and inside (cathode) with spring loading arrangement. A K - type thermocouple was positioned close to the sample pellet, so that sample temperature could be accurately measured. The commercially procured standard hydrogen in argon gas mixture was filled in the outer chamber and the hydrogen pumping study was carried out using the precision source/measure unit (Keysight B2912 A). The separated hydrogen gas was analysed by injecting the gas sample from the inner chamber into a hydrogen sensor [24-26] developed in-house.

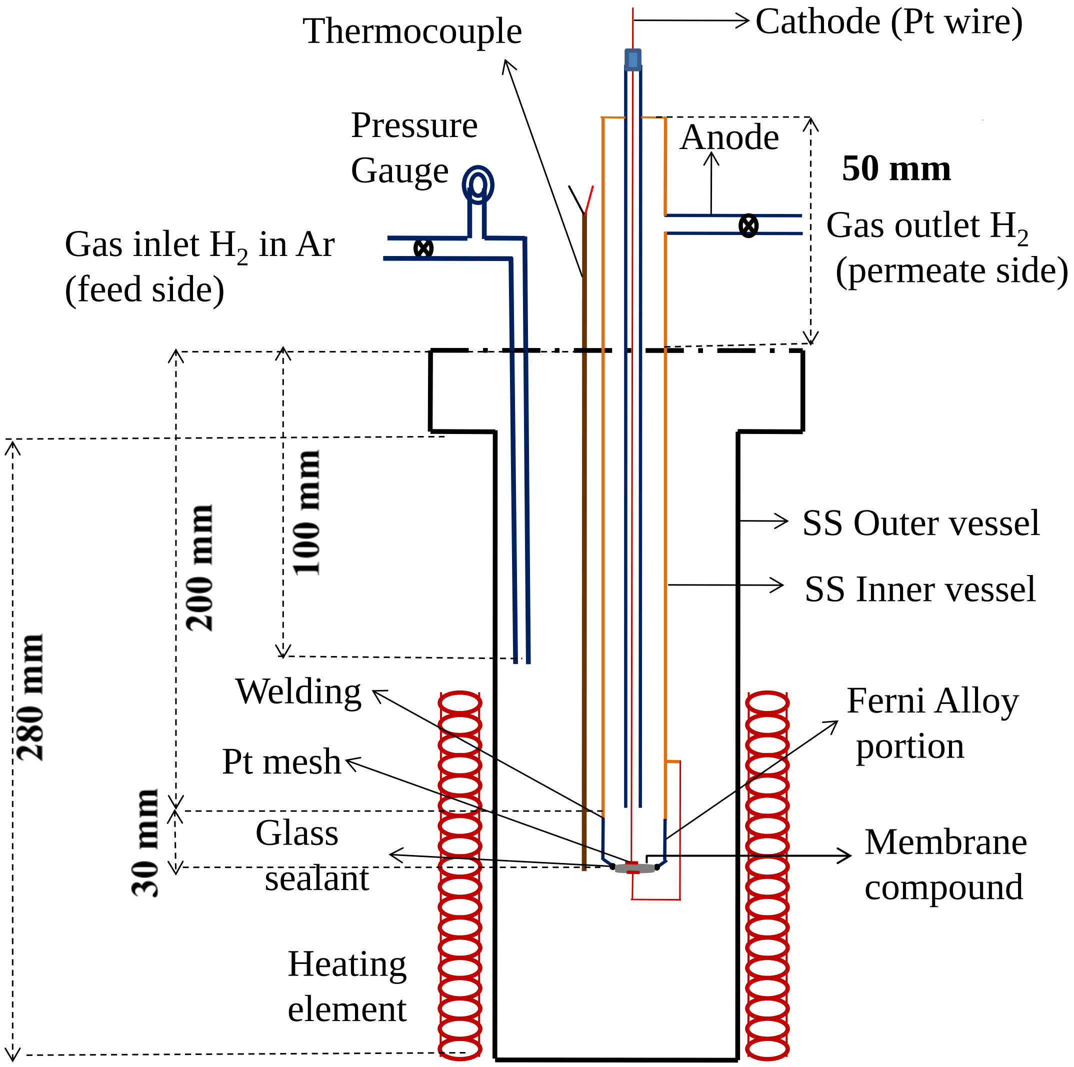

Figure 2. 10 Schematic diagrams of hydrogen extraction apparatus

Figure 2. 11 Digital photograph of hydrogen extraction apparatus

2.3 References

[1] C.N.R. Rao, K. Biswas, Ceramic methods in essentials of inorganic materials synthesis, John Wiley & Sons Inc, Hoboken, NJ 2015.

[2] A. R. West, Solid state chemistry and its applications, John Wiley & Sons Inc, Singapore, 2003.

[3] L.E Smart, E.A. Moore, Solid State Chemistry: An Introduction, Third Edition:, Taylor & Francis 2005.

[4] P.R. Bhagat, R. Acharya, A.G.C. Nair, A.K. Pandey, N.S. Rajurkar, A.V.R. Reddy, Estimation of iodine in food, food products and salt using ENAA, Food Chemistry, 115 (2009) 706-710.

[5] W.D. Ehmann, D. E. Vance, Radiochemistry and Nuclear methods of Analysis, Wiley Interscience Publication, John Wiley & Sons, Inc, New York, 1991.

[6] The applications of research reactors, IAEA-TECDOC-1234, IAEA, Vienna, 1999.

[7] R.A. Meyers, Encyclopedia of analytical chemistry, (X-ray technique: Overview), John Wiley & Sons Ltd, Chichester, 2000.

[8] S.E. Dann, Reactions and characterization of solids, The Royal Society of Chemistry 2002.

[9] B.D.Cullity, S.R.Stock, Elements of X-ray diffraction, Prentice Hall, NJ, 2001.

[10] L.V. Azaroff, Elements of X – ray crystallography, McGraw Hill, New York 1968.

[11] B.D. Cullity, S.R. Stock, Elements of X-ray diffraction, , Prentice Hall,, NJ, , 2001.

[12] C. Suryanarayana, M.G. Norton, X-Ray Diffraction A Practical Approach, Springer US, New York, 1998.

[13] D.E. Newbury, D.C. Joy, P. Echlen, C.E. Fiori, J.I. Goldstein, Advanced scanning electron microscopy and X-ray microanalysis, Plenum Press, New York, 1986.

[14] K. Mills, J.R. Davis, D.A. Dieterich, Metallography and microstructure, ASM handbook, International Soc. ASM, Material Park, USA, 1998.

[15] J.E. Shea, Apparatus for measuring volumes of solid materials, 1954.

[16] Turner et al., Gas comparison pycnometer, 1978.

[17] Furuse, Volume measuring apparatus and method, 1989.

[18] S. Lowell, J.E. Shields, M.A. Thomas, M. Thommes, Characterization of Porous Solids and Powders: Surface Area, Pore Size and Density, Kluwer Academic Publishers, Netherlands, 2004.

[19] T.M. Theophanides, Infrared Spectroscopy-Materials Science,Engineering and Technology, InTech 2012.

[20] E. Barsoukov, J.R. Macdonald, Impedance Spectroscopy Theory, Experiment, and Applications, A John Wiley & Sons, Inc, New Jersey, 2005.

[21] M.E. Orazem, B. Tribollet, Electrochemical impedance spectroscopy A john wiley & sons, inc, New Jersey, 2008.

[22] P. Vanysek, Introduction to electrochemical impedance, Calgray, 1994.

[23] Z view®-Impedance software, Scribner Associates, Inc, North Carolina, USA.

[24] V. Jayaraman, K.I. Gnanasekar, E. Prabhu, T. Gnanasekaran, G. Periaswami, Preparation and characterisation of $Cr_{2-x}Ti_xO_{3+\delta}$ and its sensor properties, Sensors and Actuators B: Chemical, 55 (1999) 175-179.

[25] V. Jayaraman, E. Prabhu, K.I. Gnanasekar, T. Gnanasekaran, G. Periaswami, Soft-chemical preparation and gas sensing properties of iron and manganese substituted $Cr_{1.8}Ti_{0.2}O_{3+\delta}$, Materials Chemistry and Physics, 86 (2004) 165-175.

[26] E. Prabhu, S. Muthuraja, K.I. Gnanasekar, V. Jayaraman, S. Sivabalan, T. Gnanasekaran, Ammonia sensing properties of thick and thin films of $Ag_6Mo_{10}O_{33}$ and $Cr_{1\cdot8}Ti_{0\cdot2}O_{3+\delta}$, Surface Engineering, 24 (2008) 170-175.

CHAPTER 3

Chapter 3: Behavior of Ytterbium in Calcium and Strontium Zirconate Matrices

3.1 Introduction

Zirconates such as $CaZrO_3$, $SrZrO_3$ and $BaZrO_3$ are promising candidates as high temperature solid electrolytes owing to their high tolerance against ambient gases such as CO_2 and water vapour. They are of potential use in emerging technologies such as fuel cells [1-3] hydrogen pumps [4] hydrogen separators [5] steam electrolyzers and steam pumps [6], hydrogen sensors [7] etc,. Several investigations were reported for the trivalent (e.g. In^{3+}, Sc^{3+}, Y^{3+}) substituted $CaZrO_3$ [3, 8, 9]. Browall and Muller reported that [10] trivalent substituted $SrZrO_3$ showed oxide ion and mixed conduction at high temperature. Shin and coworkers confirmed the dissolution of hydrogen into the single crystal of $SrZrO_3$ substituted with yttrium, by the measurement of infrared and ac conductivity [11]. However, no detailed work was reported for substitution of ytterbium in place of Zr^{4+} in $CaZrO_3$ matrix. In addition, to obtain high hydrogen permeability, the membrane should have high ambipolar conductivity, i.e., simultaneous preparation of high proton conductivity as well as electronic conductivity. This can be attained by (i) the partial substitution of the B-site cations with aliovalent cations, i.e., cations with different oxidation states or (ii) the addition of another phase with inherently high electronic conductivity [12]. This provides the scope to investigate the change in electrical properties of Yb substituted $CaZrO_3$. This chapter deals with preparation and various characterizations such as INAA, XRD, SEM and AC impedance spectroscopy analysis of $AZr_{1-x}Yb_xO_{3-\delta}$ (where A= Ca & Sr) (x=0-0.2).

3.1.1 Studies on $CaZr_{1-x}Yb_xO_{3-\delta}$

In the CaO-ZrO_2 system $CaZrO_3$ is the only compound with the melting point of 2618 K [13]. This compound exists in two polymorphic forms i.e., orthorhombic form is stable up to 2173 K and cubic form is stable at high temperatures (< 2173 K). At room temperature, calcium zirconate has an orthorhombic structure with Pnma space group. According to the crystallographic file (CIF-4571) the structure is shown in Figure 3.1. It is an insulator with a band gap of 5.6 eV [14]. $CaZrO_3$ structure is composed of almost regular ZrO_6 octahedra which are rotated in relation to their position in an ideal cubic perovskite structure. Owing to this rotation, the coordination number of A site i.e., Ca^{2+} ions is reduced from 12 to 8 in disordered $CaZrO_3$.

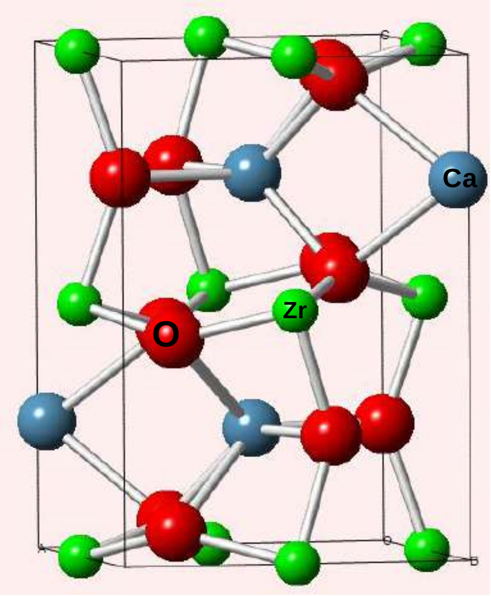

Figure 3. 1 Structure of Calcium zirconate

Lyagaeva et al. [15] reported pure (undoped $CaZrO_3$) does not exist as conductor owing to the small degree of its disordering [16]. However, acceptor – doping (M_2O_3 where M = Sc, Y, Yb etc.) results in the emergence of oxygen vacancies ($V_O^{\bullet\bullet}$), which results in high ionic (oxygen – ionic and protonic) transport of zirconates. This can be expressed by Kröger-Vink notation [17] as follows:

$$M_2O_3(ZrO_2) \rightarrow 2M'_{Zr} + 3O_O^x + V_O^{\bullet\bullet} \qquad (3.1)$$

where, M'_{Zr} is the substitution defect and O_O^x denotes oxygen at the regular site.

The proton defect can be formed by, with as well as without participation of oxygen vacancies in wet and dry hydrogen atmosphere [18] i.e.

$$H_2O + O_O^x + V_O^{\bullet\bullet} \leftrightarrow 2OH_O^{\bullet} \qquad \text{(Wet)} \qquad (3.2)$$

$$H_2(g) + 2O_O^x \leftrightarrow 2OH_O^{\bullet} + 2e^- \qquad \text{(Dry)} \qquad (3.3)$$

Following sections discuss the solid solution formation range of ytterbium in $CaZrO_3$ and the impact of Yb on the physiochemical properties with help of several experimental tools.

3.1.2 Experimental

Nominal compositions, $CaZr_{1-x}Yb_xO_{3-\delta}$ (x = 0 – 0.2) were synthesized using the precursor materials such as of $CaCO_3$ (99.5%), ZrO_2 (99.0%) and Yb_2O_3 (99.5%) by a solid state method described in detail in chapter 2. Details of the physicochemical techniques employed for the characterization of $CaZr_{1-x}Yb_xO_{3-\delta}$ (x = 0 – 0.2) are presented in chapter 2.

3.1.3 Results and Discussion

3.1.3.1 Elucidation of homogeneous distribution of Yb in $CaZrO_3$

In conventional solid state synthesis, precursor materials are physically mixed in presence of some organic volatile solvent. Since the amount of dopant is in very low concentration, it is difficult to obtain the homogeneous powder. The knowledge of the homogeneity is essential prior to the calcination. An attempt was made to dissolve the compound $CaZr_{1-x}Yb_xO_{3-\delta}$ (x=0.1), and found to be insoluble, even in HF, due to the presence of zirconium in it. Under this condition, estimation of ytterbium by other techniques (ICP-OES) was not possible. Thus, neutron activation analysis was selected, in which the powder sample can be directly used as such for irradiation, followed by subsequent measurement of induced radioactivity for the determination of the concentration of an element. Thus, neutron activation analysis was used to evaluate the homogeneous distribution of very low substituent concentration as mentioned in chapter-2. The Yb concentrations in all the three samples were calculated using the equation (2.3) described in chapter 2. The results obtained using instrumental neutron activation analysis (INAA) are shown in Table 3.1 with the average Yb concentration being less than 4 % of the amount initially added. These internal variations of the concentration of ytterbium in the compound was found to be within the statistical variation of the counting technique. Thus, the mixing methodology employed in the present investigations was found to be a satisfactorily effective homogeneous distribution of ytterbium. The typical decay scheme of ytterbium isotope, ^{175}Yb is shown in Figure 3.2.

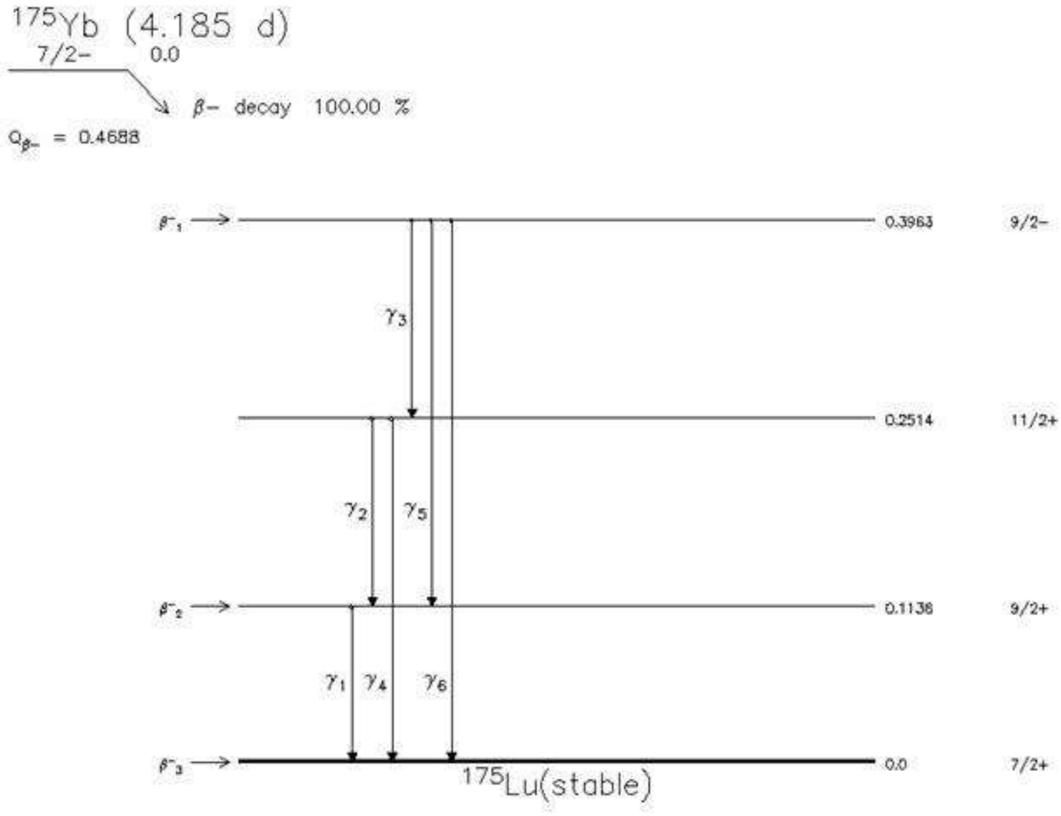

Figure 3. 2 Typical decay scheme of ^{175}Yb

Table 3. 1 Establishment of homogeneous mixing of ytterbium in calcium zirconate matrix by instrumental neutron activation analysis (INAA)

Sample	**Yb concentration (ppm)**
S1	757.5 ± 6.3
S2	753.7 ± 11.0
S3	758.3 ± 9.1

(S1, S2 and S3 are indicating the sample measurement in triplicate)

3.1.3.2 X- ray Diffraction

The powder diffraction patterns recorded for $CaZr_{1-x}Yb_xO_{3-\delta}$ (where x = 0 - 0.2) are shown in Figure 3.3. The observed lines were indexed and the phase identification of Yb substituted $CaZrO_3$ was confirmed by comparing their XRD patterns with JCPDS (space group Pnma, JCPDS card number 35–0790) file. Using linear least square fit algorithm, the structural parameters of pristine $CaZrO_3$ and Yb substituted compositions were calculated and summarized in Table 3.2. The lattice parameters reported are in good agreement with literature values [19, 20] confirming, a single phase of materials up to 10 % Yb substitution. Further introduction of ytterbium content, secondary phase attributed to Yb_2O_3 was also observed for the nominal composition $CaZr_{0.8}Yb_{0.2}O_{3-\delta}$. These observations indicate that up to 10 % ytterbium forms a solid solution in calcium zirconate matrix.

Table 3. 2 Calculated lattice parameter (a, b and c in Å) of $CaZr_{1-x}Yb_xO_{3-\delta}$ (where x = 0 - 0.1)

Compound	Lattice parameters (Å)		
	a	b	c
$CaZrO_3$	5.751 ± 0.001	8.032 ± 0.002	5.601± 0.001
$CaZr_{0.99}Yb_{0.01}O_{2.995}$	5.743 ± 0.002	7.970 ± 0.003	5.603± 0.002
$CaZr_{0.95}Yb_{0.05}O_{2.975}$	5.742 ± 0.001	8.012± 0.001	5.592± 0.001
$CaZr_{0.9}Yb_{0.1}O_{2.95}$	5.760± 0.002	8.024 ± 0.002	5.581± 0.003

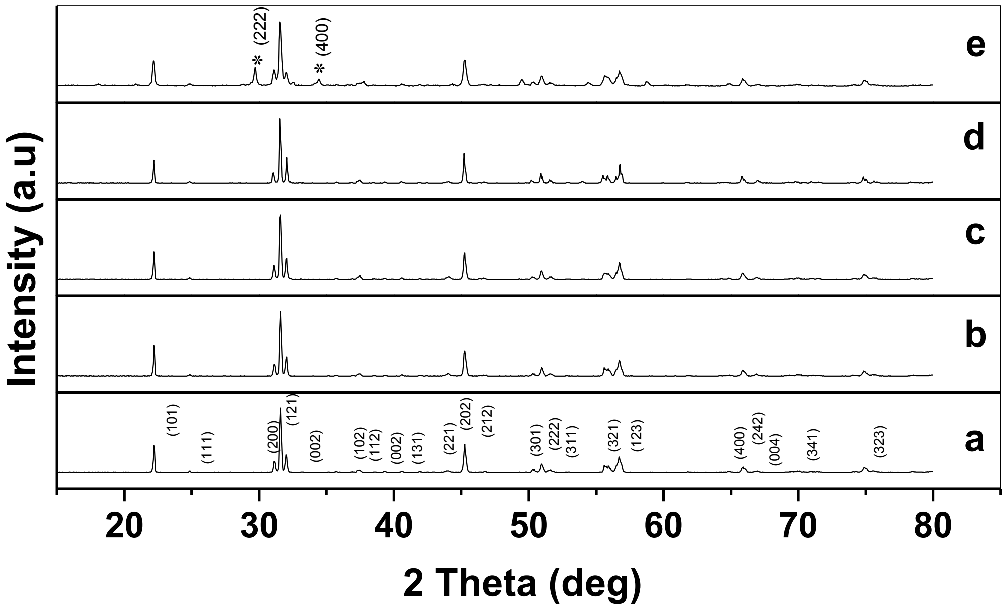

Figure 3. 3 XRD patterns of (a) $CaZrO_3$, nominal compositions (b) $CaZr_{0.99}Yb_{0.01}O_{3-\delta}$, (c) $CaZr_{0.95}Yb_{0.05}O_{3-\delta}$, (d) $CaZr_{0.9}Yb_{0.1}O_{3-\delta}$ and (e) $CaZr_{0.8}Yb_{0.2}O_{3-\delta}$ (* Indicates precipitation of Yb_2O_3)

3.1.3.3 Density measurements

Density of the sintered pellets obtained by both geometrical and pyconometry (liquid displacement) methods are shown in the Table 3.3. Closeness of the pycnometrically derived values with those from geometrical measurements indicated that the samples possess negligible or nil open porosities. Also, irrespective of the substitution level of ytterbium, the density remained nearly constant.

Table 3. 3 Comparison of density measurement results from geometrical and pycnometry for nominal compositions, $CaZr_{1-x}Yb_xO_{3-\delta}$ (x = 0 – 0.05)

Compound	**(%) of theoretical density**	
	Geometrical	**Archimedes**
$CaZrO_3$	93	94
$CaZr_{0.99}Yb_{0.01}O_{2.995}$	92	93
$CaZr_{0.95}Yb_{0.05}O_{2.975}$	92	93
$CaZr_{0.9}Yb_{0.1}O_{2.95}$	92	94

3.1.3.4 Morphological characterization

Figure 3.4 shows the scanning electron microscope images of the sintered $CaZr_{1-x}Yb_xO_{3-\delta}$ (x = 0, 0.01 & 0.05). The well-formed granules with pebble-like structure were observed. The granule size was found to be in the range of 1 to 5 μm range. The morphology was also found to be dense with well defined microstructure for all the three nominal compositions. The grain size was observed to be unaltered irrespective of the Yb concentration in $CaZrO_3$, indicates that the presence of ytterbium has no influence on the grain growth of $CaZrO_3$.

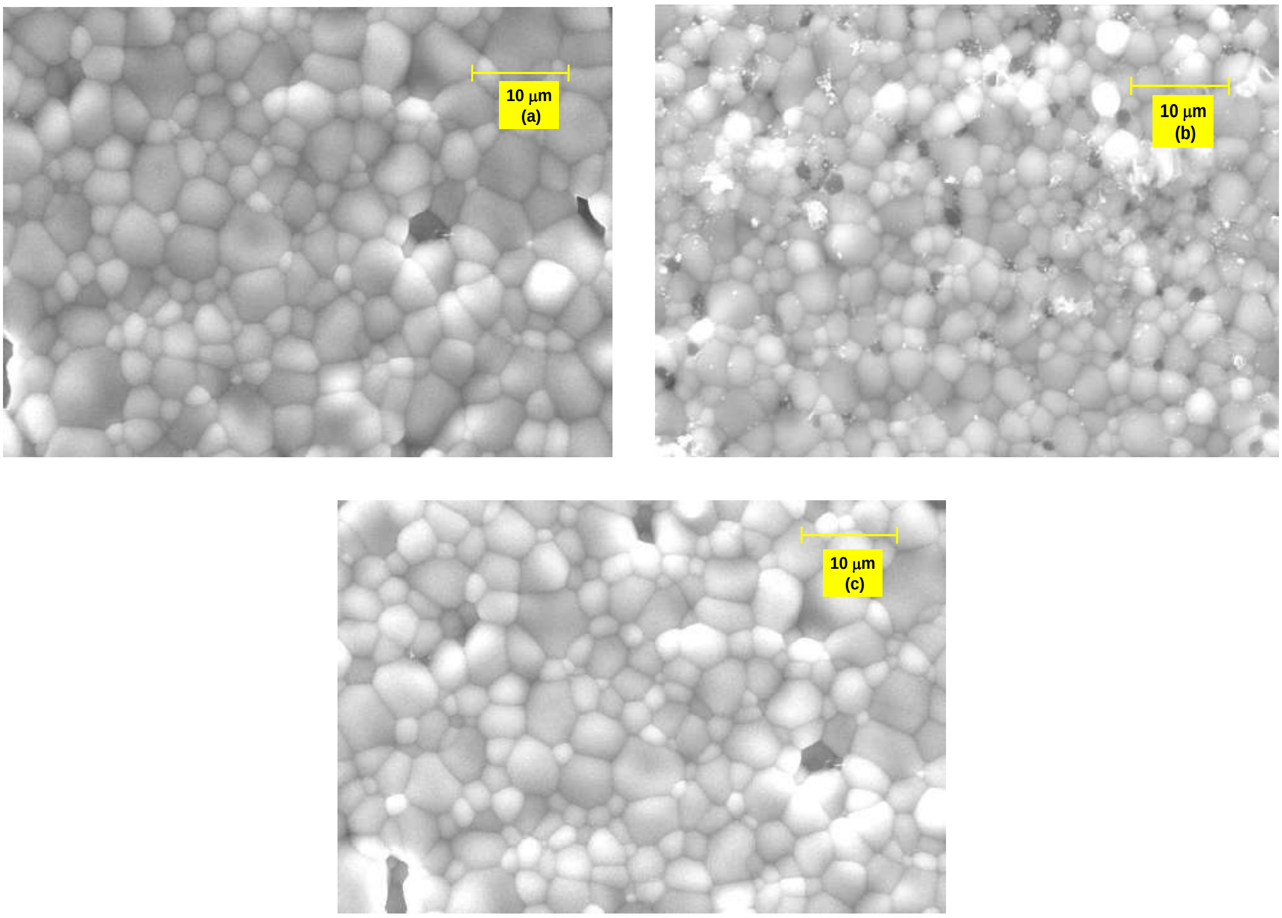

Figure 3. 4 Scanning electron microscope images of (a) $CaZrO_3$, (b) $CaZr_{0.99}Zr_{0.01}O_{2.995}$ and (c) $CaZr_{0.95}Zr_{0.05}O_{2.975}$

3.1.3.5 Electrical conductivity of $CaZr_{1-x}Yb_xO_{3-\delta}$ (x = 0 – 0.2)

(i) In Air

Typical Cole–Cole plot of $CaZr_{1-x}Yb_xO_{3-\delta}$ (x = 0, 0.01 & 0.05) recorded in air at 973 K is shown in Figure 3.5. The Nyquist plot drawn from the impedance data obtained for all the samples could only be fitted with single semicircle (Equivalent fit shown in the inset of Fig. 3.5) using Z® view (version 2.8) and the real axis intercept gives the resistance of the sample. No inter/intra grain boundary conductivities were able to resolve in the temperature range under study. The conductivity values were deduced from the dimensions of the pellet. The observed semicircular pattern is attributed to the inherent conduction processes involving the bulk or grain boundary conduction or a combination of both. As observed, the resistance of the compound increased with the introduction of ytterbium (Figures 3.5 (b) and 3.5 (c)). Further addition of ytterbium, i.e. $CaZr_{0.9}Yb_{0.1}O_{2.95}$, showed further increase in resistance (not shown in the figure). Similar observation of increase in resistance with ytterbium incorporation was also observed at all temperatures.

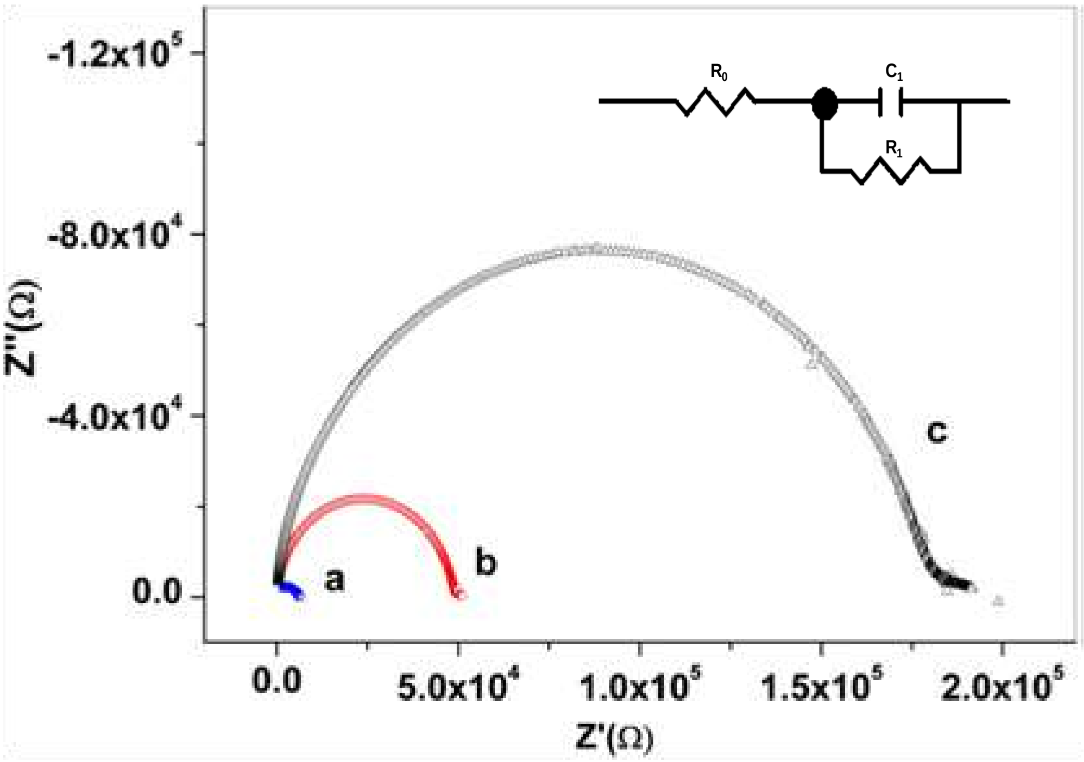

Figure 3. 5 Typical Cole–Cole plot measured in air at 973 K for (a) $CaZrO_3$, (b) $CaZr_{0.99}Yb_{0.01}O_{2.995}$ and (c) $CaZr_{0.95}Yb_{0.05}O_{2.975}$

Figure 3.6 shows the Arrhenius type plot of $CaZr_{1-x}Yb_xO_{3-\delta}$ (x = 0, 0.01, 0.05 & 0.1) in air. The activation energy deduced from this plot was around 0.95 eV, which suggests that the conducting species is oxide ion. It was also observed that the activation energy remained nearly same irrespective of the ytterbium concentration introduced, indicating that the conducting species and the mechanism remain unaltered. Up to $CaZr_{0.9}Yb_{0.1}O_{2.95}$, the reduction in conductivity is significant when compared to the parent, calcium zirconate. However, a small difference in the total conductivity was observed between the nominal compositions, $CaZr_{0.9}Yb_{0.1}O_{2.95}$ and $CaZr_{0.95}Yb_{0.05}O_{2.975}$ which is ascribed to the solid solution formation limit of ytterbium in calcium zirconate, as evidenced by X-ray diffraction results (section 3.3.2).

On introduction of ytterbium, the conductivity of calcium zirconate systematically decreased from 10^{-4} to 10^{-6} Scm^{-1} at 973 K. Similar trend of reduction in conductivity was observed at all temperatures. Calcium being a smaller ion (size 112 pm) probably tightly binds the oxygen ions bonded to it, which reduces the mobility of oxide ion, although more oxygen vacancies are created on systematic introduction of ytterbium. This reduction in the conductivity at extrinsic region, possibly due to the clustering of defects at low temperature and hence reduction in conductivity was observed. Further such compounds with different dopants were reported at high temperature (1000 K) [21].

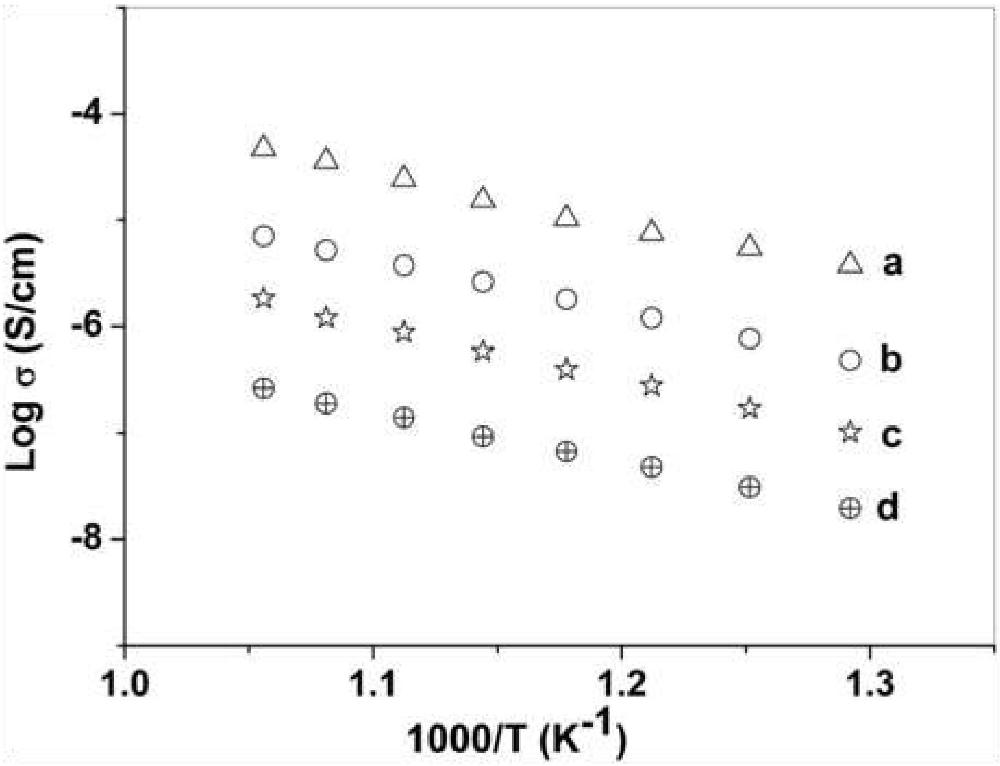

Figure 3. 6 Arrhenius plot for electrical conductivity of (a) $CaZrO_3$, (b) $CaZr_{0.99}Yb_{0.01}O_{2.995}$, (c) $CaZr_{0.95}Yb_{0.05}O_{2.975}$ and (d) $CaZr_{0.9}Yb_{0.1}O_{2.95}$ in air

(ii) Argon containing 80 ppm hydrogen

Figure 3.7 shows the typical Cole–Cole plot of $CaZr_{0.95}Yb_{0.05}O_{2.95}$ at three different temperatures, viz. 798, 973 and 973 K under 80 ppm H_2 atmosphere. As observed in air, in 80 ppm hydrogen in argon also the resistance decreased with increase in temperature. Figure 3.8 shows the typical Cole–Cole plot of $CaZr_{0.95}Yb_{0.05}O_{2.975}$ at 973 K in three different atmospheres such as air, O_2 and 80 ppm H_2 in Ar. As observed from the traces, the resistance remained nearly the same irrespective of the ambience.

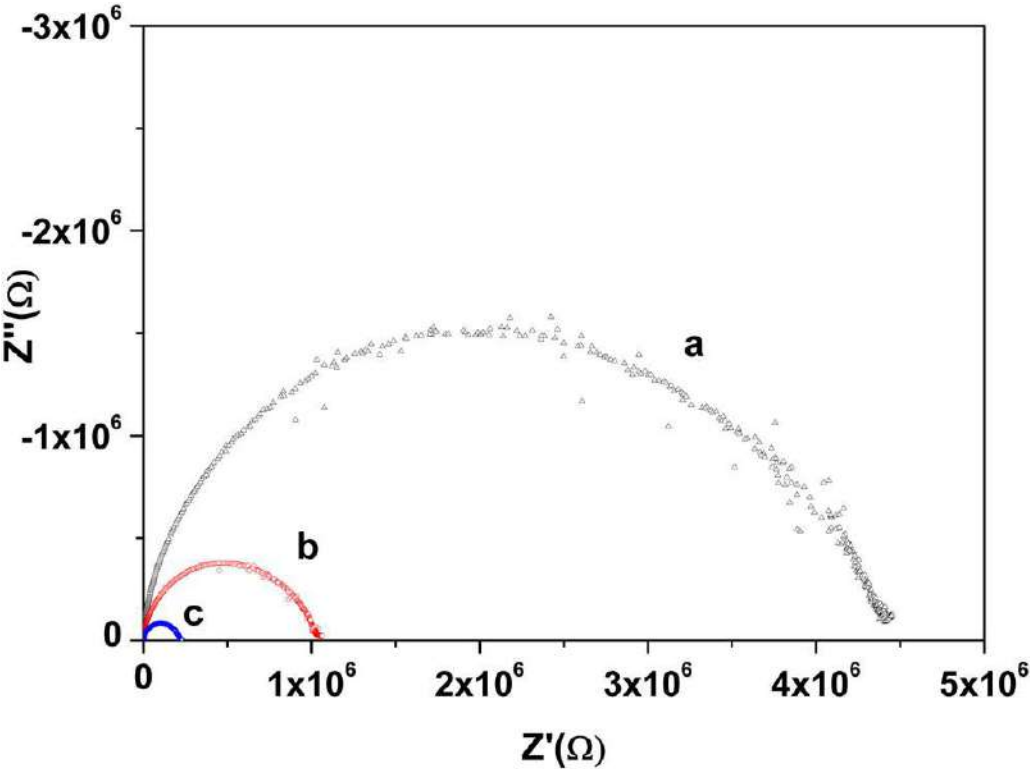

Figure 3. 7 Typical Cole-Cole plots of $CaZr_{0.95}Yb_{0.05}O_{2.975}$ recorded in 80 ppm H_2 in argon atmosphere :(a) 798, (b) 873 and (c) 973 K

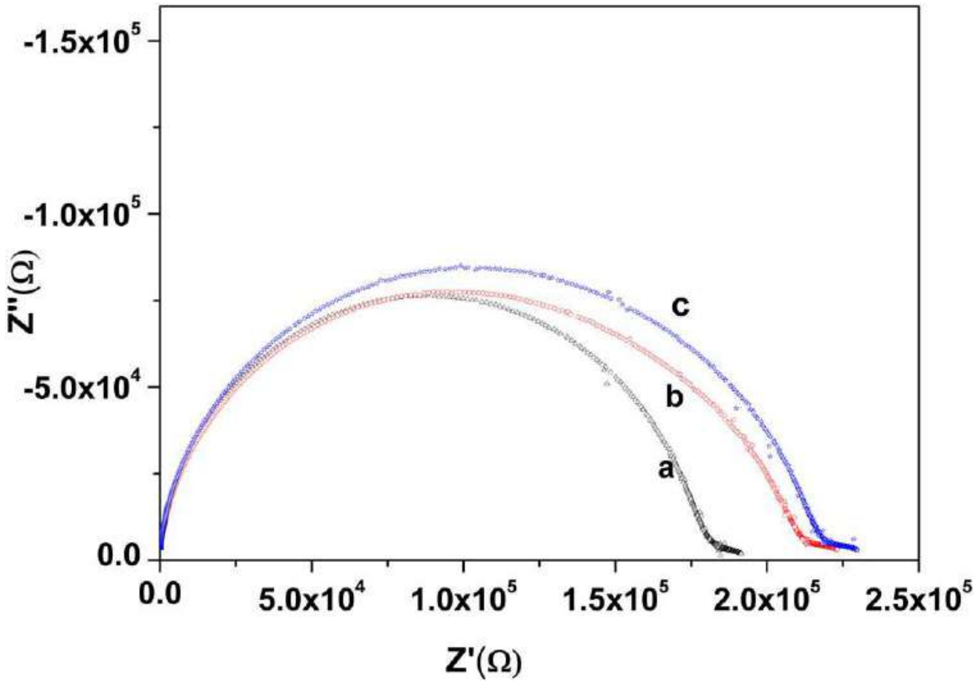

Figure 3. 8 Typical Cole-Cole plots of $CaZr_{0.95}Yb_{0.05}O_{2.975}$ recorded at 973 K in three difference ambiences (a) Air, (b) O_2 and (c) 80 ppm H_2 in argon

Figure 3.9 shows the typical Arrhenius-type plot for the nominal composition, $CaZr_{0.95}Yb_{0.05}O_{2.975}$ in three different atmospheres, viz. air, oxygen, and 80 ppm H_2 in argon. As evident from the plots, no significant difference both in the conductivity and also in activation energy was observed in these atmospheres. This also confirmed that the conducting species remain the same irrespective of the ambience. This corroborates with the observations made in the Arrhenius plots shown in Figure 3.9. Tables 3.4 and 3.5 showcase the consolidated account of the conductivity values and activation energies obtained for different nominal compositions under various atmospheres.

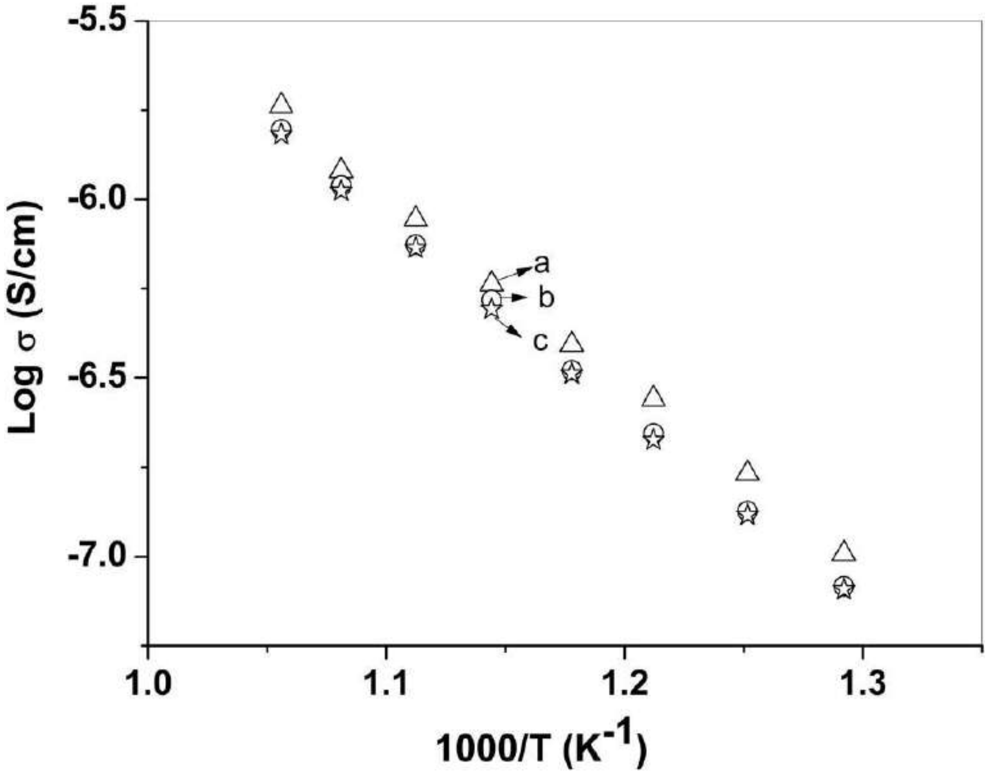

Figure 3. 9 Arrhenius plot for electrical conductivity of $CaZr_{0.95}Yb_{0.05}O_{2.975}$ in (a) Air, (b) O_2 and (c) 80 ppm H_2 in Ar

Table 3. 4 Conductivity of nominal compositions, $CaZr_{1-x}Yb_xO_{3-\delta}$ (x = 0 – 0.1) in different ambience

Compound	Conductivity (S cm^{-1}) [798–973] K		
	Air	O_2	80 ppm H_2 in Ar
$CaZrO_3$	(3.8 – 57.2) x 10^{-6}	(3.9 – 48.2) x 10^{-6}	(3.9 – 47.9) x 10^{-6}
$CaZr_{0.99}Yb_{0.01}O_{2.995}$	(0.48 – 7.01) x 10^{-6}	(0.45 – 7.10) x 10^{-6}	(0.44 – 6.83) x 10^{-6}
$CaZr_{0.95}Yb_{0.05}O_{2.975}$	(0.10 – 1.82) x 10^{-6}	(0.08 – 1.57) x 10^{-6}	(0.08 – 1.51) x 10^{-6}
$CaZr_{0.9}Yb_{0.1}O_{2.95}$	(0.02 – 0.26) x 10^{-6}	(0.02 – 0.26) x 10^{-6}	(0.02 – 0.26) x 10^{-6}

Table 3. 5 Activation energy for the conductivity process exhibited by the nominal compositions, $CaZr_{1-x}Yb_xO_{3-\delta}$ (x = 0 – 0.1)

Compound	Ea [eV]		
	Air	O_2	80 ppm H_2 in Ar
$CaZrO_3$	0.91 (±0.10)	0.90 (±0.09)	0.89 (±0.10)
$CaZr_{0.99}Yb_{0.01}O_{2.995}$	0.95 (±0.03)	0.97 (±0.03)	0.97 (±0.03)
$CaZr_{0.95}Yb_{0.05}O_{2.975}$	0.99 (±0.08)	1.03 (±0.04)	1.03 (±0.04)
$CaZr_{0.9}Yb_{0.1}O_{2.95}$	0.91 (±0.05)	1.01 ((±0.04)	1.01 (±0.09)

3.2 Studies on $SrZr_{1-x}Yb_xO_{3-\delta}$ (x= 0 – 0.2)

3.2.1 Structure

$SrZrO_3$ undergoes three phase transitions i.e. orthorhombic (Pnma), orthorhombic (Cmcm), tetragonal (l4mcm) and cubic (Pm3m) at 970, 1100 and 1440 K respectively. It has a melting temperature of about 2920 K and thereby it is cubic in a wide range of temperatures [22]. It is orthorhombic structure at room temperature, with space group Pnma-(62). The band gap of polycrystalline $SrZrO_3$ at room temperature was reported as 5.6 eV [23]. According to the crystallographic file (CIF) - 4387, $SrZrO_3$ structure is shown in Figure 3.10. The following section describes the solid solution formation range of ytterbium in $SrZrO_3$ and the effect of ytterbium on the physiochemical properties with the help of various experimental tools. Retention of hydrogen in the $SrZrO_3$ matrix was also elucidated.

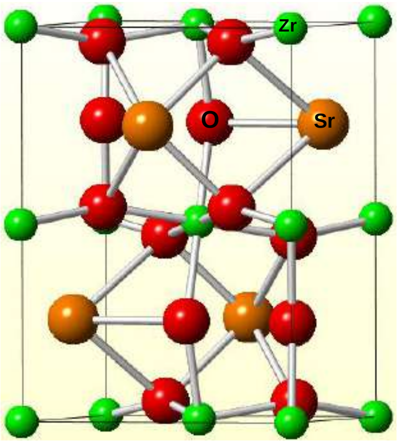

Figure 3. 10 Structure of Strontium zirconate

3.2.2 Experimental

Nominal compositions, $SrZr_{1-x}Yb_xO_{3-\delta}$ (x = 0 – 0.2) were synthesized via SSR using the precursor materials such as $SrCO_3$ (99.5%), ZrO_2 (99.0%) and Yb_2O_3

(99.5%). The calcination and sintering procedure were already discussed in the chapter-2. Physicochemical characterization techniques employed for the characterization of these compounds are presented in chapter 2.

3.2.3 Results and Discussion

3.2.3.1 X-ray characterization

X-ray diffraction patterns of $SrZr_{1-x}Yb_xO_{3-\delta}$ (where x = 0 - 0.2) are shown in Figure 3.11. The phase identification of $SrZrO_3$ was confirmed by comparing the XRD patterns with JCPDS (space group Pnma, JCPDS card number 44-0161) file. XRD pattern of 1 and 5 % were found to be identical with that of $SrZrO_3$ indicating the formation of solid solution. However, the other nominal compositions, $SrZr_{1-x}Yb_xO_{3-\delta}$ (where x = 0.1 & 0.2) showed the precipitation of Yb_2O_3 phase. The unit cell volume of strontium zirconate is 276.69 Å^3 (calculated from unit cell parameters, a = 5.8179 Å; b = 8.204 Å; c = 5.797 Å–JCPDS 44–0161), which is about 7.3% more than the unit cell volume of calcium zirconate is 257.85 Å^3. Thus, it is logical to expect a higher limit of solid solution formation in strontium zirconate owing to its larger lattice volume. However, the solid solution formation limit of ytterbium in strontium zirconate is significantly lower than that in calcium zirconate. Further, though the size of Yb^{3+} (86.8 pm) is higher than host ion Zr^{4+} (72 pm) on introduction of Yb^{3+} in Zr^{4+} site, significant change in 2 theta is not observed up to the solid solution formation limit (1 - 5% Yb_2O_3 substitution) in comparison with pristine $SrZrO_3$.

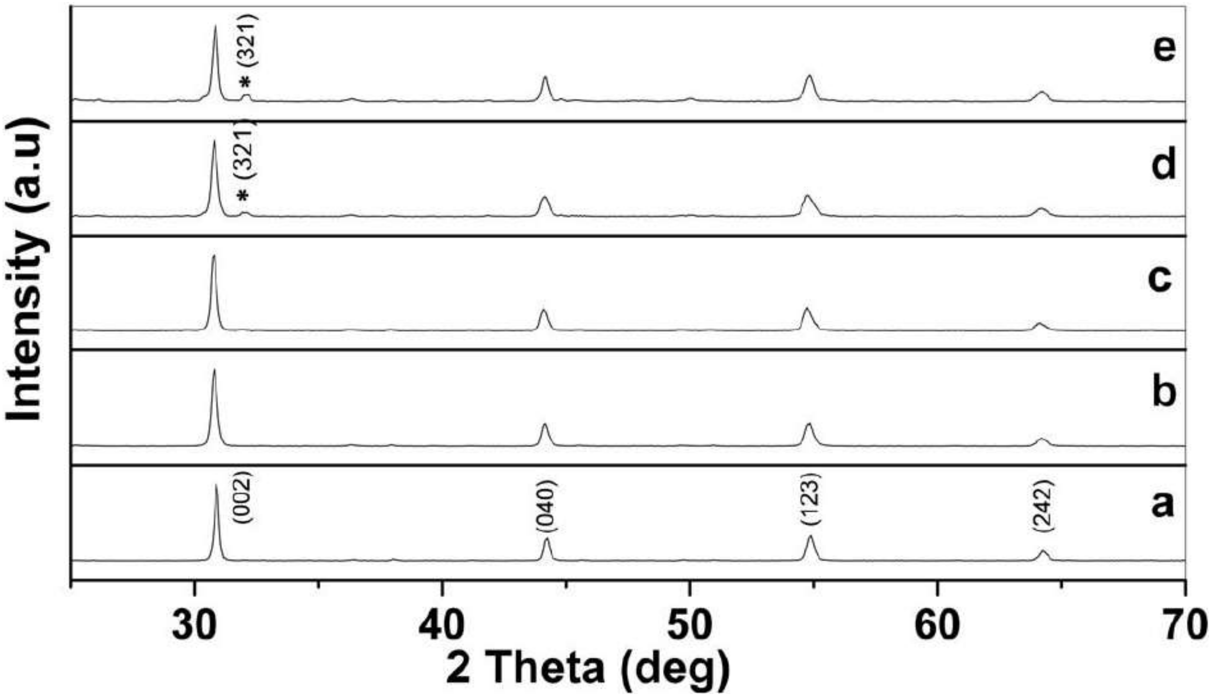

Figure 3. 11 XRD pattern of (a) $SrZrO_3$, nominal compositions (b) $SrZr_{0.99}Yb_{0.01}O_{3-\delta}$, (c) $SrZr_{0.95}Yb_{0.05}O_{3-\delta}$, (d) $SrZr_{0.9}Yb_{0.1}O_{3-\delta}$ and (e) $SrZr_{0.8}Yb_{0.2}O_{3-\delta}$ (* Indicates precipitation of Yb_2O_3)

3.2.3.2 Density measurements

The density of the sintered pellets obtained by both geometrical and pyconometry (liquid displacement) method are shown in the Table 3.6. The values are about 93% of the theoretical densities of these ceramics. The values derived between both the methods were found to be nearly same, owing to the negligible or nil open porosity of the sintered samples. Irrespective of the concentration of Yb, the densities of the sample remained nearly same. Identical observation was made with $CaZrO_3$ also (section 3.1.3.3).

Table 3. 6 Comparison of density measurement results from geometrical and pycnometry for nominal compositions, $SrZr_{1-x}Yb_xO_{3-\delta}$ (x = 0 – 0.05)

Compound	% of theoretical density	
	Geometrical	Archimedes method
$SrZrO_3$	94	95
$SrZr_{0.99}Yb_{0.01}O_{2.995}$	94	93
$SrZr_{0.95}Yb_{0.05}O_{2.975}$	93	93

3.2.3.3 Morphological characterization

Pristine $SrZrO_3$ (Figure 3.12 (a)) showed very well formed dense grains with the sizes varying between 1 and 5 μm. On introduction of ytterbium, ($SrZr_{0.99}Yb_{0.01}O_{2.995}$), it shows a significant reduction in average grain size to 500 nm (Fig. 3.12 (b)) and further reduction in grain size for higher ytterbium concentration is not observed (Fig. 3.12 (c)). This observation of saturation in the reduction of grain growth coincided with the solid solution formation limit observed in X-ray diffraction studies (section 3.2.3.1).

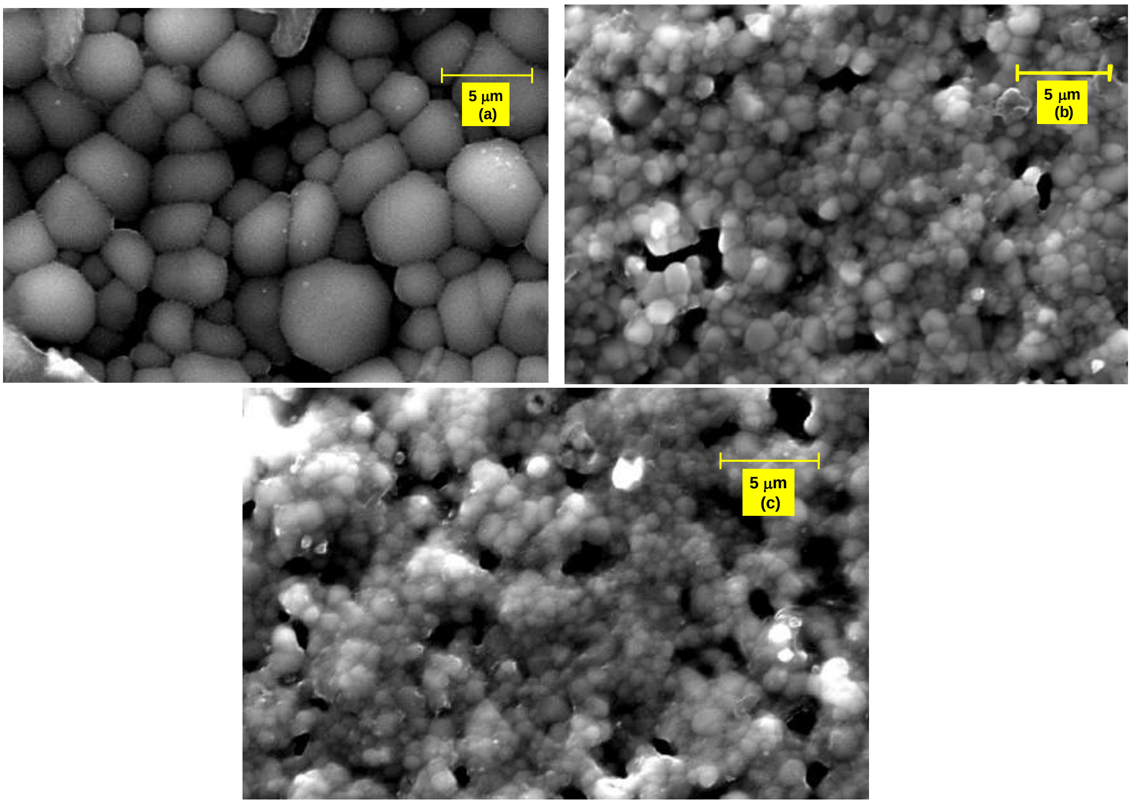

Figure 3. 12 Microstructures of the samples sintered at 1873 K. (a) $SrZrO_3$, (b) $SrZr_{0.99}Yb_{0.01}O_{2.995}$, and (c) $SrZr_{0.95}Yb_{0.05}O_{2.975}$

3.2.3.4 Electrical conductivity

(i) In Air

Typical Cole–Cole plot of $SrZr_{1-x}Yb_xO_{3-\delta}$ (x = 0, 0.01 & 0.05) recorded in air at 973 K is shown in Figure 3.13. As observed, on introduction of ytterbium the resistance of the compound decreased (Figures 3.13 b and 3.13 c). Further addition of ytterbium, i.e., $SrZr_{0.9}Yb_{0.1}O_{2.95}$, showed further decrease in resistance (not shown in the figure). Similar observation of decrease in resistance with ytterbium incorporation was also observed at all temperatures.

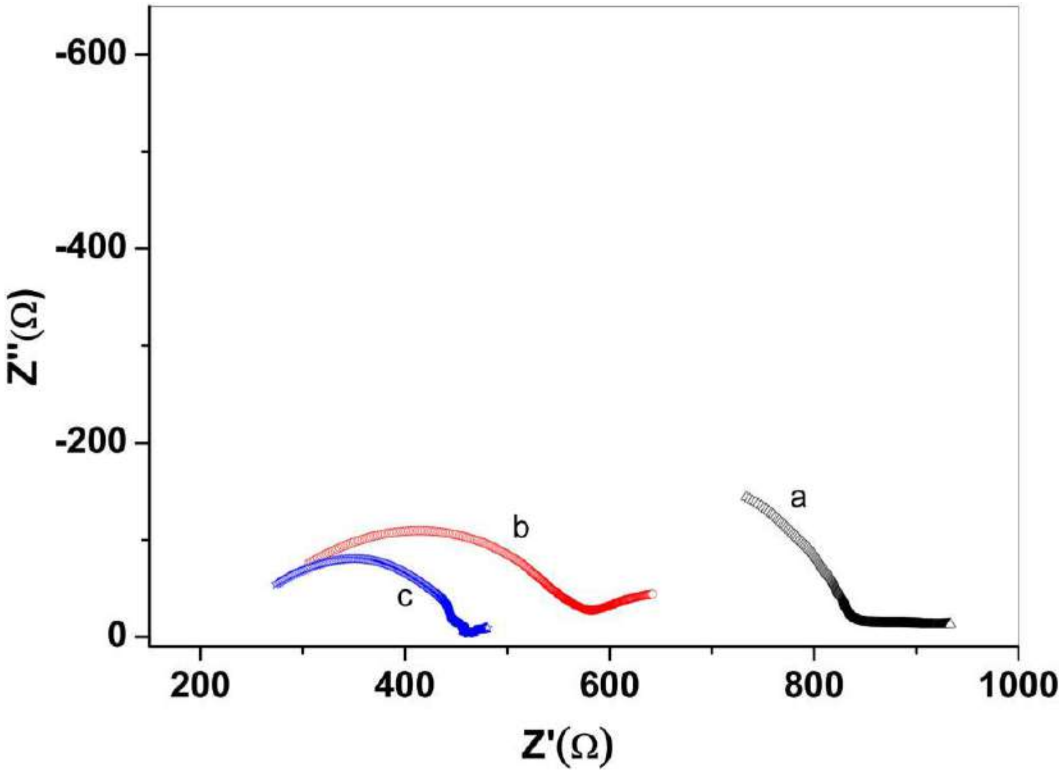

Figure 3. 13 Typical Cole-Cole plots measured in air at 973 K for (a) $SrZrO_3$, (b) $SrZr_{0.99}Yb_{0.01}O_{2.995}$ and (c) $SrZr_{0.95}Yb_{0.05}O_{2.975}$

Figure 3.14 shows the Arrhenius plot of $SrZr_{1-x}Yb_xO_{3-\delta}$ (x = 0 - 0.1) in air. The activation energy was deduced from this plot and a small reduction in the activation energy was observed after introduction of ytterbium. This suggests that the conducting species is oxide ion. However, the reason for the decrease in activation energy with ytterbium substitution was not understood. The increase in conductivity was observed to be significant for the composition up to the $SrZr_{0.95}Yb_{0.05}O_{2.975}$ in comparison with parent strontium zirconate. However, there was no significant change in conductivity between 1 and 5 % Yb_2O_3 substituted $SrZrO_3$, This is ascribed to the solid solution formation limit of ytterbium in strontium zirconate, which lies between 0.01 and 0.05 and precipitation of ytterbia (Yb_2O_3), as evidenced by X-ray diffraction results (section 3.2.3.1). Table 3.8 gives the activation energy values derived for the nominal compositions in the temperature range of 798 to 973 K. As discussed in X-ray characterization section, the unit cell volume of strontium zirconate is about 7.3 % more than that of calcium zirconate. On introduction of ytterbium in strontium zirconate, oxide ion vacancy will be created up to the solid solution formation limit [change in volume of the matrix due to the introduction of ytterbium is considered negligible]. Strontium ion being bigger in size (126 pm), is expected to bind the oxygen ion surrounding it less tightly compared to calcium. Also, due to the enhanced volume of strontium zirconate, facile oxide ion movement is envisaged in strontium zirconate matrix when compared to calcium zirconate. These factors possibly contribute to the improved conductivity by ytterbium substituted strontium zirconate.

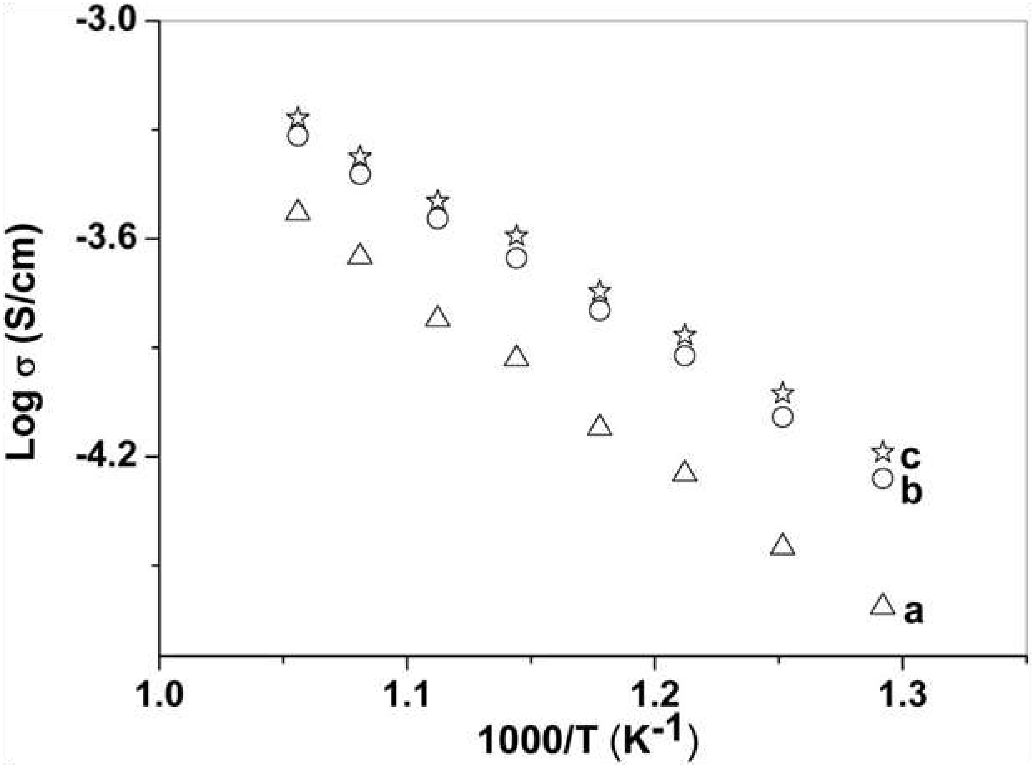

Figure 3. 14 Arrhenius plot for electrical conductivity of (a) $SrZrO_3$, (b) $SrZr_{0.99}Yb_{0.01}O_{2.995}$ and (c) $SrZr_{0.95}Yb_{0.05}O_{2.975}$ in air

The conductivity of $SrZr_{0.95}Yb_{0.05}O_{2.975}$ in air, O_2, 80 ppm and 4% H_2 in argon is plotted in Figure 3.15 as a function of temperature. The conductivity values are found to be in the same order for the all the ambience, although oxygen and hydrogen concentrations were increased from 20 to 100 % (in case of air to oxygen) and from 80 to 40000 ppm (4%) (in case of hydrogen in argon) respectively.

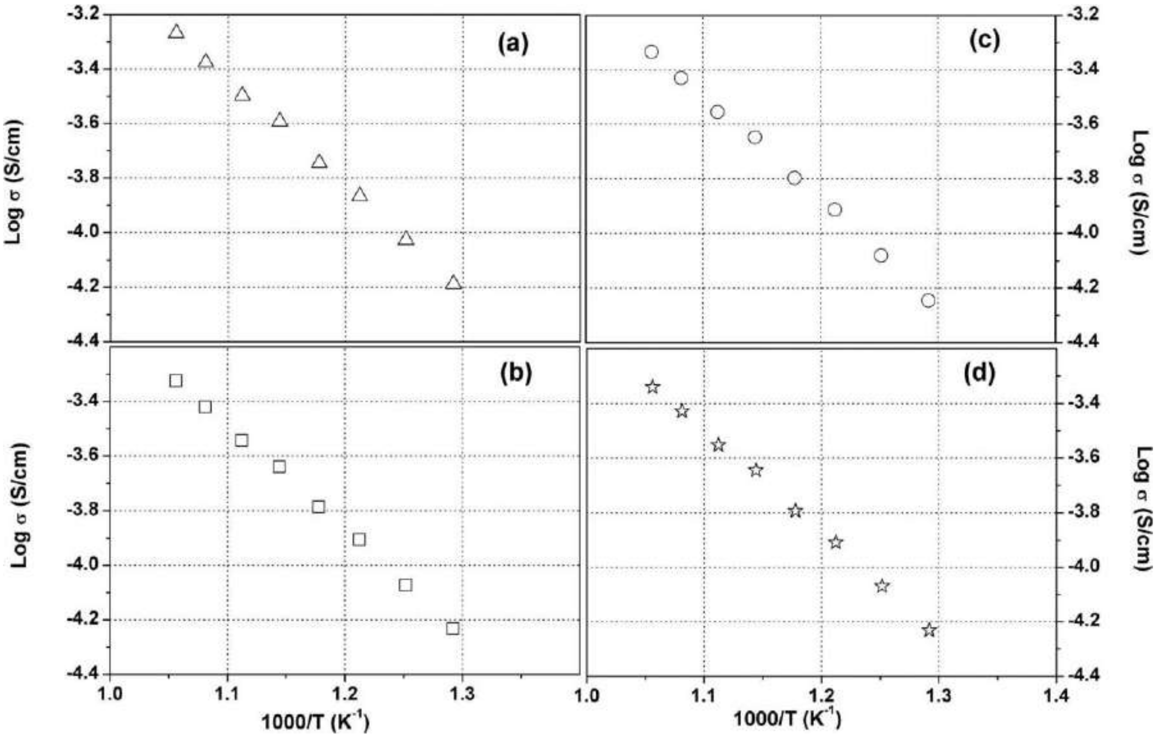

Figure 3. 15 Arrhenius plots for electrical conductivity $SrZr_{0.95}Yb_{0.05}O_{2.975}$ (a) Air, (b) O_2, (c) 80 ppm H_2 in Argon and (d) 4% H_2 in Argon

Figure 3.16 & 3.17 shows the conductivity of pure Yb_2O_3 and $SrZr_{1-x}Yb_xO_{3-\delta}$ (x = 0, 0.01, 0.05) as function of temperature in 80 ppm hydrogen in argon respectively. The conductivity of pure Yb_2O_3 in air was found to be in the range from ($9x10^{-10}$- $41x10^{-10}$) Scm^{-1} in the temperature range from (573 – 873) K. No significant variation in the conductivity for different ambience such as O_2 and 80 ppm hydrogen in argon. The comparison of our results (shown in Table 3.8) with $SrZr_{0.85}Yb_{0.15}O_{2.925}$, reported by Yajima et al. [11] show one order less in the temperature range from 873 – 973 K. However, for pristine $SrZrO_3$, our data show 1 order higher than the literature value [11]. It is further pointed out that our studies were carried out in 80 ppm and 40000 ppm (4%) hydrogen in argon, while the literature report was under 100% hydrogen atmosphere. However, the precise reasons for the different conductivity values of pristine and ytterbium substituted strontium zirconate phases when compared to the literature values still remain unexplained.

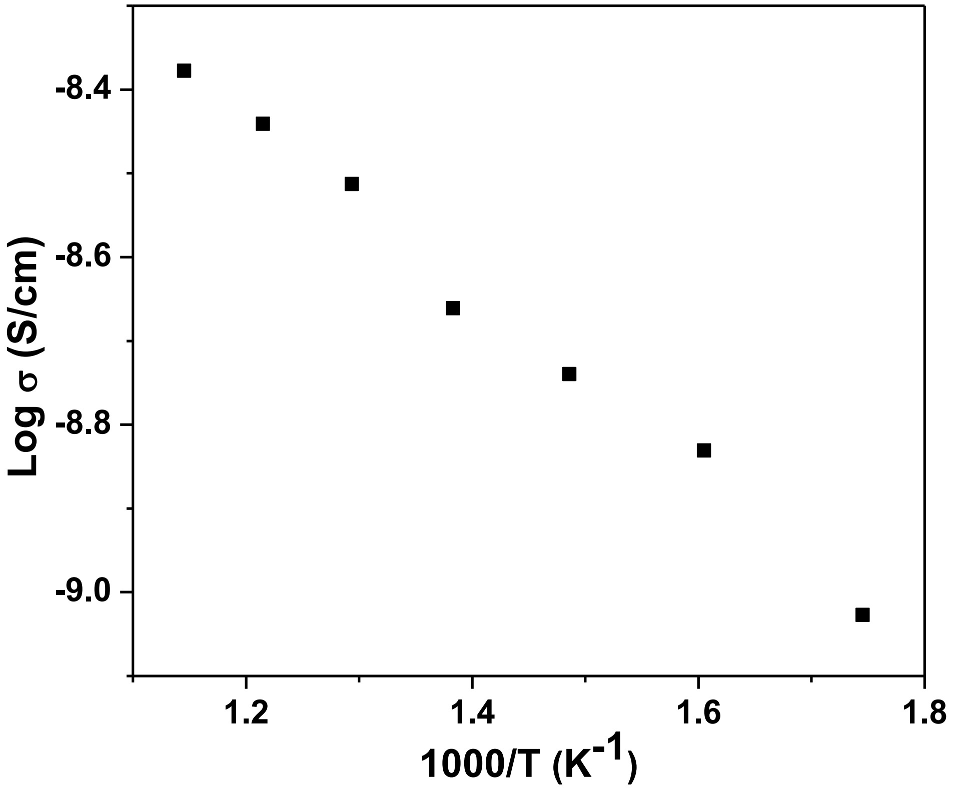

Figure 3. 16 Arrhenius plot for electrical conductivity of Yb_2O_3 in air

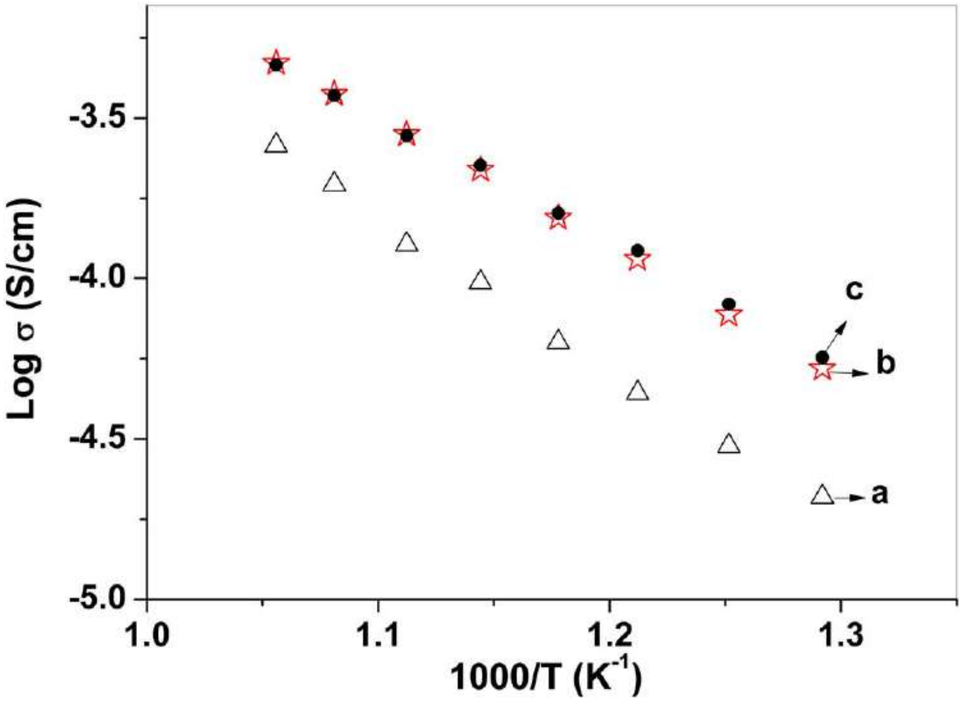

Figure 3. 17 Arrhenius plot for electrical conductivity of (a) $SrZrO_3$, (b) $SrZr_{0.99}Yb_{0.01}O_{2.995}$ and (c) $SrZr_{0.95}Yb_{0.05}O_{2.975}$ in 80 ppm H_2 in Argon

(ii) In argon containing 80 ppm hydrogen

Figure 3.17 shows the typical Cole-Cole plot of $SrZr_{0.95}Yb_{0.05}O_{2.975}$ at three different temperatures, viz. 798, 873 and 973 K under 80 ppm H_2 atmosphere. As observed, the conductivity increased with temperature. Tables 3.7 and 3.8 showcase the consolidated account of the conductivity values and activation energy obtained for different nominal compositions under various atmospheres. Pristine strontium zirconate exhibited similar conductivity like its lower analogue, namely, calcium zirconate. However, on introduction of ytterbium, the nominal composition, $SrZr_{0.99}Yb_{0.01}O_{2.995}$, exhibited twice the conductivity of the pristine strontium zirconate at all temperatures. Any further addition of ytterbium, for example, the nominal composition, $SrZr_{0.95}Yb_{0.05}O_{2.975}$ showed only marginal improvement in conductivity. The probable mechanism for the conduction, while exposing the sample to air and oxygen is given in equation 3.4.

$$\frac{1}{2}O_2 + V_{\ddot{O}} \rightarrow O_{O}^{X} + h^{\cdot\cdot} \qquad (3.4)$$

As shown in the equation (3.4), in air /oxygen hole concentration increases, leading to increase in conductivity.

Similarly hydrogen incorporation would lead to increase the proton conduction, as per the equation 3.2 and 3.3 shown in section 3.1.1, when sample was exposed to hydrogen atmosphere.

All the composition shows similar activation energy (Table 3.8) in different ambience, which possibly indicates that the conduction mechanism remains same irrespective of the ambience.

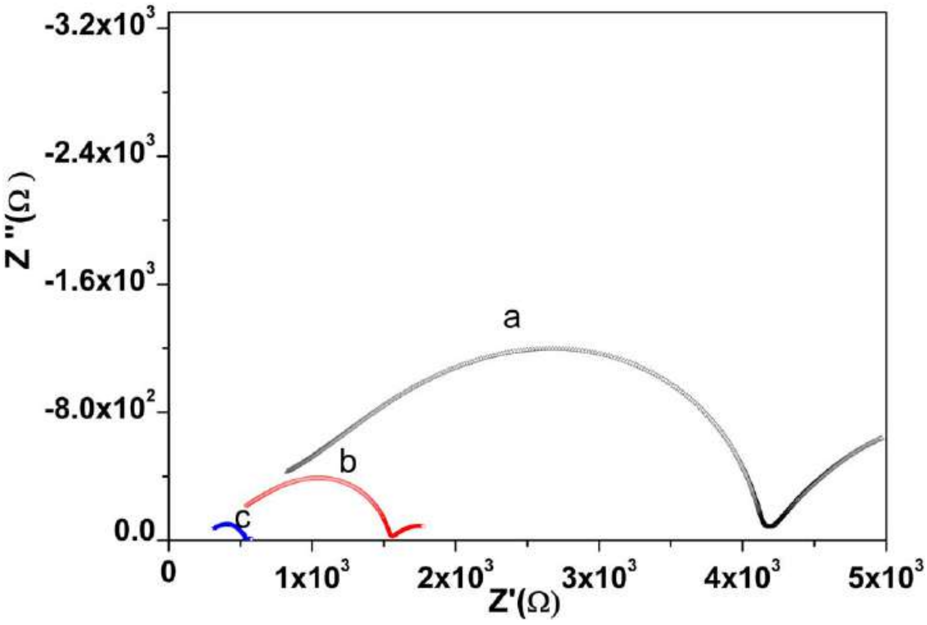

Figure 3. 18 Typical Cole–Cole plots of $SrZr_{0.95}Yb_{0.05}O_{2.975}$ in 80 ppm H_2 in argon (a) 798 (b) 873 and (c) 973 K

Table 3. 7 Conductivity of nominal compositions, $SrZr_{1-x}Yb_xO_{3-\delta}$ (x = 0 – 0.05) in different ambience

Compound	**Conductivity (Scm^{-1}) [798 - 973] K**		
	Air	O_2	80ppm H_2 in Ar
$SrZrO_3$	(0.24 -2.95) x10^{-4}	(0.27 -2.79) x10^{-4}	(0.21 -2.59) x10^{-4}
$SrZr_{0.99}Yb_{0.01}O_{2.995}$	(0.55 -4.81) x10^{-4}	(0.53 -4.68) x10^{-4}	(0.53 -4.69) x10^{-4}
$SrZr_{0.95}Yb_{0.05}O_{2.975}$	(0.62 -5.14) x10^{-4}	(0.56 -4.50) x10^{-4}	(0.54 -4.41) x10^{-4}

Table 3. 8 Activation energy for the conductivity process exhibited by the nominal compositions, $SrZr_{1-x}Yb_xO_{3-\delta}$ (x = 0 – 0.05)

Compound	**Ea [eV]**		
	Air	O_2	80 ppm H_2 in Ar
$SrZrO_3$	0.89 (±0.10)	0.90 (±0.10)	0.91 (±0.10)
$SrZr_{0.99}Yb_{0.01}O_{2.995}$	0.76 (±0.04)	0.77 (±0.04)	0.77 (±0.04)
$SrZr_{0.95}Yb_{0.05}O_{2.975}$	0.75 (±0.05)	0.74 (±0.05)	0.74 (±0.05)

3.2.3.5 Elucidation of hydrogen retention in $SrZr_{0.95}Yb_{0.05}O_{2.975}$ matrix

To evaluate the retention of hydrogen in zirconate matrix, the electrical conductivity studies were carried out using 5 mole of ytterbium substituted strontium zirconate. Initially, the nominal composition of $SrZr_{0.95}Yb_{0.05}O_{2.975}$ was equilibrated with oxygen for 6 h at 873 K and conductivity measurements were carried out in the temperature range from 573 to 873 K. The same sample was further, equilibrated with hydrogen and electrical conductivity was measured in the same temperature range. To understand the regeneration or retrace nature of conductivity, the samples exposed with hydrogen were equilibrated in oxygen atmosphere. Conductivities for the same range of temperature of study were recorded at different time intervals i.e. 24,48 and 96 h. Figure 3.18 shows the typical conductivity behavior of $SrZr_{0.95}Yb_{0.05}O_{2.975}$ (a) in O_2, (b) in H_2 and (c) to (e) during recovery in oxygen atmosphere after 24 h, 48 h and 96 h exposure to hydrogen respectively. Figure 3.18 (c (□)) shows conductivity measurement of the sample equilibrated for 24 h in oxygen atmosphere (after exposure to H_2). The conductivity values remained close to that of hydrogen equilibrated sample (Fig 3.18 (b (○)). The conductivity measured after equilibration for 48 h was indicated by (d (☆)). The measured values slightly different from that of (c (□)). The equilibrium studies were continued further and conductivity measurement were performed after 96 h (e (⊕)). These values were close to that of the sample equilibrated initially with oxygen. This indicates the acceptable retrace of the conductivity back to its original values. This behavior suggests the incorporation of hydrogen into the matrix during the equilibration with hydrogen atmosphere which was removed again on its equilibration with O_2 equilibration at high temperature for long duration.

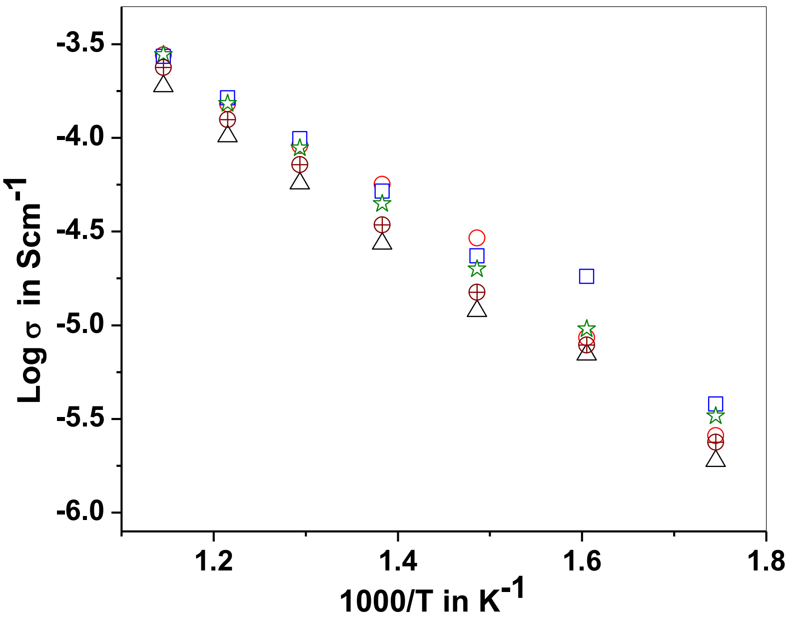

Figure 3. 19 Electrical of conductivity behavior of $SrZr_{0.95}Yb_{0.05}O_{2.975}$ in presence of (a) (△) O_2, [b] (○) H_2 and during recovery in O_2 ambience after [c] (□) 24h, [d] (☆) 48 h and [e] () 96 h

3.3 Conclusions

The present investigations established the following observations i.e. the solid solution formation range of ytterbium in calcium zirconate is up to 10% substitution of zirconium (i.e. $CaZr_{0.9}Yb_{0.1}O_{2.95}$), while in the case of strontium zirconate, it lies between 1 and 5% ($SrZr_{0.99}Yb_{0.01}O_{2.995}$-$SrZr_{0.95}Yb_{0.05}O_{2.975}$). Introduction of ytterbium did not influence the grain growth of calcium zirconate. On the other hand, it inhibited the grain growth up to the solid solution formation limit in strontium zirconate ($SrZr_{0.99}Yb_{0.01}O_{2.995}$). The present studies, highlighted the impact of ytterbium on the conductivity of calcium zirconate for the first time. The conductivity was reduced by two orders up to the solid solution formation limit ($CaZr_{0.9}Yb_{0.1}O_{2.95}$) in the entire temperature range of the studies (798 – 973 K). The conductivity was also not influenced by the ambience in which the studies were performed. On the other hand, introduction of ytterbium in strontium zirconate, the conductivity was increased, which saturates with the limit of solid solution formation ($SrZr_{0.95}Yb_{0.05}O_{2.975}$). However, as in the case of calcium analogues, ytterbium substituted strontium zirconates also showed no influence of the ambience on their conductivity. The incorporation of hydrogen in ytterbium substituted strontium zirconates was elucidated in the conductivity studies. The results were also found in agrrement with the reported conductivity values. In nutshell, the present results elucidated the contrasting roles played by ytterbium in the solid solution formation range, grain growth and electrical conductivity of calcium and strontium zirconate matrices.

3.4 References

[1] H. Iwahara, H. Uchida, S. Tanaka, High temperature type proton conductor based on $SrCeO_3$ and its application to solid electrolyte fuel cells, Solid State Ionics, 9-10 (1983) 1021-1025.

[2] T. Yajima, H. Kazeoka, T. Yogo, H. Iwahara, Proton conduction in sintered oxides based on $CaZrO_3$, Solid State Ionics, 47 (1991) 271-275.

[3] H. Iwahara, T. Yajima, T. Hibino, K. Ozaki, H. Suzuki, Protonic conduction in calcium, strontium and barium zirconates, Solid State Ionics, 61 (1993) 65-69.

[4] H. Iwahara, T. Esaka, H. Uchida, T. Yamauchi, K. Ogaki, High temperature type protonic conductor based on $SrCeO_3$ and its application to the extraction of hydrogen gas, Solid State Ionics, 18-19 (1986) 1003-1007.

[5] H. Iwahara, Hydrogen pumps using proton-conducting ceramics and their applications, Solid State Ionics, 125 (1999) 271-278.

[6] H. Iwahara, T. Hibino, T. Sunano, An electrochemical steam pump using a proton conducting ceramic, Journal of Applied Electrochemistry, 26 (1996) 829-832.

[7] T. Yajima, K. Koide, N. Fukatsu, T. Ohashi, H. Iwahara, A new hydrogen sensor for molten aluminum, Sensors and Actuators B: Chemical, 14 (1993) 697-699.

[8] G.C. Mather, F.M. Figueiredo, J.R. Jurado, J.R. Frade, Synthesis and characterisation of cermet anodes for SOFCs with a proton-conducting ceramic phase, Solid State Ionics, 162-163 (2003) 115-120.

[9] M. Zhou, A. Ahmad, Sol–gel processing of In-doped $CaZrO_3$ solid electrolyte and the impedimetric sensing characteristics of humidity and hydrogen, Sensors and Actuators B: Chemical, 129 (2008) 285-291.

[10] K.W. Browall, O. Muller, R.H. Doremus, Oxygen ion conductivity in oxygen-deficient perovskite-related oxides, Materials Research Bulletin, 11 (1976) 1475-1481.

[11] T. Yajima, H. Suzuki, T. Yogo, H. Iwahara, Protonic conduction in $SrZrO_3$-based oxides, Solid State Ionics, 51 (1992) 101-107.

[12] H. Wang, X. Wang, B. Meng, X. Tan, K.S. Loh, J. Sunarso, S. Liu, Perovskite-based mixed protonic–electronic conducting membranes for hydrogen separation: Recent status and advances, Journal of Industrial and Engineering Chemistry, 60 (2018) 297-306.

[13] P. Stoch, J. Szczerba, J. Lis, D. Madej, Z. Pędzich, Crystal structure and ab initio calculations of $CaZrO_3$, Journal of the European Ceramic Society, 32 (2012) 665-670.

[14] Santosh K. Gupta, P. S. Ghosh, N.P. and, R. Tewarib, Nature of defects in blue light emitting $CaZrO_3$: spectroscopic and theoretical study, RSC Adv, 5 (2015).

[15] J. Lyagaeva, N. Danilov, D. Korona, A. Farlenkov, D. Medvedev, A. Demin, I. Animitsa, P. Tsiakaras, Improved ceramic and electrical properties of $CaZrO_3$-based proton-conducting materials prepared by a new convenient combustion synthesis method, Ceramics International, 43 (2017) 7184-7192.

[16] S.C. Hwang, G.M. Choi, The mixed ionic and electronic conductivity of $CaZrO_3$ with cation nonstoichiometry and oxygen partial pressure, Solid State Ionics, 179 (2008) 1042-1045.

[17] R.J.D. Tilley, Defects in Solids, A John Wiley & Sons , INC., Publication2008.

[18] Z. Tao, L. Yan, J. Qiao, B. Wang, L. Zhang, J. Zhang, A review of advanced proton-conducting materials for hydrogen separation, Progress in Materials Science, 74 (2015) 1-50.

[19] M.V. Anan’ev, N.M. Bershitskaya, S.V. Plaksin, E.K. Kurumchin, Phase equilibriums, oxygen exchange kinetics and diffusion in oxides $CaZr_{1-x}Sc_xO_{3-x/2-\delta}$, Russian Journal of Electrochemistry, 48 (2012) 879-886.

[20] Z.F. Hou, Ab initio calculations of elastic modulus and electronic structures of cubic $CaZrO_3$, Physica B: Condensed Matter, 403 (2008) 2624-2628.

[21] J. Bao, Y. Okuyama, Z. Shi, N.F.a.N. Kurita, Properties of Electrical Conductivity in Y-Doped $CaZrO_3$, Materials Transactions, 53 (2012).

[22] R.I. Eglitis, Ab Initio Calculations of the Atomic and Electronic Structure of $SrZrO_3$ (111) Surfaces, Ferroelectrics, 436 (2012) 5-11.

[23] Y.S. Lee, J.S. Lee, T.W. Noh, D.Y. Byun, K.S. Yoo, K. Yamaura, E. Takayama-Muromachi, Systematic trends in the electronic structure parameters of the 4d transition-metal oxides $SrMO_3$ (M=Zr, Mo, Ru, and Rh), Physical Review B, 67 (2003) 113101.

CHAPTER 4

Chapter 4: Preparation & physio-chemical characterization of $BaTh_{1-x}Yb_xO_{3-\delta}$ (x = 0 – 0.2)

4.1. Introduction

The perovskite structured ($A^{II}B^{IV}O_3$) cerates [1-3] and zirconates [4-6] exhibit appreciable oxide and proton conduction at high temperatures under suitable ambiences. Ishihara reported among II–IV perovskites, $BaZrO_3$, $BaCeO_3$, $BaTbO_3$ and $BaThO_3$ as the best proton conductors, owing to their large negative hydration enthalpies and small activation energies for proton migration [7]. The highest total proton conductivity among the system is arranged in the ascending order as follows, $CaZr_{0.9}In_{0.1}O_{3-\delta} < SrZr_{0.95}Y_{0.05}O_{3-\delta} < SrCe_{0.95}Yb_{0.05}O_{3-\delta} < BaCe_{0.95}Y_{0.05}O_{3-\delta}$, the trend of which can be rationalized based on the temperature programmed desorption (TPD) experiment, their proton concentrations and proton mobility [8]. This may be explained mainly by considering the following aspects: (1) the larger ionic radii of ions occupy A and B positions of ABO_3 perovskites, (2) relatively low electronegativity and (3) low grain-boundary resistance. In addition, the trivalent dopant ion is also playing a key role, which is mainly governed by ionic size.

The total conductivities of ytterbium substituted Ca and Sr zirconates in different ambience in the temperature range of 798 to 973 K were discussed in the chapter 3. In order to have higher electrical conductivity than $SrZrO_3$ at moderate temperatures, the approach for selection of perovskites is evolved based on the crystallographic- related parameters. Cerate and thorate based materials are preferred and they satisfy the criteria of larger ionic radii of A and B site cations owing to their bigger size, and larger lattice free volume [9, 10]. Further, tri-valent doped a $BaCeO_3$

and $BaZrO_3$ have been studied extensively for their proton conduction application [11-14]. A very limited literature is available on the studies of thorate based perovskites [9, 15, 16] that has provided a scope to explore the preparation and electrical conductivity behavior of pristine and ytterbium substituted barium thorate in oxygen and hydrogen ambiences.

4.1.1. Structure of $BaThO_3$

$BaThO_3$ is cubic structure with the space group of pm3m [17] which is shown in Fig 4.1. Murtaza et al. [18] reported the energy gap between the valence and conduction band as 3.33 eV.

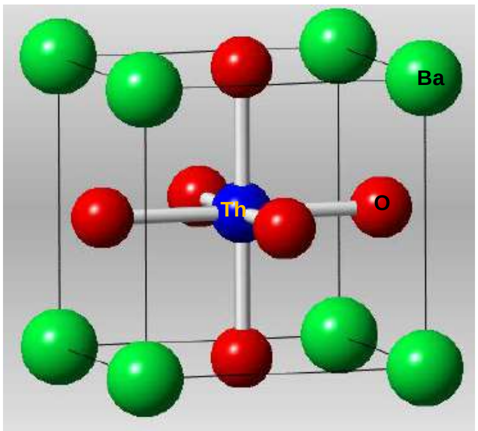

Figure 4. 1 Structure of Barium thorate

4.2. Theoretical background for the synthesis of $BaThO_3$

Yuji Ohishi et al. [19] prepared $BaThO_3$ from solid state reaction of $BaCO_3$ and ThO_2 under dry air at 1673 K. Equation 4.1 shows the formation of $BaThO_3$.

$$BaCO_3 + ThO_2 \rightarrow BaThO_3 + CO_2 \qquad (4.1)$$

The above equation suggests that the partial pressure of CO_2 plays a key role in the product formation. The interplay between pCO_2 and temperature may result in low temperature synthesis of the compound. The equilibrium pCO_2 of the reaction (equation .4.1) at 1100 K is calculated to be 0.0023 atm (from Gibbs energy data) [20, 21]. A marginal increase in pCO_2 (0.0026 atm) will inhibit the forward reaction. That is, the Gibbs energy of formation of $BaThO_3$ becomes positive. Even though the atmospheric CO_2 is only 0.00039 atm, the CO_2 released during the decomposition can facilitate the reverse reaction. Hence the removal of CO_2 becomes inevitable to favour only the forward reaction and obtain phase pure $BaThO_3$. Thus, a modified solid state method under vacuum was adopted to synthesize pristine and ytterbium substituted $BaThO_3$.

4.3. Experimental

4.3.1. Modified solid state reaction (MSSR) method

Nominal composition of perovskite samples of $BaTh_{1-x}Yb_xO_{3-\delta}$ (x= 0 - 0.2) were prepared using the precursors $BaCO_3$ (99.9%), Yb_2O_3 (99.99%) and ThO_2 (99.9%). Thorium oxide was obtained from the thermal decomposition of thorium oxalate which was precipitated from thorium nitrate [22]. The calcination and sintering procedure were already discussed in the chapter-2. In this chapter, details of various characterization techniques such as X-ray diffraction, helium pycnometry, infrared (IR) spectroscopy, scanning electron microscopy and electrical conductivity measurements using ac impedance spectroscopy in the temperature range from 573 - 873 K in various atmospheres are discussed.

4.4. Results and Discussion

4.4.1. Phase and morphological characterization

Figure 4.2 (a) shows the formation of barium thorate at 1100 K under vacuum that was reported for the first time in the literature to the best of our knowledge. Similar observations in Figure 4.2 (b)-(d) were observed for Yb substituted samples. In addition to $BaThO_3$, un-reacted ThO_2 (#) signatures were also observed in all these samples. The peaks attributed to the precursor, revealed the incompletion of reaction at this temperature for 24 h. Prolonged heating under vacuum for more than 24 h, may tend to reduce the ThO_2 phases. Fig. 4.3 shows the X-ray powder diffraction patterns of the $BaTh_{1-x}Yb_xO_{3-\delta}$ (where x = 0 - 0.2) which was calcined at 1373 K under argon flow. It shows evidently the existence of a single phase up to nominal composition of $BaTh_{0.85}Yb_{0.15}O_{3-\delta}$, which is much similar to that of pristine, $BaThO_3$. All diffraction peaks between 15° and 85° of the nominal compositions of $BaTh_{1-x}Yb_xO_{3-\delta}$ (where x = 0 - 0.15) were indexed according to cubic $BaThO_3$ (JCPDS card 75-0432) with a space group Pm3m. On introduction of Yb, there was no significant change observed in two theta for all the nominal compositions compared to the parent $BaThO_3$. Using linear least square fit algorithm, the lattice parameter (a = b = c) of the pristine compound was calculated to be 4.491 Å ± 0.002, which was in good agreement with the data reported by Yuji Ohishi et al. [19]. The lattice parameter for all the nominal compositions is shown in Table 4.1. Only a minor variation in the lattice parameter was observed between the pristine and all the samples. In case of the nominal composition $BaTh_{0.8}Yb_{0.2}O_{3-\delta}$, secondary phase peaks attributed to ThO_2 (#111) and Yb_2O_3 (*222) (Fig. 4.3(e)) were observed, indicating the solubility limit of Yb_2O_3 in $BaThO_3$ lies between x = 0.15 and x = 0.20.

Table 4. 1 Estimated lattice parameter of nominal composition $BaTh_{1-x}Yb_xO_{3-x/2}$ using the data obtained from XRD studies

Compound	Lattice Parameter $a = b = c$ (Å)
$BaThO_3$	4.491 ± 0.002
$BaTh_{0.95}Yb_{0.05}O_{2.975}$	4.483 ± 0.003
$BaTh_{0.9}Yb_{0.1}O_{2.95}$	4.482 ± 0.003
$BaTh_{0.85}Yb_{0.15}O_{2.925}$	4.482 ± 0.002

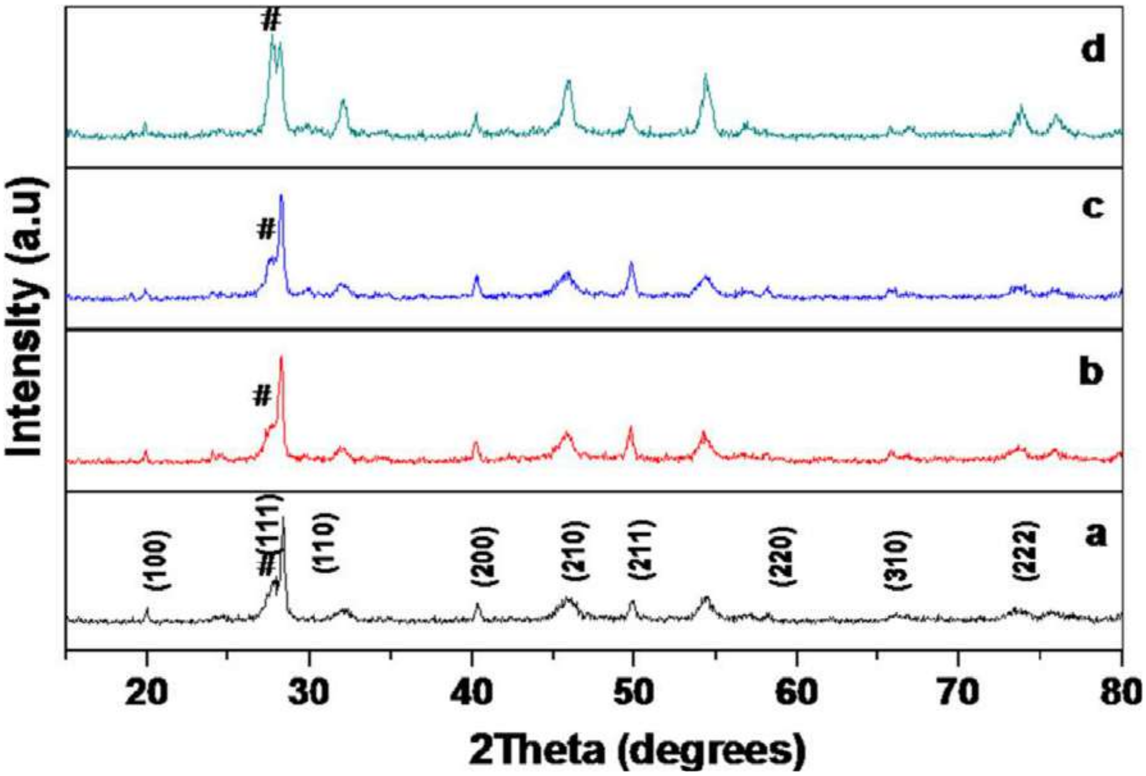

Figure 4. 2 XRD pattern of (a) $BaThO_3$, nominal compositions (b) $BaTh_{0.95}Yb_{0.05}O_{2.975}$, (c) $BaTh_{0.9}Yb_{0.1}O_{2.95}$ and (d) $BaTh_{0.85}Yb_{0.15}O_{2.925}$ at 1100 K under vacuum. (# Indicates ThO_2)

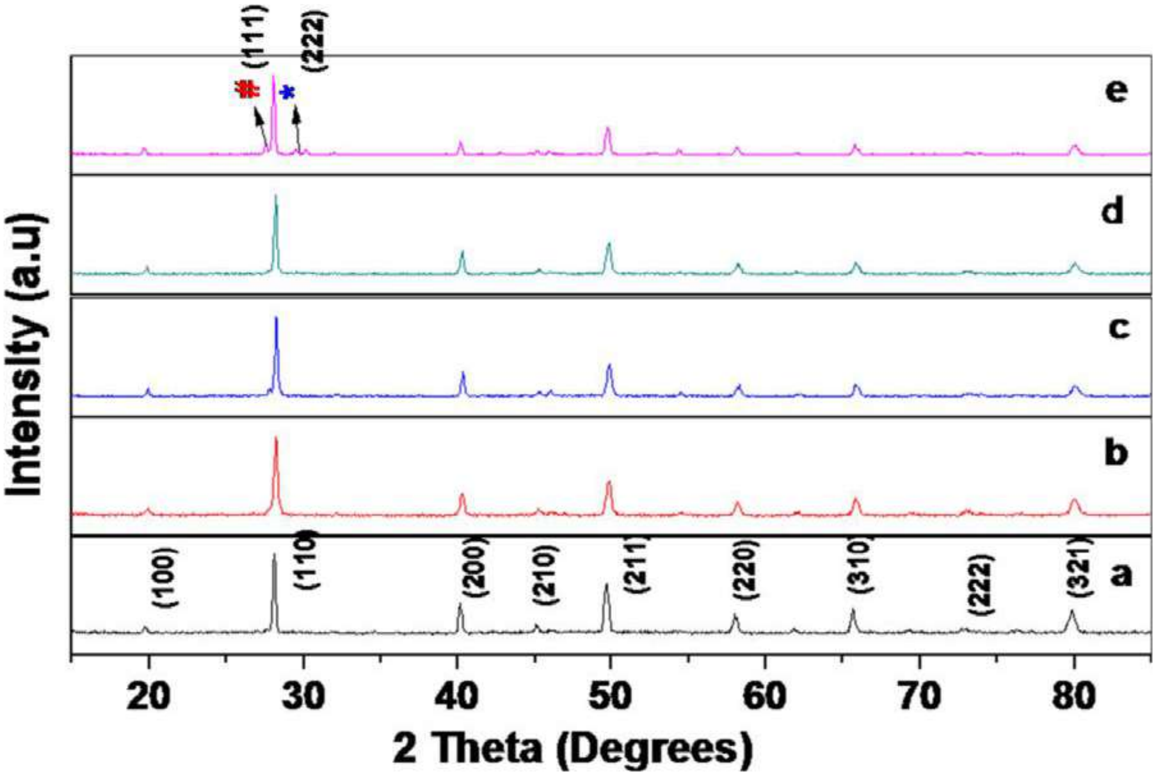

Figure 4. 3 XRD pattern of (a) $BaThO_3$, nominal compositions (b) $BaTh_{0.95}Yb_{0.05}O_{2.975}$, (c) $BaTh_{0.9}Yb_{0.1}O_{2.95}$, (d) $BaTh_{0.85}Yb_{0.15}O_{2.925}$, and (e) $BaTh_{0.8}Yb_{0.2}O_{2.9}$ at 1373 K under argon flow (# and * indicates precipitation of ThO_2 and Yb_2O_3 respectively)

The density of the sintered pellets obtained by both geometrical and helium pycnometer methods is shown in Table 4.2. The values were about 95 % of the theoretical densities of these ceramics. A marginal difference was observed between the pycnometrically derived values with those from physical measurements that indicate samples possessed negligible open pores.

Table 4. 2 Comparison of density measurement results from geometrical and helium pycnometry for nominal compositions, $BaTh_{1-x}Yb_xO_{3-\delta}$ (x=0 - 0.20)

Compound	% of theoretical density	
	Geometrical measurements	Helium Pycnometry
$BaThO_3$	93.57	95.74
$BaTh_{0.95}Yb_{0.05}O_{2.975}$	94.28	95.14
$BaTh_{0.9}Yb_{0.1}O_{2.95}$	93.03	95.19
$BaTh_{0.85}Yb_{0.15}O_{2.925}$	92.55	95.03
$BaTh_{0.8}Yb_{0.2}O_{2.90}$	92.17	94.14

Figure 4.4 (a) to (d) shows the SEM images of calcined $BaTh_{1-x}Yb_xO_{3-\delta}$ (x = 0 - 0.15), which showed granular morphology of the grains. Typical granule size of all the samples was found to be in the range of 100 - 500 nm. All the compositions were found to be highly densified. This indicated the absence of significant change in grain growth on introduction of Yb_2O_3 in $BaThO_3$. The ratio of atomic percent of thorium to ytterbium in these compositions analysed by EDX are presented in Table 4.3. The semi - quantitative measurements of atomic ratios were in good agreement, within ± 5% of the theoretical values.

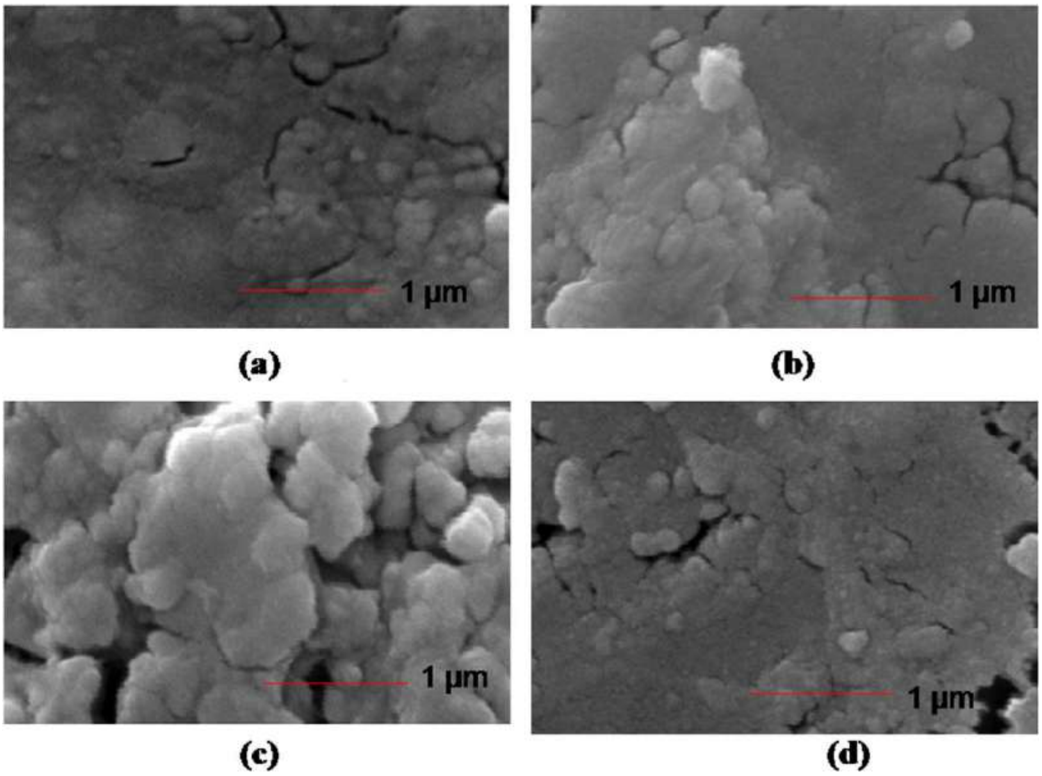

Figure 4. 4 Microstructure of the samples calcined at 1373 K (a) $BaThO_3$, (b) $BaTh_{0.95}Yb_{0.05}O_{2.975}$, (c) $BaTh_{0.9}Yb_{0.1}O_{2.95}$ and (d) $BaTh_{0.85}Yb_{0.15}O_{2.925}$

Table 4. 3 Semi - quantitative analysis of $BaTh_{1-x}Yb_xO_{3-\delta}$ (x=0 - 0.15) by EDX studies

Compound	**Ratio of atom % of Th to Yb**	
	Obtained from formula	**Data obtained from EDX**
$BaThO_3$	-	-
$BaTh_{0.95}Yb_{0.05}O_{2.975}$	19	19.4
$BaTh_{0.9}Yb_{0.1}O_{2.95}$	9	8.8
$BaTh_{0.85}Yb_{0.15}O_{2.925}$	5.7	5.9

4.4.2. Electrical conductivity of $BaTh_{1-x}Yb_xO_{3-\delta}$ (x = 0 - 0.15)

The Nyquist plots drawn from the impedance data obtained for all the samples could only be fitted with single semicircle (Equivalent fit shown in the inset of Figure 4.5) using Z®view (version 2.8). No inter/intra grain boundary conductivities were able to resolve in the temperature range under study. Typical fit parameters for a sample studied under hydrogen ambience were provided in section 4.4.2.3. Similar procedure was adopted for the analysis of all the samples in different ambience considered. The electrical conductivity was reversible and no hysteresis was observed in the entire temperature range from 573 – 873 K in O_2, 80 ppm hydrogen in argon & 100 % hydrogen during the temperature cycling. The maximum error in the conductivity measurement of the pristine and all the samples in various ambiences in the entire temperature range were found to be ± 0.02 %.

4.4.2.1. In oxygen ambience

The typical Cole-Cole plot of $BaTh_{1-x}Yb_xO_{3-\delta}$ (x = 0 - 0.15) recorded in oxygen at 573 K is shown in Fig. 4.5. All the samples showed a nearly same semicircular pattern, suggesting an identical conduction process. The conductivity values of the samples were deduced from the real axis intercept of the trace at low frequency. The resistance of the compound decreased gradually for the Yb^{3+} substituted specimens up to x = 0.15 compared to the pristine compound. The conductivity measurement was not carried out for the nominal composition of $BaTh_{0.8}Yb_{0.2}O_{2.9}$, which showed the impurity phases, as discussed in X-ray diffraction studies. As temperature increased a significant reduction in the resistance was observed. The conductivity of Yb_2O_3 in different ambience was discussed in chapter -3 (section 3.2.3.4). Typical impedance spectrum of $BaTh_{0.95}Yb_{0.05}O_{2.975}$ at two different temperatures i.e., 573 and 823 K is shown in Figure.4.6.

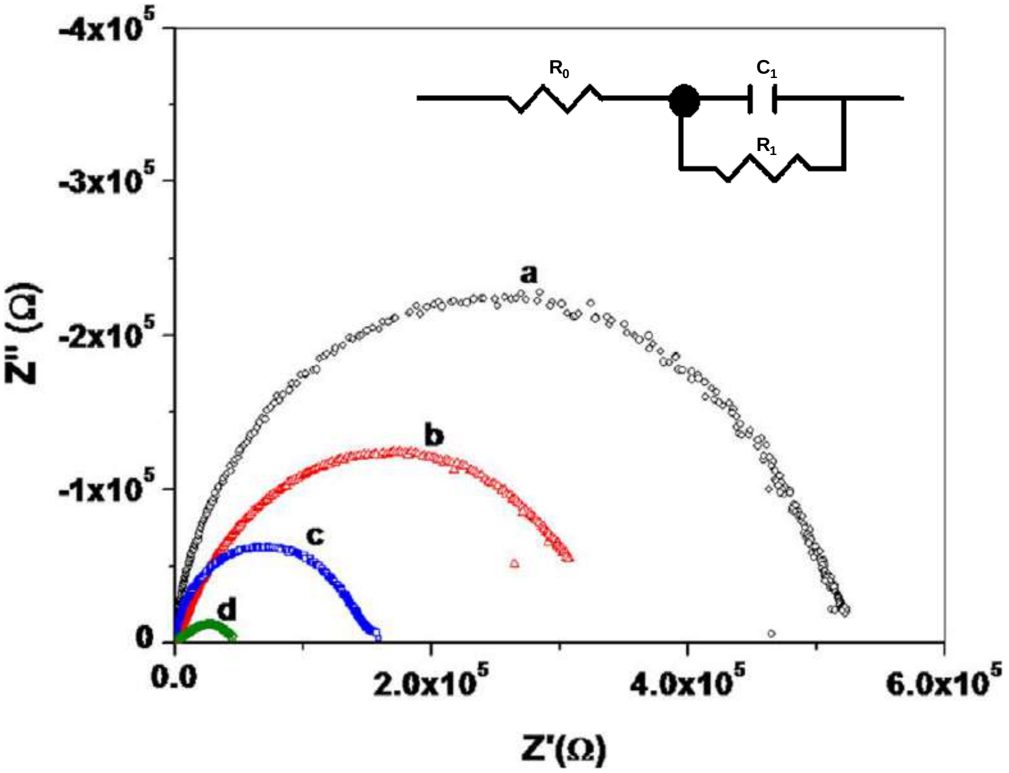

Figure 4. 5 Typical Cole - Cole plot of (a) $BaThO_3$ (b) $BaTh_{0.95}Yb_{0.05}O_{2.975}$ (c) $BaTh_{0.9}Yb_{0.1}O_{2.95}$ and (d) $BaTh_{0.85}Yb_{0.15}O_{2.925}$ recorded in O_2 at 573 K. (Equivalent circuits used for fitting complex impedance data. Ro - contact resistance, R_1 bulk resistance, and C_1 - capacitance)

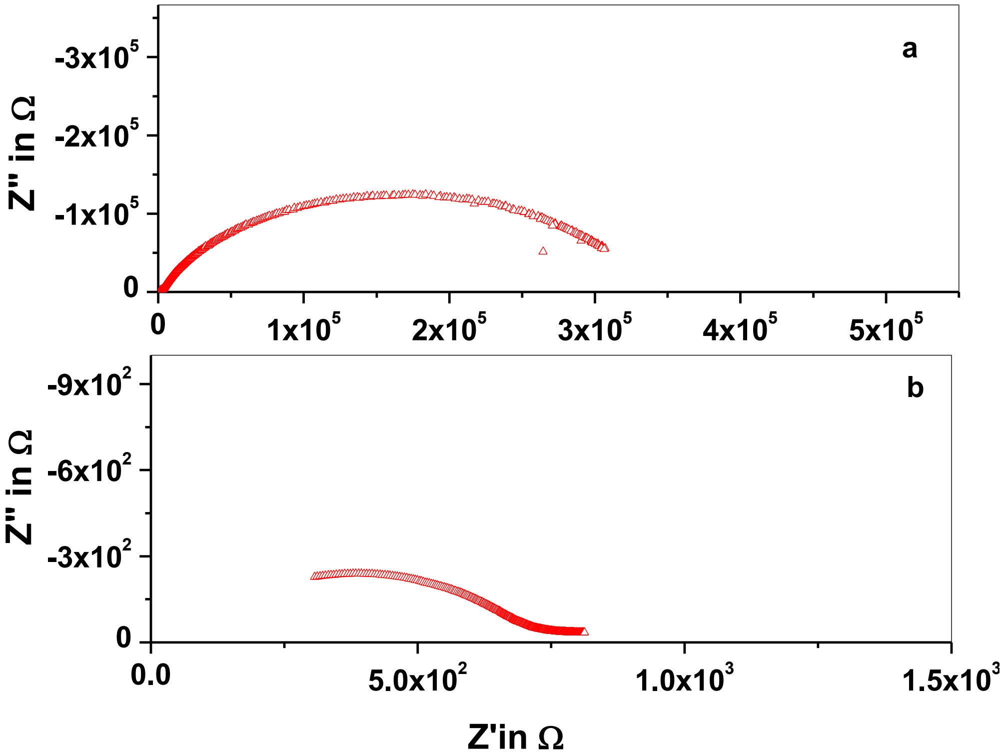

Figure 4. 6 Typical Cole – Cole plot of $BaTh_{0.95}Yb_{0.05}O_{2.975}$ recorded in O_2 (a) 573 and (b) 823 K

Figure 4.7 shows the electrical conductivity of $BaTh_{1-x}Yb_xO_{3-\delta}$ (x = 0 - 0.15) sample in O_2 as a function of reciprocal temperature (Arrhenius - like behavior). On introduction of ytterbium, a marginal variation in the conductivity was observed between the pristine and all the nominal compositions. The difference in the conductivity was found to be one order higher for the nominal composition of $BaTh_{0.85}Yb_{0.15}O_{2.925}$ than the pristine compound in the entire range of temperature. This indicated that the incorporation of more number of anion vacancies upon Yb^{3+} substitution. This can be expressed by Kröger vink [23, 24] notation shown in the equation 4.2

$$\frac{x}{2}Yb_2O_3(ThO_2) \rightarrow xYb'_{Th} + \frac{3x}{2}O_O^x + \frac{x}{2}V_O^{\cdot\cdot} \qquad (4.2)$$

Introduction of '*x*' amount of Yb^{3+} creates only $\frac{x}{2}$ amount of oxygen vacancies that maintain electrical neutrality.

The activation energy for the conduction process was also deduced from the slopes of the Arrhenius plots. The activation energy was found to be around 0.8 eV, which suggested that, the conducting species is probably oxide ion. However, it was also observed that the activation energy of all the samples with the introduction of ytterbium remained nearly same, indicating that the conducting species and the mechanism remain unaltered.

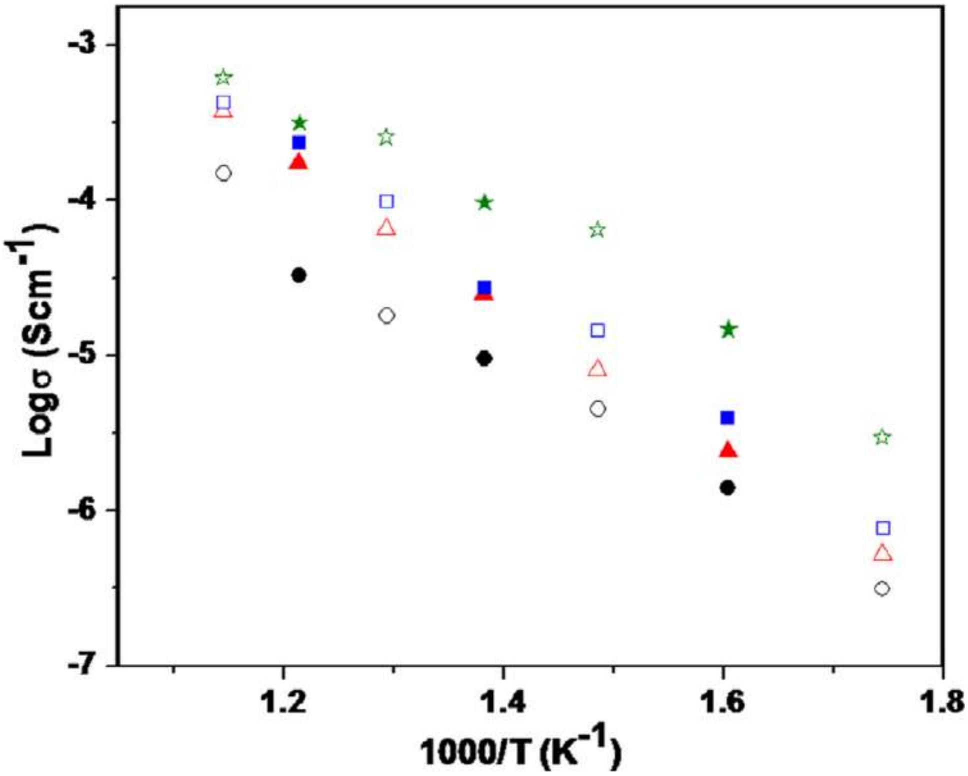

Figure 4. 7 Arrhenius plot for electrical conductivity (○) $BaThO_3$, (△) $BaTh_{0.95}Yb_{0.05}O_{2.975}$, (□) $BaTh_{0.9}Yb_{0.1}O_{2.95}$ and (☆) $BaTh_{0.85}Yb_{0.15}O_{2.925}$ recorded in O_2 in the temperature range from 573 to 873 K. The open and closed symbols indicate the cooling and heating cycles respectively

Figure 4.8 reveals the conductivity of different compositions as a function of ytterbium incorporation at different temperatures from 573 to 873 K in oxygen. It is evident that there was no significant variation in the conductivity between pristine and $BaTh_{1-x}Yb_xO_{3-\delta}$ (x = 0.05 & 0.10) in the temperature range from 573 - 673 K. However, a small difference in conductivity was observed for $BaTh_{0.85}Yb_{0.15}O_{2.925}$ at low temperature. The difference in the conductivity increased gradually and reaches the maximum for the specimen with x = 0.15 in the oxygen ambience at 873 K. This indicated that the oxide ion conductivity was larger for the higher substitution of ytterbium that could be due to more anion vacancies created as mentioned earlier section 4.4.2.1.

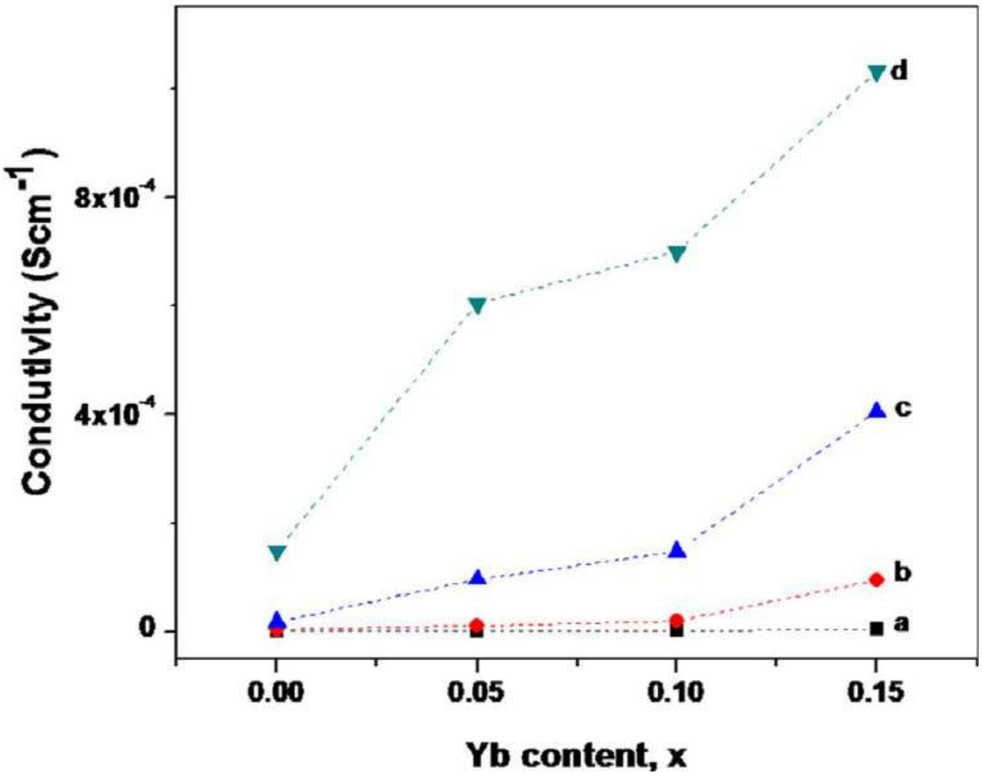

Figure 4. 8 The plot of Yb content (x), against conductivity of $BaTh_{1-x}Yb_xO_{3-\delta}$ (x = 0–0.15) in O_2 at different temperatures (a) 573, (b) 673, (c) 773 and (d) 873 K

4.4.2.2. In 80 ppm hydrogen in argon ambience

Figure 4.9 shows the electrical conductivities of $BaTh_{1-x}Yb_xO_{3-\delta}$ (x = 0 - 0.15) sample in 80 ppm hydrogen in argon as a function of reciprocal temperature. On introduction of ytterbium, a marginal increase in the conductivity was observed between the pristine and the nominal compositions of $BaTh_{1-x}Yb_xO_{3-\delta}$ (x = 0.05 & 0.10). From the figure as observed, the conductivity decreased for the specimen with x = 0.15 compared to the pristine compound in the entire range of temperature. However, the reason for the decrease in conductivity for the nominal composition of $BaTh_{0.85}Yb_{0.15}O_{2.925}$ is not evident.

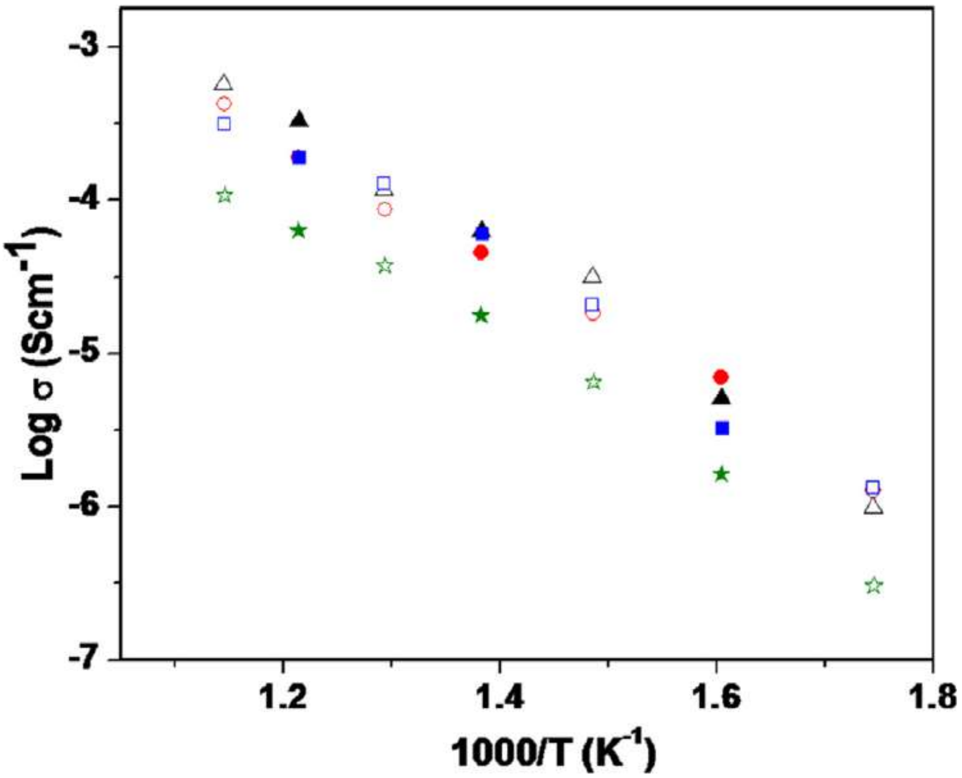

Figure 4. 9 Arrhenius plot for electrical conductivity (○) $BaThO_3$, (△) $BaTh_{0.95}Yb_{0.05}O_{2.975}$, (□) $BaTh_{0.9}Yb_{0.1}O_{2.95}$ and (☆) $BaTh_{0.85}Yb_{0.15}O_{2.925}$ recorded in 80 ppm H_2 in argon in the temperature range from 573 to 873 K. The open and closed symbols indicate the cooling and heating cycles respectively

4.4.2.3. In 100% hydrogen ambience

Figure 4.10 shows the typical Cole –Cole plot of $BaTh_{1-x}Yb_xO_{3-\delta}$ (x = 0 - 0.15) recorded in H_2 at 573 K. The lowering of resistance in $BaTh_{1-x}Yb_xO_{3-\delta}$ (x = 0, 0.05 & 0.1) after exposure to 100 % H_2 compared to that of oxygen ambience was observed. This is probably due to the mixed proton and electronic conduction. In a classical review, Tao et al. [25] described the interaction of lattice oxygen with moisture-free hydrogen to form hydroxyl bond with the liberation of electrons that can lead to mixed proton conductivity in perovskites as observed in the current study. The conductivity is observed to be higher for the $BaTh_{1-x}Yb_xO_{3-\delta}$ (x = 0.05 & 0.1) compared to the parent compound as shown in 80 ppm H_2 in argon. However, no significant variation in the resistance was observed between specimen with x = 0.05 & 0.10. Further, the resistance increased for the specimen with (x = 0.15) and was found to be approximately 4 times higher than the pristine and all other nominal compositions. It was observed that on introduction of 80 ppm hydrogen, the decrease in conductivity was about half-an-order compared to the pristine compound. However, in 100% hydrogen atmosphere, the conductivity was further reduced. This observation confirmed the influence of both ytterbium concentration level and hydrogen concentration in the ambience with the combined effect on the conductivity. The interplay of these two factors on conductivity was not clearly evident from the present experiments. Similar to oxygen ambience, the resistance decreased with increase in temperature in hydrogen ambience. Figure. 4.11 shows the impedance spectrum of $BaTh_{0.95}Yb_{0.05}O_{2.975}$ recorded at 573 and 823 K. Typical estimated values of impedance obtained from the complex non-linear least square fitting for all the compositions at 573 and 823 K are shown in Table 4.4. Similarly, high conductivities were reported for doped barium cerates (which also belong to perovskite family) in dry hydrogen by Petit et al. [26]. The consolidated conductivity values observed for the pristine and all the samples in O_2, 80 ppm H_2 in argon and H_2 are presented in Table 4.5.

Table 4. 4 Estimated values obtained from complex nonlinear least square fitting of impedance data recorded in H_2 for the nominal composition $BaTh_{1-x}Yb_xO_{3-x/2}$

Compound	**Temperature (°C)**	**R_0 (Ohm)**	**R_1 (Ohm)**	**C_1 (Farad)**
$BaThO_3$	300	1089	1.08E+05	4.49E-11
	550	30.55	6.551	5.32E-06
$BaTh_{0.95}Yb_{0.05}O_{2.975}$	300	1049	7.51E+04	4.41E-11
	550	13.1	5.22	1.10E-05
$BaTh_{0.9}Yb_{0.1}O_{2.95}$	300	935	7.49E+04	5.13E-11
	550	21.38	9.25	4.48E-06
$BaTh_{0.85}Yb_{0.15}O_{2.925}$	300	1145	2.91E+05	5.08E-11
	550	417.5	168.9	5.31E-07

Table 4. 5 Conductivity of nominal compositions, $BaTh_{1-x}Yb_{x}O_{3-\delta}$ (x=0 - 0.15) in different ambience such as O_{2}, 80 ppm H_{2} in argon and H_{2}

Compound	**Conductivity (Scm^{-1}) [573- 873] K [Error ± 0.02%]**		
	O_2	**80 ppm H_2 in Ar**	**H_2**
$BaThO_3$	$3.13\ x10^{-7}$ - $1.49X10^{-4}$	$1.28\ x10^{-6}$ - $4.23\ x10^{-4}$	$1.36x10^{-6}$ - $4.35\ x10^{-3}$
$BaTh_{0.95}Yb_{0.05}O_{2.975}$	$5.83x10^{-7}$ - $6.04x10^{-4}$	$1.15\ x10^{-6}$ - $9.56\ x10^{-4}$	$2.21\ x10^{-6}$ - $9.31\ x10^{-3}$
$BaTh_{0.9}Yb_{0.1}O_{2.95}$	$8.74x10^{-7}$ - $6.99x10^{-4}$	$1.54\ x10^{-6}$ - $5.11\ x10^{-4}$	$1.54\ x10^{-6}$ - $6.12\ x10^{-3}$
$BaTh_{0.85}Yb_{0.15}O_{2.925}$	$3.62x10^{-6}$ - $1.03x10^{-3}$	$0.32\ x10^{-6}$ - $1.60\ x10^{-4}$	$0.48\ x10^{-6}$ - 3.2710^{-4}

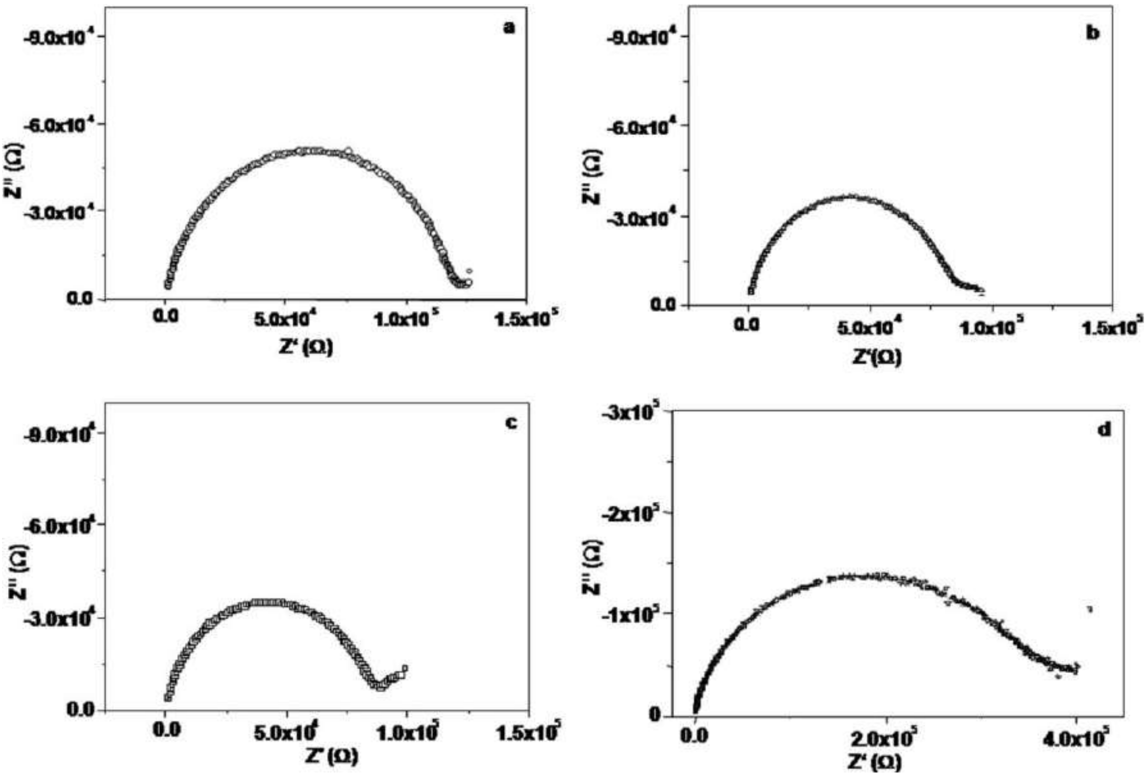

Figure 4. 10 Typical Cole - Cole plots of (a) $BaThO_3$, (b) $BaTh_{0.95}Yb_{0.05}O_{2.975}$, (c) $BaTh_{0.9}Yb_{0.1}O_{2.95}$ and (d) $BaTh_{0.85}Yb_{0.15}O_{2.925}$ recorded in H_2 at 573 K

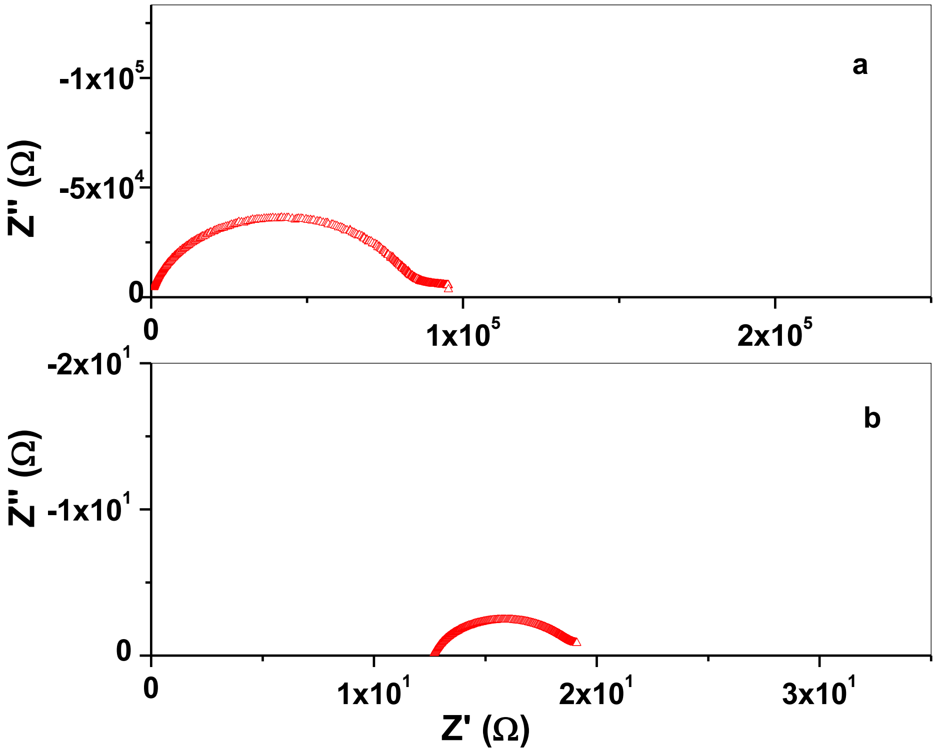

Figure 4. 11 Typical Cole – Cole plot of $BaTh_{0.95}Yb_{0.05}O_{2.975}$ recorded in H_2 (a) 573 and (b) 823 K

The electrical conductivity of $BaTh_{1-x}Yb_xO_{3-\delta}$ (x = 0 - 0.15) in H_2 as a function of reciprocal temperature is shown in Fig. 4.12. From the figure, the conductivity is not showing linear behavior with temperature for all the samples in the hydrogen ambience in the entire range of temperature. Similarly, non-linear behavior of conductivity with temperature was reported for doped barium cerates by Islam et al. [27]. The conductivity of the pristine and $BaTh_{1-x}Yb_xO_{3-\delta}$ (x = 0, 0.05 & 0.10) showed an order higher in hydrogen than in oxygen. In hydrogen atmosphere, possible incorporation of the proton in the sample might have taken place, during the equilibration of the sample at high temperature that might have caused to increase the conductivity [28]. The average ratio of the conductivity value of the nominal composition of $BaTh_{0.95}Yb_{0.05}O_{2.975}$ was found to be 1.5 times higher than the pristine compound for the entire range of temperature. Further addition of ytterbium, this ratio gradually decreased. From the figure as observed, the conductivity of the specimen with x = 0.15 was found to be an order less compared to the pristine compound. The activation energy for the conduction process in hydrogen for all compositions except, $BaTh_{0.85}Yb_{0.15}O_{2.925}$ was found to be in the range 0.6 to 0.8 eV, which is in a good agreement with reported values [29]. However the composition, $BaTh_{0.85}Yb_{0.15}O_{2.925}$ showed lower activation energy i.e. 0.3 eV, even though the conductivity was found to be almost the same for the temperature range of 673 – 873 K. The reason for the lower activation energy is not evident. In the low temperature range, i.e. below 673 K, all the compositions exhibited activation energy of about 1.4 eV for the conduction process. These results clearly indicated that all the compositions exhibited a transformation from low conducting phase to high conducting structure at about 673 K in presence of hydrogen. More detailed experiments may be required to elucidate the features attributing to the difference in conductivity of these phases. The combined activation energy values observed for the pristine and all the samples in O_2, 80 ppm H_2 in argon and H_2 are presented in Table 4.6.

Table 4. 6 Activation energy for the conductivity process exhibited by the nominal composition of $BaTh_{1-x}Yb_xO_{3-\delta}$ (x=0 - 0.15) in different ambiance ie O_2, 80 ppm H_2 in argon and H_2

Compound	**E_a (eV)**			
	O_2	**80 ppm H_2 in Ar**	**H_2**	
	[573-873] K	**[573-873] K**	**[573-723] K**	**[673-873] K**
$BaThO_3$	0.75 ± 0.04	0.73 ± 0.02	1.60 ± 0.21	0.58 ± 0.10
$BaTh_{0.95}Yb_{0.05}O_{2.975}$	0.91 ± 0.01	0.87 ± 0.04	1.56 ± 0.26	0.63 ± 0.04
$BaTh_{0.9}Yb_{0.1}O_{2.95}$	0.85 ± 0.03	0.80 ± 0.05	1.45 ± 0.29	0.77 ± 0.05
$BaTh_{0.85}Yb_{0.15}O_{2.925}$	0.72 ± 0.05	0.81 ± 0.04	1.39 ± 0.20	0.30 ±0.05

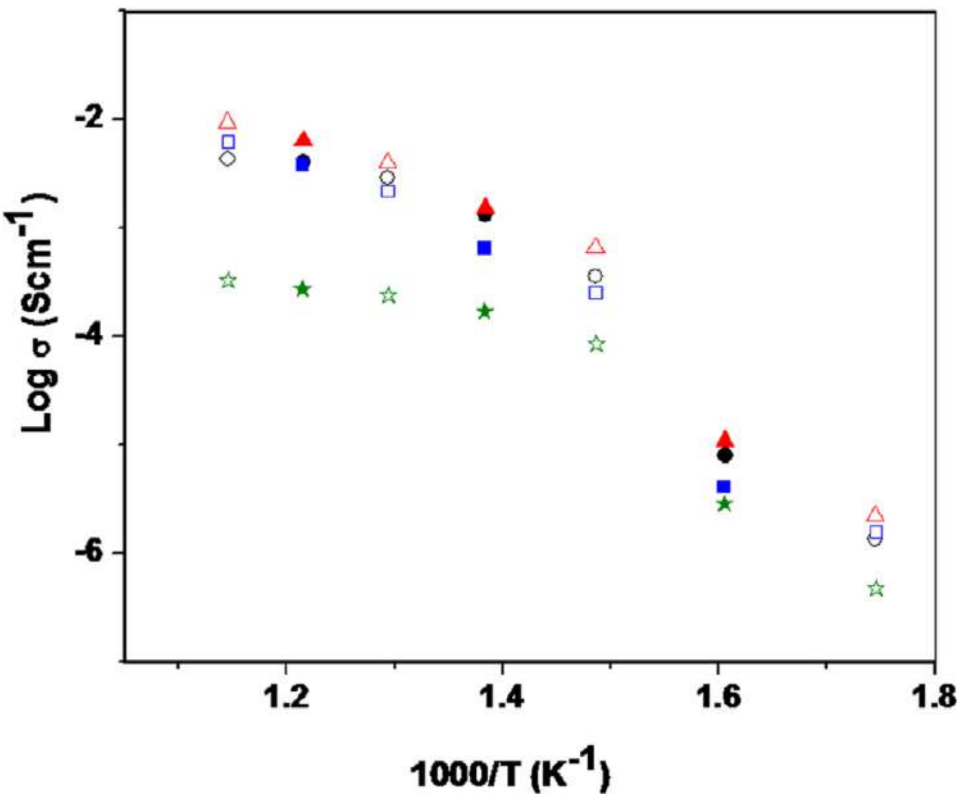

Figure 4. 12 Arrhenius plot for electrical conductivity (○) $BaThO_3$, (△) $BaTh_{0.95}Yb_{0.05}O_{2.975}$, (□) $BaTh_{0.9}Yb_{0.1}O_{2.95}$ and (☆) $BaTh_{0.85}Yb_{0.15}O_{2.925}$ recorded in H_2 in the temperature range from 573 to 873 K, The open and closed symbols indicate the cooling and heating cycles respectively

4.4.2.4. Effect of dopant concentration on conductivity in H_2 ambience

Figure 4.13 shows the plot of the dependence of total conductivity with ytterbium concentration in hydrogen ambience. No significant change in the conductivity was observed for all the samples in the temperature range from 573 – 673 K. Compared to the parent compound, the conductivity decreased with increasing temperature for the nominal composition of $BaTh_{1-x}Yb_xO_{3-\delta}$ (x = 0.10 & 0.15) except for the nominal composition of $BaTh_{0.95}Yb_{0.05}O_{2.975}$. No significant variation in the conductivity was observed for the nominal composition of $BaTh_{0.85}Yb_{0.15}O_{2.925}$ in the temperature range from 573 – 873 K. The specimen with x = 0.05 showed the highest conductivity compared to all the samples. This result established the desired concentration of ytterbium in barium thorate for the maximum conductivity in hydrogen ambience.

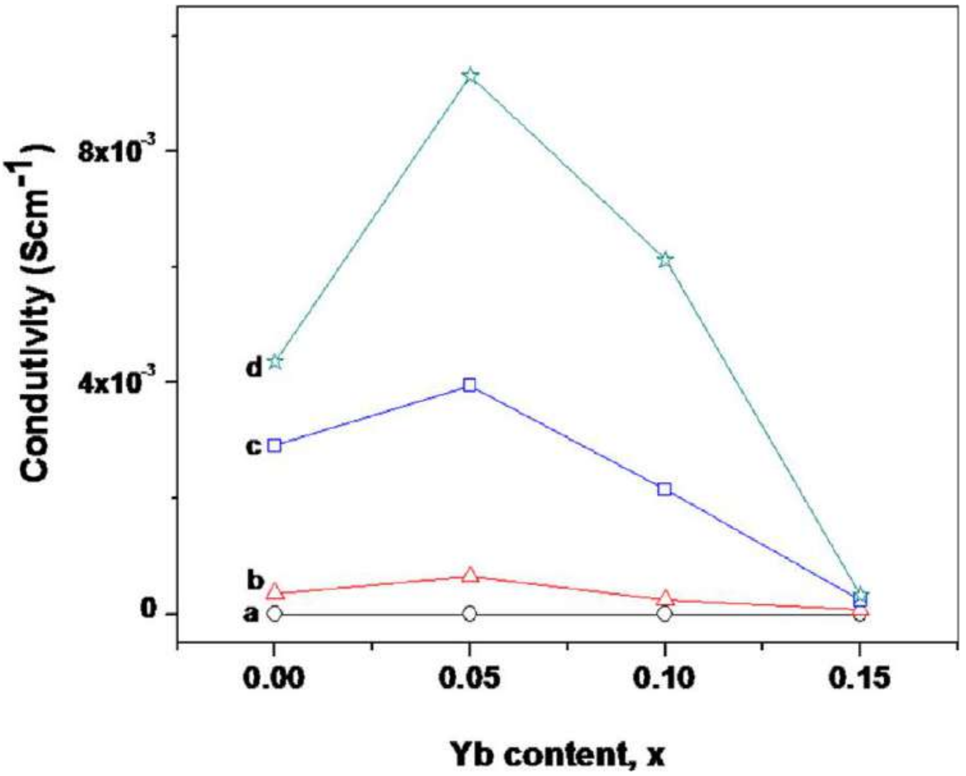

Figure 4. 13 The plot of Yb content (x), against conductivity of $BaTh_{1-x}Yb_xO_{3-\delta}$ (x = 0 – 0.15) in H_2 at different temperatures (a) 573, (b) 673, (c) 773 and (d) 873 K

4.4.3 Elucidation of hydrogen retention in thorate matrix

Studies in section 4.4.2.1 and 4.4.2.3 indicated lower conductivity of nominal compositions in oxygen ambience than in hydrogen. The hydrogen-exposed samples were equilibrated in oxygen atmosphere as described in section 4.4.2.1, to understand the regeneration or retrace nature of conductivity. At different time intervals (24 h, 48 h and 96 h) their respective conductivities in the temperature range of study were recorded. Typical conductivity behavior of $BaTh_{0.9}Yb_{0.1}O_{2.95}$ a) in O_2, b) in H_2 and (c) to (e) during recovery in O_2 ambience after 24 h, 48 h and 96 h after exposure to H_2 respectively is shown in Fig. 4.14. After equilibrating for 24 h in oxygen ambience (after exposure to H_2), the conductivity values remained close to that of hydrogen equilibrated sample (c (□)). The conductivity measured after equilibration for 48 h is indicated by (d (☆)). The measured values were slightly different from that of (c (□)). The equilibration studies were further continued and conductivity measurements were performed after 96 h (e (⊕)). These values were close to that of oxygen equilibrated sample, indicating the acceptable retrace of the conductivity back to its original values. This behavior suggested the incorporation of hydrogen into the thorate matrix during the equilibration with hydrogen atmosphere which was removed again on its equilibration with oxygen equilibration at high temperature for long duration. To elucidate this behavior, infra red spectra were recorded for the samples exposed to deuterium. Typical IR spectra of $BaTh_{0.95}Yb_{0.05}O_{2.975}$ are shown in Fig. 4.15. Before exposure to D_2, the compound exhibited characteristic peaks at 3576 cm^{-1} due to O-H stretching, a possible interference from moisture (Fig. 4.15 (a)). The sample exposed to deuterium for 24 h shows O-D stretch at 2630 cm^{-1} also an O-H stretch at 3570 cm^{-1}(Fig. 4.15 (b)). Observation of O-D stretch at 2630 cm^{-1} confirmed the incorporation of deuterium in the matrix. The O-H (3605), O-D (2662) and ThO_2 (860) cm^{-1} stretching frequencies are compared with those reported in the literature for the compound viz. $SrCe_{0.95}Y_{0.05}O_{3-\delta}$ [30] and ThO_2 [31]. The incorporated deuterium was removed by heating the sample in oxygen ambience for 96 h which showed no stretching frequency corresponding to O-D and O-H (Fig. 4.15(c)). Thus, the IR studies ensured the removal incorporated H/D in the samples by heating in oxygen at high temperature. In nutshell, the conductivity experiments and IR studies with deuterium clearly established the incorporation of hydrogen in thorate matrix.

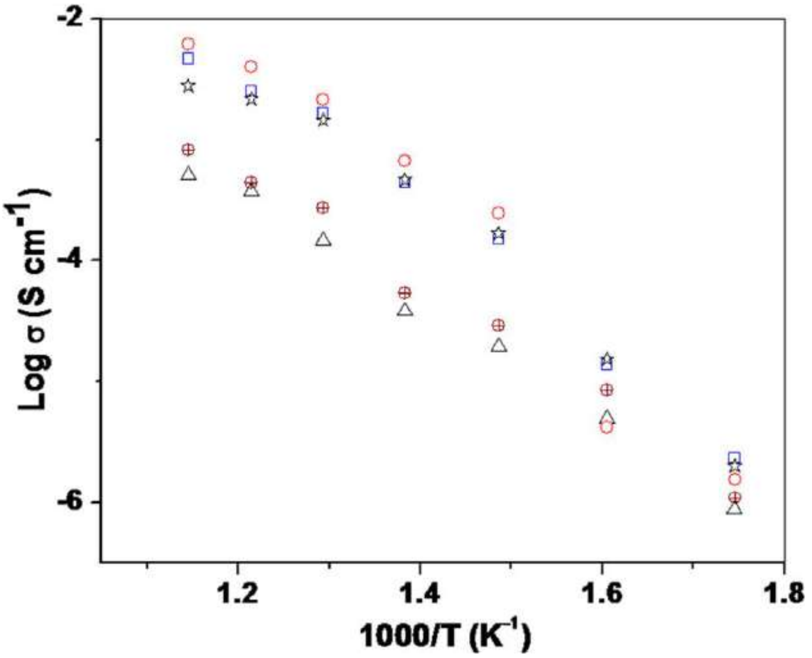

Figure 4. 14 Electrical conductivity behavior of $BaTh_{0.9}Yb_{0.1}O_{2.95}$ in presence of [a] (△) O_2, [b] (○) H_2 and during recovery in O_2 ambience after [c] (□) 24h, [d] (☆) 48 h and [e] (⊕) 96 h

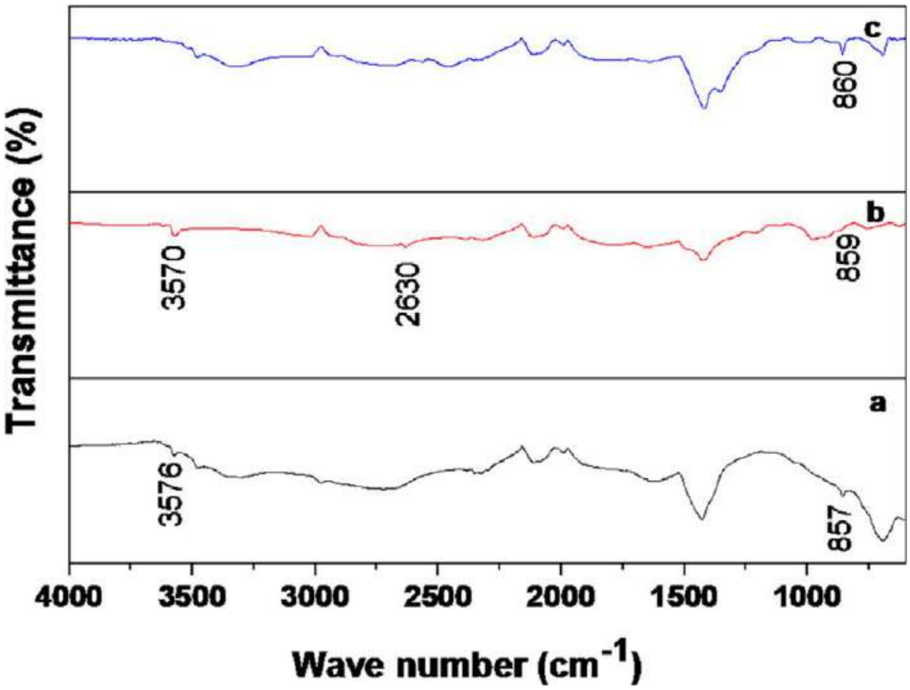

Figure 4. 15 IR Spectra of (a) Un-exposed $BaTh_{0.95}Yb_{0.05}$ $O_{2.975}$, (b) $BaTh_{0.95}Yb_{0.05}$ $O_{2.975}$ exposed to D_2 for 24 h (c) $BaTh_{0.95}Yb_{0.05}$ $O_{2.975}$ heated in O_2 for 96 h

4.5. Conclusions

$BaThO_3$ solid solution with ytterbium, $BaTh_{1-x}Yb_xO_{3-\delta}$ (x = 0 - 0.15) were successfully synthesized via solid state method modified under vacuum followed by argon ambience at 1100 K and 1373 K respectively. The present study highlighted the modified solid state synthesis, under vacuum and the impact of ytterbium on the conductivity of barium thorate for the first time. The solid solution formation range of ytterbium in barium thorate was found to be 15 %. Introduction of ytterbium did not influence the grain growth of barium thorate. The conductivity was influenced by the introduction of ytterbium in oxygen ambience, which was the highest for the composition, $BaTh_{0.85}Yb_{0.15}O_{2.925}$. The variation in the total conductivities of oxide ion induced by doping Yb^{3+} can be explained by the difference in electronegativity between dopant cation and oxygen anion as well as A and B-site cation both of which play critical role in the conduction mechanism. In hydrogen, the conductivities were found to be higher when compared to that in oxygen for the compositions, $BaTh_{1-x}Yb_xO_{3-\delta}$ (x = 0.05 & 0.10). However, the composition, $BaTh_{0.85}Yb_{0.15}O_{2.925}$, showed lower conductivity in hydrogen than in oxygen, which could not be explained from the present studies. Incorporation of hydrogen / deuterium in the samples was established by both conductivity measurements and infrared spectroscopic analysis.

4.6 References

[1] Q.A. Islam, S. Nag, R.N. Basu, Electrical properties of Tb-doped barium cerate, Ceramics International, 39 (2013) 6433-6440.

[2] W. Suksamai, I.S. Metcalfe, Measurement of proton and oxide ion fluxes in a working Y-doped $BaCeO_3$ SOFC, Solid State Ionics, 178 (2007) 627-634.

[3] N.V. Sharova, V.P. Gorelov, Electroconductivity and Ion Transport in Protonic Solid Electrolytes $BaCe_{0.85}R_{0.15}O_{3-\delta}$, where R is a Rare-Earth Element, Russian Journal of Electrochemistry, 39 (2003) 461-466.

[4] M.D. Gonçalves, P.S. Maram, A. Navrotsky, R. Muccillo, Effect of synthesis atmosphere on the proton conductivity of Y-doped barium zirconate solid electrolytes, Ceramics International, 42 (2016) 13689-13696.

[5] W. Sun, Z. Zhu, Z. Shi, W. Liu, Chemically stable and easily sintered high-temperature proton conductor $BaZr_{0.8}In_{0.2}O_{3-\delta}$ for solid oxide fuel cells, Journal of Power Sources, 229 (2013) 95-101.

[6] J.S. Park, J.H. Lee, H.W. Lee, B.K. Kim, Low temperature sintering of $BaZrO_3$-based proton conductors for intermediate temperature solid oxide fuel cells, Solid State Ionics, 181 (2010) 163-167.

[7] T. Ishihara, Perovskite Oxide for Solid Oxide Fuel Cells, 2009.

[8] T. Hibino, K. Mizutani, T. Yajima, H. Iwahara, Evaluation of proton conductivity in $SrCeO_3$, $BaCeO_3$, $CaZrO_3$ and $SrZrO_3$ by temperature programmed desorption method, Solid State Ionics, 57 (1992) 303-306.

[9] R.L. Cook, J.J. Osborne, J.H. White, R.C. MacDuff, A.F. Sammells, Investigations on $BaTh_{0.9}Gd_{0.1}O_3$ as an Intermediate Temperature Fuel Cell Solid Electrolyte, Journal of The Electrochemical Society, 139 (1992) L19-L20.

[10] A. Mitsui, M. Miyayama, H. Yanagida, Evaluation of the activation energy for proton conduction in perovskite-type oxides, Solid State Ionics, 22 (1987) 213-217.

[11] Y. Yamazaki, P. Babilo, S.M. Haile, Defect Chemistry of Yttrium-Doped Barium Zirconate: A Thermodynamic Analysis of Water Uptake, Chemistry of Materials, 20 (2008) 6352-6357.

[12] H. Iwahara, Technological challenges in the application of proton conducting ceramics, Solid State Ionics, 77 (1995) 289-298.

[13] N. Bonanos, K.S. Knight, B. Ellis, Perovskite solid electrolytes: Structure, transport properties and fuel cell applications, Solid State Ionics, 79 (1995) 161-170.

[14] N. Bonanos, B. Ellis, K.S. Knight, M.N. Mahmood, Ionic conductivity of gadolinium-doped barium cerate perovskites, Solid State Ionics, 35 (1989) 179-188.

[15] T. Tsuji, T. Suzuki, H. Iwahara, Electrical conduction in $BaThO_3$ doped with Nd_2O_3, Solid State Ionics, 70-71 (1994) 291-295.

[16] T. Tsuji, N. Miyajima, M. Ochida, Electrical conduction in $BaThO_3$ doped with Y_2O_3, Solid State Ionics, 79 (1995) 183-187.

[17] A.I. Lebedev, Crystal structure and properties of barium thorate $BaThO_3$ from first principles, Journal of Alloys and Compounds, 580 (2013) 487-490.

[18] G. Murtaza, I. Ahmad, B. Amin, A. Afaq, M. Maqbool, J. Maqssod, I. Khan, M. Zahid, Investigation of structural and optoelectronic properties of $BaThO_3$, Optical Materials, 33 (2011) 553-557.

[19] Y. Ohishi, E. Yusnitha, K. Kurosaki, H. Muta, S. Yamanaka, Thermophysical properties of $BaThO_3$, Journal of Nuclear Materials, 448 (2014) 62-65.

[20] R. Mishra, M. Ali, S.R. Bharadwaj, A.S. Kerkar, D. Das, S.R. Dharwadkar, Thermodynamic stability of barium thorate, $BaThO_3$, from a Knudsen effusion study, Journal of Alloys and Compounds, 290 (1999) 97-102.

[21] I. Barin, Thermochemical Data of Pure Substances, VCH Publishers, Inc., New York, NY (USA), 1995.

[22] V. Jayaraman, D. Krishnamurthy, R. Ganesan, A. Thiruvengadasami, R. Sudha, M.V.R. Prasad, T. Gnanasekaran, Development of yttria-doped thoria solid electrolyte for use in liquid sodium systems, Ionics, 13 (2007) 299-303.

[23] R.J.D. Tilley, Defects in Solids, A John Wiley & Sons, Inc.2008.

[24] T. Ishihara, Perovskite Oxide for Solid Oxide Fuel Cells, Springer 2008.

[25] Z. Tao, L. Yan, J. Qiao, B. Wang, L. Zhang, J. Zhang, A review of advanced proton-conducting materials for hydrogen separation, Progress in Materials Science, 74 (2015) 1-50.

[26] C.T.G. Petit, S. Tao, Structure and conductivity of praseodymium and yttrium co-doped barium cerates, Solid State Sciences, 17 (2013) 115-121.

[27] C.G. Fan, Z.Q. Deng, Y.B. Zuo, W. Liu, C.S. Chen, Preparation and characterization of $SrCo_{0.8}Fe_{0.2}O_{3-\delta}$–$SrSnO_3$ oxygen-permeable composite membrane, Solid State Ionics, 166 (2004) 339-342.

[28] A.F. Sammells, R.L. Cook, J.H. White, J.J. Osborne, R.C. MacDuff, Rational selection of advanced solid electrolytes for intermediate temperature fuel cells, Solid State Ionics, 52 (1992) 111-123.

[29] Matti Hotokka, Erkki J. Brändas, Jean Maruani, G. Delgado-Barrio, Advances in Quantum Methods and Applications in Chemistry, Physics, and Biology, 2013.

[30] Marianne Glerup, Finn W. Poulsen, R.W. Berg, Vibrational spectroscopy on protons and deuterons in proton conducting perovskites, Solid State Ionics, 148 (2002) 83.

[31] J.L. Bates, The absorption spectra of Thorium dioxide, Pacific Northwest Laboratory Richland, Washington, 1967.

CHAPTER 5

Chapter 5: Electrical conductivity and chemical stability of pure and Zr substituted $BaThO_3$

5.1. Introduction

In our earlier study the synthesis, characterization and electrical conductivity of the pristine and ytterbium substituted $BaThO_3$ [1] were discussed and presented in the chapter 4. However, the knowledge on stability of barium thorate in the CO_2 atmosphere is necessary for its application in any high temperature process. Literature reports poor chemical stability of it in the CO_2 environment. However, zirconium substituted cerates showed good chemical stability [2-8]. In this chapter, the solubility limit of barium zirconate in barium thorate and the effect of zirconium in $BaThO_3$ on conductivity and stability in the CO_2 atmosphere were investigated.

5.2. Experimental

5.2.1 Preparation and characterization

Nominal compositions of $BaTh_{1-x}Zr_xO_3$ (x = 0 - 0.4) were prepared using the precursors $BaCO_3$ (99.9%), Yb_2O_3 (99.99%), ZrO_2 (99.0%) and ThO_2 (99.9%) via MSSR. Further, the calcination and sintering was continued using the same procedure as discussed in the chapter 4. The various characterization techniques such as X-ray diffractometer, helium pycnometry, scanning electron microscopy, infrared spectroscopy and electrical conductivity measurements using ac impedance spectroscopy in the temperature range from 573- 873 K in three different atmospheres are described. For further evaluations, the stability of the Zr substituted barium thorate with all the nominal composition of $BaTh_{1-x}Zr_xO_3$ (x = 0 - 0.3) were continuously exposed with carbon dioxide purging with flow rate of 50 mL/min for 2 h at two different temperatures viz. 673 and 873 K and the samples collected from these experiments were ground and examined by XRD and IR spectroscopy.

5.3. Results and Discussion

5.3.1 Phase composition

Figure 5.1 shows the XRD patterns of the $BaTh_{1-x}Zr_xO_3$, (where x = 0 - 0.4) calcined under vacuum at 1100 K. Figure 5.1(a) shows the formation of barium thorate at 1100 K. Similar observations were perceived for Zr substituted samples (Fig. 5.1(b) to (e)). In addition to barium thorate, un-reacted ThO_2 (*) and precipitated ZrO_2 (#) were also observed. The peak attributed to ThO_2, revealed the incompletion of the reaction at this temperature for 24 h. The peak corresponded to the precursor, may be reduced by the continuous heating under vacuum for more than 24 h. X-ray powder diffraction patterns of samples as mentioned above calcined at 1373 K under argon flow are shown in Fig. 5.2. The existence of a single phase up to the nominal composition of $BaTh_{0.8}Zr_{0.2}O_3$ (Fig. 5.2c) is seen, which is similar to that of pristine, $BaThO_3$ (Fig. 5.2a). All diffraction peaks between 15° and 85° of the nominal compositions of $BaTh_{1-x}Zr_xO_3$ (where x = 0 - 0.2) were indexed according to cubic $BaThO_3$ (JCPDS card 75-0432) with a space group Pm3m. On introduction of Zr, the peak positions were gradually shifted to higher angles of 2θ, owing to the relatively smaller ionic radius of six coordinated Zr^{4+}, i.e., 72 pm in comparison with that of Th^{4+} with 94 pm [9]. Further contraction in the unit cell volume was observed for Zr substituted samples compared to the pristine $BaThO_3$. The lattice parameter of the $BaThO_3$ was calculated using linear least square fit algorithm and was found to be

4.491 Å ± 0.002, which is in good agreement with the reported value [10, 11]. When Zr content exceeds the level corresponding to x > 0.2, it shows the presence of a secondary phase due to its precipitation as $ZrO_2^{\#}$ at 30.269° (011) (Fig. 5.1(c-e) and Fig. 5.2 (d-e)) owing to the limited solubility of Zr in Th. These observations indicate that the solubility of ZrO_2 in $BaThO_3$ is maximum at x = 0.2. Further characterization studies were continued with the compositions $BaTh_{1-x}Zr_xO_3$, (x = 0 – 0.3).

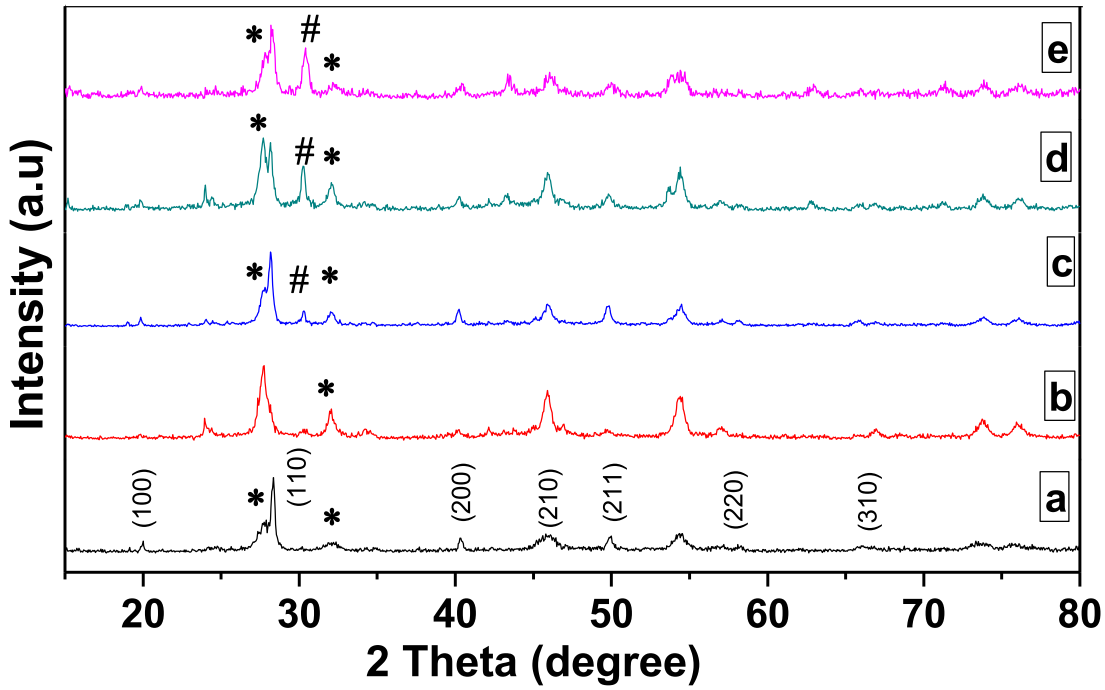

Figure 5. 1 XRD patterns of $BaTh_{1-x}Zr_xO_3$ [x = (a) 0, (b) 0.1, (c) 0.2, (d) 0.3 & (e) 0.4] calcined at 1100 K under vacuum [*ThO_2 (111) (200) and # ZrO_2 (011)]

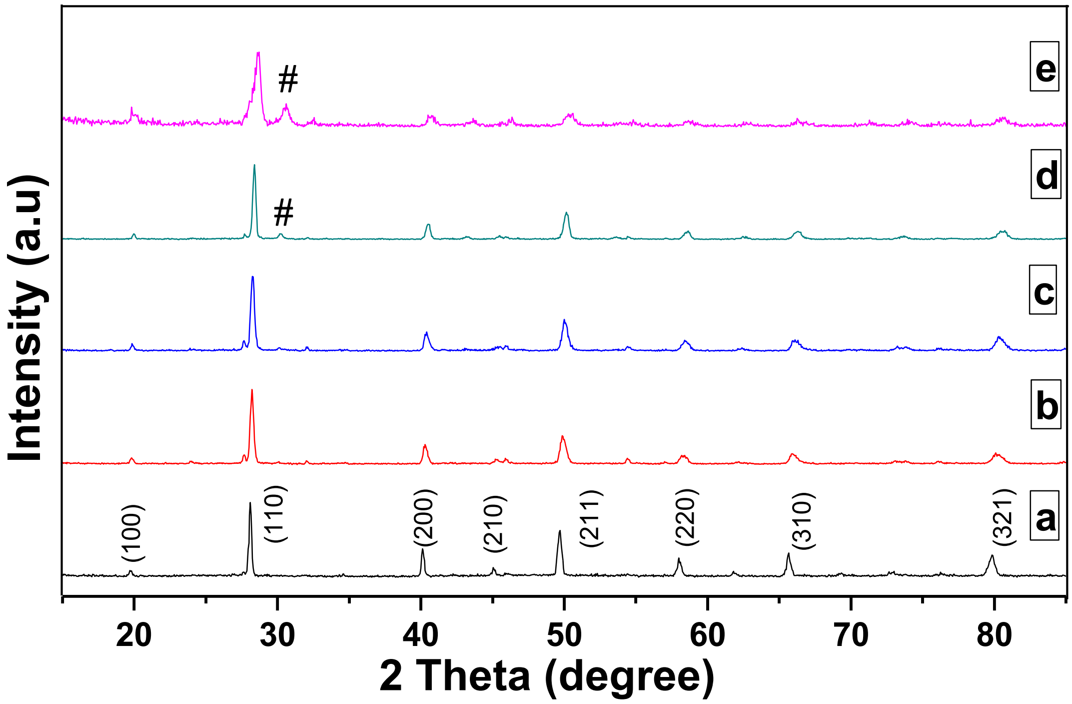

Figure 5. 2 XRD patterns of $BaTh_{1-x}Zr_xO_3$ [x = (a) 0, (b) 0.1, (c) 0.2, (d) 0.3 & (e) 0.4] calcined at 1373 K in argon flow [# ZrO_2 (011)]

The density was obtained by both geometrical and helium pycnometric methods. The percentage density[1] decreased systematically for $BaTh_{1-x}Zr_xO_3$, (where x = 0 - 0.3) and found to be 94 – 81 % and 96 - 82 % when measured by geometrical and helium pycnometric methods respectively. Helium pycnometry results reveal the systematic decrease in density for the substitution zirconium. The pores/voids may be attributed to the decrease in density, resulted by poor sintering of zirconium substituted compounds and the lowest density was exhibited for the nominal composition, $BaTh_{0.7}Zr_{0.3}O_3$. Similarly, in case of barium cerate also, the reduction in percentage density with zirconium substitution was observed due to the high temperature requirement (~ 1973 K) for sintering of $BaZrO_3$ [12, 13].

---

[1] Percentage density = (Measured density)÷(Theoretical density)×100

Figure 5.3 (a) to (d) show the morphological images of nominal compositions, $BaTh_{1-x}Zr_xO_3$ (x = 0, 0.1, 0.2 and 0.3) sintered at 1473 K. All the images show melt-like features, irrespective of the concentration of added zirconium. The pristine $BaThO_3$ (Fig 5.3(a)) shows formation of larger grains over which small pebble-like grains are present. The typical grain size ranges from ~ 5 to 0.5 μm. The composition, $BaTh_{0.9}Zr_{0.1}O_3$ (Fig 5.3(b)), also showed similar morphology and grain sizes as shown by the pristine $BaThO_3$. This observation indicates, possible coalescing of smaller grains during sintering to form larger grains. The other two compositions, $BaTh_{1-x}Zr_xO_3$ (x = 0.2 and 0.3) show morphology comprising only small granules and the size is around ~ 0.5 μm (Fig 5.3(c) & (d)). Further, for the compositions, $BaTh_{1-x}Zr_xO_3$ (x = 0.2 and 0.3), the grain growth was found to decrease when compared to pristine and 10 mole % zirconium added $BaThO_3$.

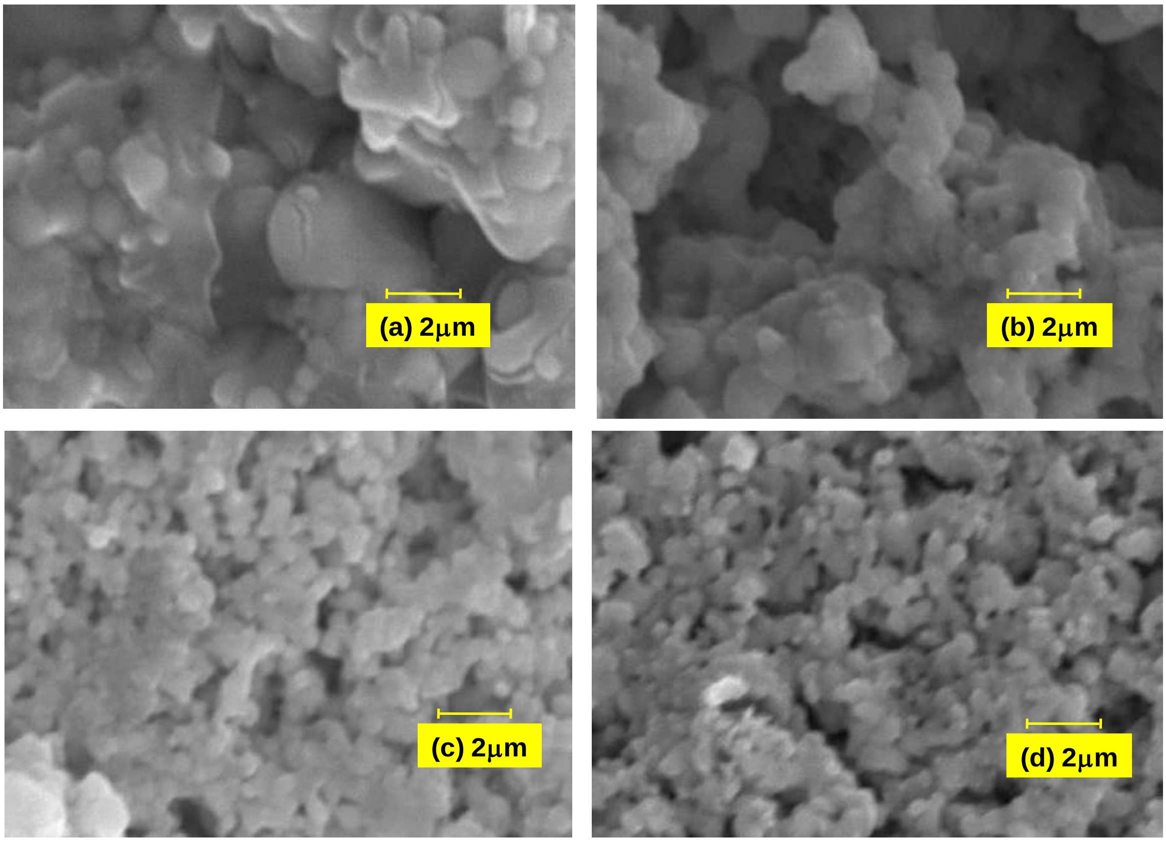

Figure 5. 3 Scanning electron microscopic images of (a) $BaThO_3$,(b) $BaTh_{0.9}Zr_{0.1}O_3$,(c) $BaTh_{0.8}Zr_{0.2}O_3$ and (d) $BaTh_{0.7}Zr_{0.3}O_3$

5.3.2 Electrical Conductivity of $BaTh_{1-x}Zr_xO_3$ (x = 0 - 0.3)

5.3.2.1 In oxygen

Figure 5.4 shows the typical Cole-Cole plot of the sintered pellets recorded in the oxygen atmosphere at 573 K. All the compositions exhibited a single semicircular pattern that can be fitted with an equivalent circuit shown in the inset of Fig. 5.4. The resistances were deduced from the real axis intercept of the trace at low frequency. The resistance of $BaThO_3$ ($5\times10^5\Omega$) was reduced by an order for 10 % of zirconium substitution. However, with further increase in zirconium content (20 and 30%), a gradual increase in resistance was observed.

On introduction of zirconium up to 10 %, the reduction in the resistance was observed compared to the pristine $BaThO_3$, probably due to increase in tolerance factor, which facilitate high conductivity. Further Zr introduction i.e. 20 & 30 % is expected to follow the same trend while compared to the pristine. But, the resistance was found to increase for higher Zr substitution when compare to 10 %, this may probably due to the poor sintering (results pores/voids) of the samples. As zirconium is smaller than thorium, it could hold the oxygen ion more tightly and hence resulting in increased resistance.

From the preceding sections, it was clear that zirconium substituted barium thorates showed low densities. While the conductivity increases with Zr substitution up to 10 %, the same is observed to decrease for the Zr substitution beyond 10 %. It should be noted that the pores/voids present in the sample generally reduce the conductivity. Fonseca et al.[14] reported a decrease in electrical conductivity with increasing porosity in yttria-stabilized zirconia. Thus, for sufficiently dense zirconium substituted composition, it is expected to exhibit higher conductivity than observed in the present studies.

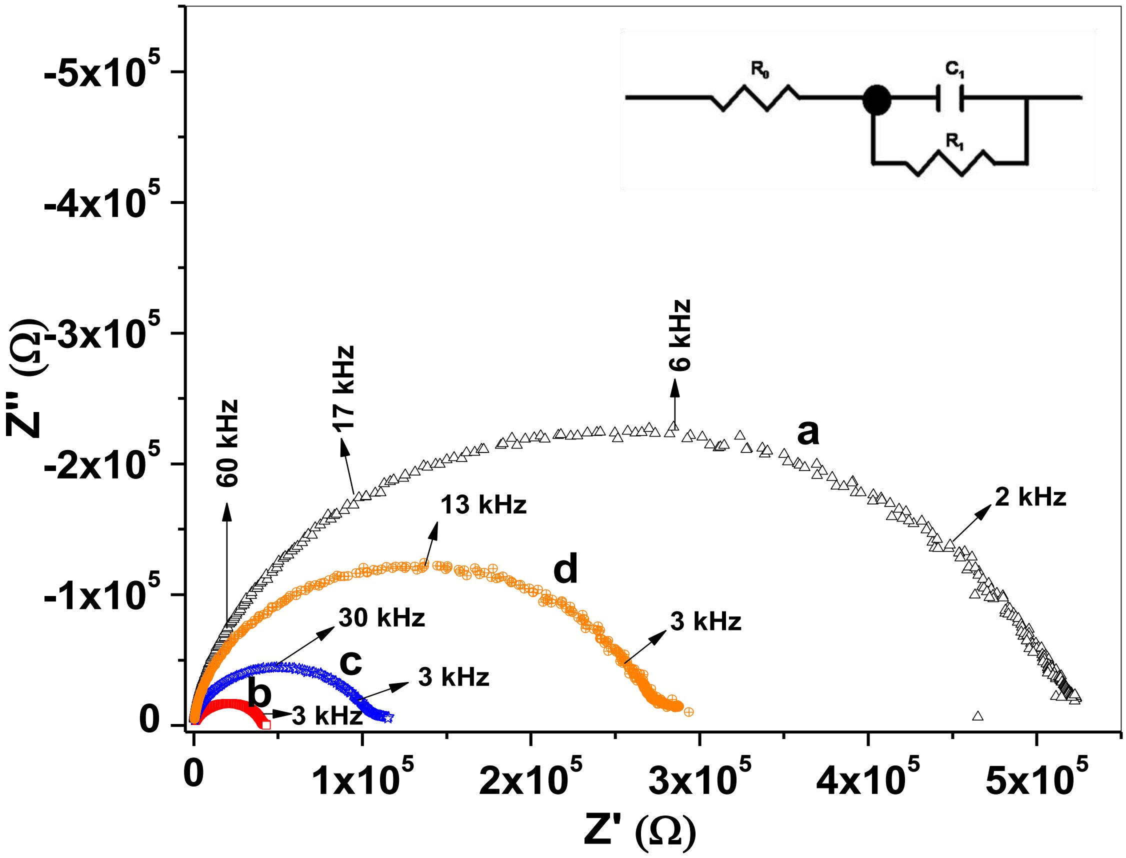

Figure 5. 4 Typical Cole-Cole plots of (a) $BaThO_3$, (b) $BaTh_{0.9}Zr_{0.1}O_3$, (c) $BaTh_{0.8}Zr_{0.2}O_3$ and (d) $BaTh_{0.7}Zr_{0.3}O_3$ in O_2 at 573 K

Figure 5.5 shows the temperature dependent electrical conductivity of $BaTh_{1-x}Zr_xO_3$ (x = 0 - 0.3) in O_2 atmosphere. Zirconium substituted compositions exhibited different slopes for the temperature ranges of 573 – 648 K and 673 – 873 K, whereas a single slope was observed for the pristine barium thorate in the temperature range of 573 – 873 K [15]. On introduction of zirconium, increase in conductivity was observed in oxygen atmosphere for all the zirconium substituted samples in comparison with the pristine compound. The change in slope at two different temperature ranges could be due to change in conduction mechanism. However this could not be established from the present investigation, clearly.

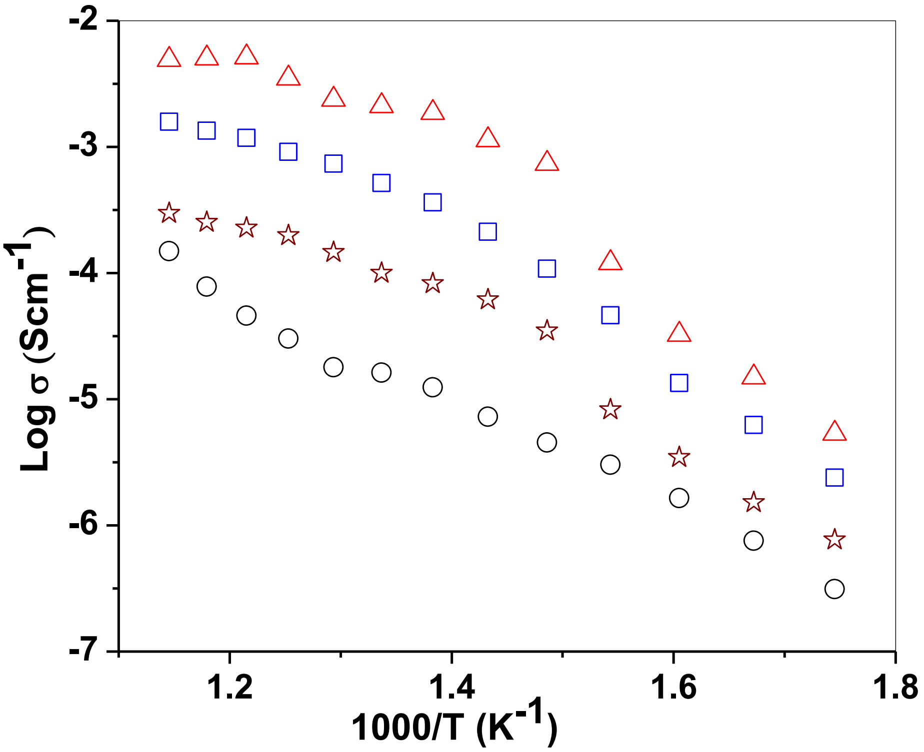

Figure 5. 5 Arrhenius plots for electrical conductivity (○) $BaThO_3$, (△) $BaTh_{0.9}Zr_{0.1}O_3$, (□) $BaTh_{0.8}Zr_{0.2}O_3$ and (☆) $BaTh_{0.7}Zr_{0.3}O_3$ recorded in O_2 in the temperature range from 573 – 873 K. The alternative points are indicating to the cooling and heating cycles

5.3.2.2 In argon containing 80 ppm hydrogen

The variation of the electrical conductivity for the sintered samples as a function of reciprocal temperature in 80 ppm hydrogen in argon is shown in Fig. 5.6. Zirconium addition results two linear regions in semi-log conductivity plot, similar to the oxygen atmosphere. In the temperature range of 573 – 648 K, no significant difference in the conductivities were noticed up to 20 % of Zr-substitution whereas, increase in the conductivity was observed in the temperature range of 673 – 873 K with Zr substitution. As zirconium content is increased to 30 %, the conductivity decreased below that of $BaThO_3$ in the entire range of temperature that may attributed to the precipitation of ZrO_2 phase as observed in the X-ray diffraction studies (Fig. 5.2 (d)).

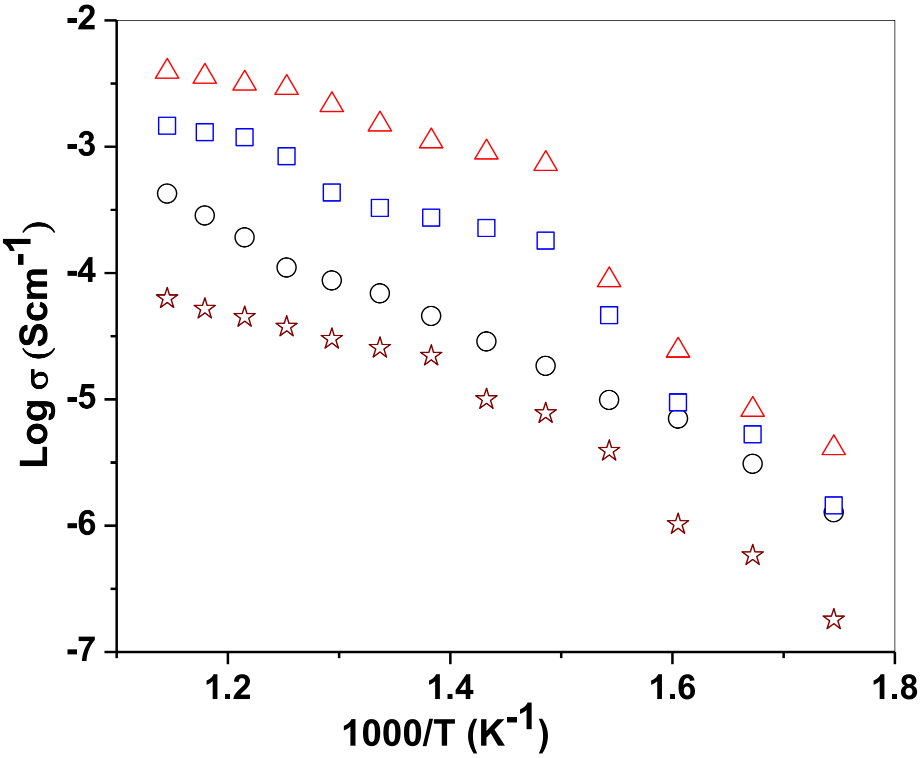

Figure 5. 6 Arrhenius plot for electrical conductivity (○) $BaThO_3$, (△) $BaTh_{0.9}Zr_{0.1}O_3$, (□) $BaTh_{0.8}Zr_{0.2}O_3$ and (☆) $BaTh_{0.7}Zr_{0.3}O_3$ recorded in 80 ppm H_2 in argon in the temperature range from 573 - 873 K The alternative points are indicating to the cooling and heating cycles

5.3.2.3 In hydrogen

Figure 5.7 shows the electrical conductivities of pellets as a function of reciprocal temperature in the presence of hydrogen. Two linear ranges of conductivity were observed viz. 573 – 648 K (low), and 673 – 873 K (high) in semi-log conductivity plots for all the compositions under study. In high temperature region, no significant difference in the conductivity was observed between the pristine and zirconium substituted nominal composition of $BaTh_{1-x}Zr_xO_3$ (x = 0.1 - 0.2). However, the difference in the conductivity is found to be two orders higher for the specimens x

= 0.1- 0.2 than the pristine compound in the low temperature region 573 – 648 K. The decrease in conductivity of $BaTh_{0.7}Zr_{0.3}O_3$ below that of $BaThO_3$ is complementing the observations of the earlier section (5.3.2.2). Introduction of zirconium in place of thorium, the Arrhenius type plots (Figure 5.5 – 5.7) clearly showed the presence of two different regimes of conductivity as a function of temperature namely, low and high conductivity regions 573 – 648 K and 673 – 873 K, respectively. It could be probably due to the involvement of either change in conducting species participating in the conduction process or change in the mechanism of conductivity in the two different regimes. However, more detailed investigations are required to establish the exact conduction species and mechanism. No significant difference in the activation energy for the nominal composition of $BaTh_{1-x}Zr_xO_3$ (x= 0.1 - 0.3) was observed in the atmospheres studied. The consolidated conductivity and activation energy for the conduction process observed for the pristine and all zirconium substituted compound in O_2, 80 ppm H_2 in argon and H_2 are presented in Table 5.1 and 5.2 respectively.

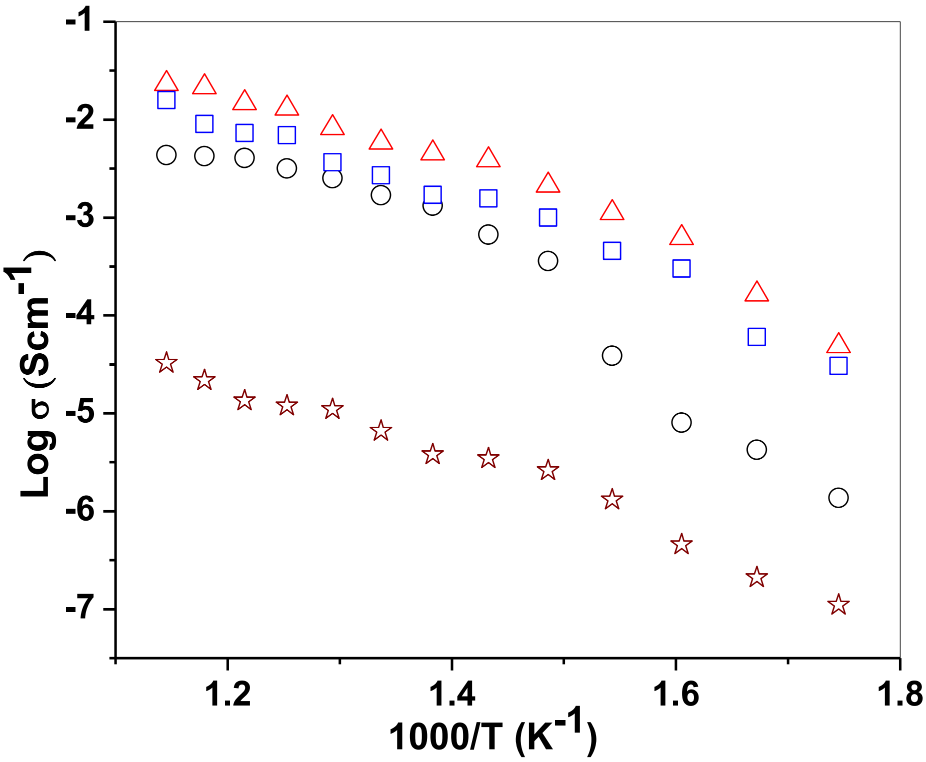

Figure 5. 7 Arrhenius plots for electrical conductivity (○) $BaThO_3$, (△) $BaTh_{0.9}Zr_{0.1}O_3$, (□) $BaTh_{0.8}Zr_{0.2}O_3$ and (☆) $BaTh_{0.7}Zr_{0.3}O_3$ recorded in H_2 in the temperature range from 573 – 873 K. The alternative points are indicating to the cooling and heating cycles

Table 5. 1 Conductivity of nominal compositions, $BaTh_{1-x}Zr_xO_3$ (x=0 - 0.3) in different atmospheres such as O_2, 80 ppm H_2 in argon and H_2

Compound	**Tolerance factor**	**Conductivity (Scm^{-1}) [573 - 873] K [Error ± 0.02%]**		
		O_2	**80 ppm H_2 in Ar**	**H_2**
$BaThO_3$	0.9097	3.13×10^{-7} - 1.49×10^{-4}	1.28×10^{-6} - 4.23×10^{-4}	1.36×10^{-6} - 43.5×10^{-4}
$BaTh_{0.9}Zr_{0.1}O_3$	0.9183	5.34×10^{-6} - 4.89×10^{-3}	4.11×10^{-6} - 3.93×10^{-3}	4.86×10^{-5} - 2.32×10^{-2}
$BaTh_{0.8}Zr_{0.2}O_3$	0.9271	2.38×10^{-6} - 1.57×10^{-3}	1.44×10^{-6} - 1.46×10^{-3}	3.05×10^{-5} - 1.58×10^{-2}
$BaTh_{0.7}Zr_{0.3}O_3$	0.9361	7.68×10^{-7} - 2.98×10^{-4}	1.80×10^{-7} - 6.27×10^{-5}	1.1×10^{-7} - 3.26×10^{-5}

Table 5. 2 Activation energy for the conductivity process exhibited for the $BaTh_{1-x}Zr_xO_3$ (x=0, 0.1, 0.2, & 0.3) in different atmospheres i.e. O_2, 80 ppm H_2 in argon and H_2

Compound	**Ea (eV)**					
	O_2		**80 ppm H_2 in Ar**		**H_2**	
	[573 - 648] K	**[673 - 873] K**	**[573 - 648] K**	**[673 - 873] K**	**[573 - 648] K**	**[673 - 873] K**
$BaThO_3$	0.80 ± 0.01		0.79 ± 0.01		1.36 ± 0.02	0.64 ± 0.02
$BaTh_{0.9}Zr_{0.1}O_3$	1.29 ± 0.05	0.50 ± 0.02	1.31 ± 0.06	0.49 ± 0.01	1.38 ± 0.05	0.61 ± 0.01
$BaTh_{0.8}Zr_{0.2}O_3$	1.23 ± 0.04	0.59 ± 0.02	1.40 ± 0.07	0.59 ± 0.02	1.25 ± 0.08	0.68 ± 0.02
$BaTh_{0.7}Zr_{0.3}O_3$	1.01 ± 0.03	0.53 ± 0.01	1.25 ± 0.05	0.52 ± 0.02	1.05 ± 0.04	0.63 ± 0.02

5.3.2.4 Electrical conductivity versus tolerance factor (t)

The stability of perovskite structure has often been described using Goldschmidt tolerance factor (an estimate of ionic packing) that is defined as,

$$t = \frac{r_A + r_B}{\sqrt{2}\left(r_B + r_O\right)} \qquad (5.1)$$

Where, r_A, r_B and r_O are the ionic radii of A, B and O, respectively. The stability of many perovskites has been successfully expressed in terms of their tolerance factor by Virkar et al. [16, 17]. The tolerance factor is 1.0 for cubic ideal perovskite, whereas, the structural deviations will lower this value. The radius of B-site ion (r_B) is arrived by considering the weighted average of ionic radii of Th and Zr [9]. On introduction of Zr, the tolerance factor gradually increases, from 0.92 to 0.94, compared to the pristine barium thorate, i.e., 0.91. The increase in tolerance factor should have helped in enhancing the conductivity. However, due to the presence of significant void fraction above 10 % addition of zirconium, the conductivity reduces. Figure 5.8 shows the electrical conductivity as a function of tolerance factor for the pristine and Zr substituted samples in three different atmospheres, i.e., O_2, 80 ppm H_2 in argon and H_2. The electrical conductivity in all the atmospheres passes through a maximum at x = 0.1. Nominal composition, $BaTh_{0.7}Zr_{0.3}O_3$ exhibited lower conductivity in the presence of H_2, compared to that of oxygen.

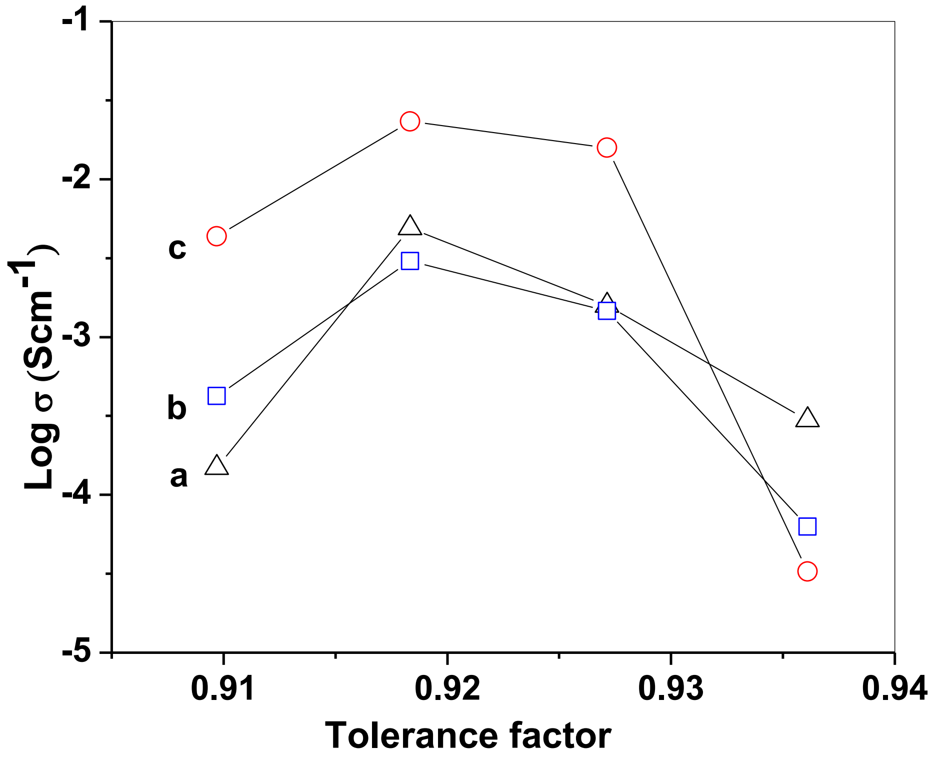

Figure 5. 8 Electrical conductivity as a function of tolerance factor of $BaTh_{1-x}Zr_xO_3$ (x = 0 - 0.3) (a) O_2, (b) 80 ppm H_2 in Argon and (c) H_2 at 873 K

5.3.2.5 Elucidation of hydrogen retention in $BaTh_{0.9}Zr_{0.1}O_3$ matrix

Studies in section 5.3.2.1 and 5.3.2.3 indicated higher conductivity for nominal compositions of $BaTh_{0.9}Zr_{0.1}O_3$ in hydrogen atmosphere than that of oxygen. The hydrogen-exposed samples were equilibrated in oxygen atmosphere as described in section 5.3.2.1, to investigate the regeneration or retrace behavior of conductivity. After the time interval of 24 h, the conductivity was measured in the temperature range from 573 to 873 K with an interval 50 K. Typical conductivity behavior of $BaTh_{0.9}Zr_{0.1}O_3$ [a] (□) in O_2 [b] (○) in H_2 and [c] (☆) during recovery in O_2 (24 h) respectively is shown in Figure 5.9. The conductivity values (☆) obtained after equilibrated in O_2 for 24 h shows almost identical to the values (□) obtained in the initial oxygen measurement. This behavior suggests that the substitution of Zr in barium thorate enchances the conductivity in hydrogen, without incorporation of hydrogen in the matrix, in comparison with the Yb substituted barium thorate as discussed in the section (4.4.3).

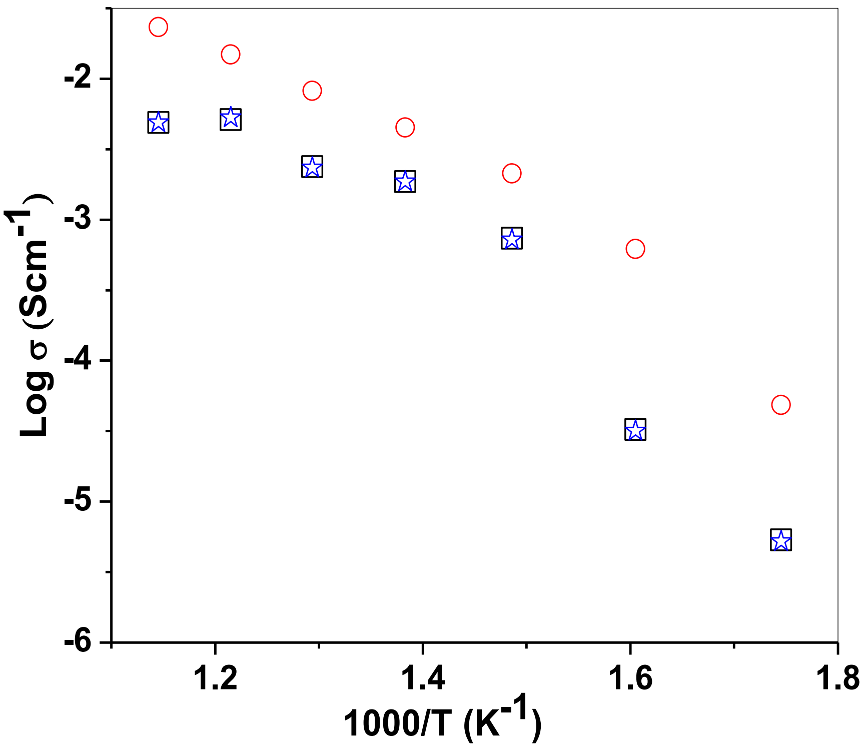

Figure 5. 9 Electrical of conductivity behavior of $BaTh_{0.9}Zr_{0.1}O_3$ in presence of [a] (□) O_2, [b] (○) H_2 and [c] (☆) during recovery in O_2 ambience after 24h

5.4 Chemical stability of $BaTh_{1-x}Zr_xO_3$ (x = 0 – 0.3) in CO_2 atmosphere

Figures 5.10 and 5.11 show the XRD patterns of $BaTh_{1-x}Zr_xO_3$ (where x = 0 - 0.3) after exposure to pure CO_2 for two hours at 673 and 873 K respectively. Typical reaction of a perovskite (ABO_3) with CO_2 is expressed by equation (5.2).

$$ABO_3 + CO_2 \rightarrow ACO_3 + BO_2 \qquad (5.2)$$

The standard Gibbs energies of reaction (ΔG°) between $BaThO_3$ / $BaZrO_3$ with CO_2 are deduced [2, 18] and presented in equations (5.3) & (5.4), respectively.

$$\Delta G^{\circ}_{BaThO_3} = 174\,T - 243200\,J/mol \qquad (5.3)$$

$$\Delta G^{\circ}_{BaZrO_3} = 158\,T - 243200\,J/mol \qquad (5.4)$$

The reaction Gibbs energy changes with the partial pressure of CO_2 (p_{CO_2} ~1.1×10^5 Pa) at 673 and 873 K were calculated for pristine and Zr substituted barium thorate. The calculated Gibbs energies of reaction for $BaTh_{0.9}Zr_{0.1}O_3$ are found to be -116.9 and -82.6 kJ/mol at 673 and 873 K respectively. Similarly, for the pristine $BaThO_3$, it is found to be -126.6 and -91.9 kJ/mol at the temperatures reported [19]. The higher Gibbs energy of reaction for Zr substituted barium thorate relative to that of pure $BaThO_3$ might have probably enhanced the chemical stability against CO_2. The reaction of pristine $BaThO_3$ with CO_2 at 673 and 873 K showed diffraction peaks at $2\theta = 23.94^o$ (111) and 24.29^o (021), which were attributed to $BaCO_3$ as shown in Figures 5.10 and 5.11 (b). However, the effect of zirconium substitution on barium thorates showed different reaction behavior at the two temperatures. While no peak corresponding to $BaCO_3$ was observed at 673 K, the same was observed at 873 K. However, probably due to the limitation of XRD, the peak corresponding to any of the by-products was not observed. As the kinetics of diffusion of CO_2 will be higher at higher temperatures, the decomposition of barium thorates under study at 873 K is more kinetically favorable, as observed by the XRD studies (Figures 5.11 (b – e)).

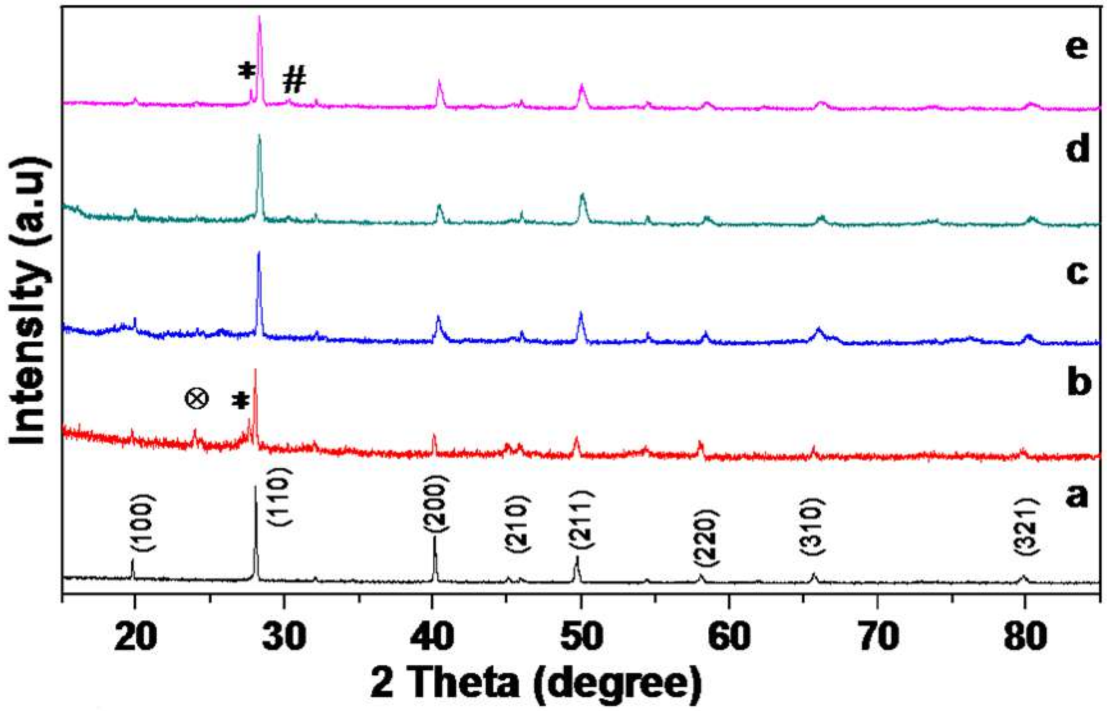

Figure 5. 10 XRD patterns of $BaTh_{1-x}Zr_xO_3$ [(a) as-synthesized, exposed to pure CO_2 (b) x = 0, (c) 0.1, (d) 0.2 & (e) 0.3] exposed to pure CO_2 for 2h at 673 K [⊗ $BaCO_3$ (23.94^o (111), 24.29^o (021)), *ThO_2 (111) and # ZrO_2 (011)]

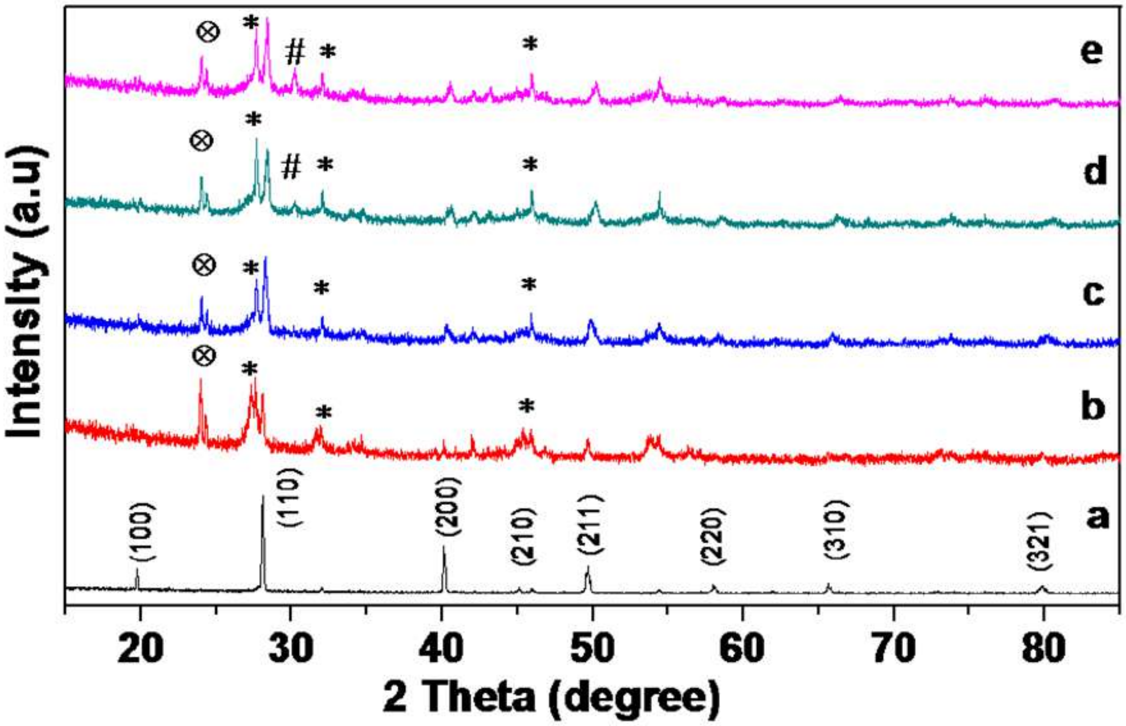

Figure 5. 11 XRD patterns of $BaTh_{1-x}Zr_xO_3$ [(a) as-synthesized, exposed to pure CO_2 (b) x = 0, (c) 0.1, (d) 0.2 & (e) 0.3] exposed to pure CO_2 for 2 h at 873 K [⊗ $BaCO_3$ (23.94° (111), 24.29° (021)), *ThO_2 (111) and # ZrO_2 (011)]

The normalized infrared spectra of $BaCO_3$ and as-prepared $BaTh_{1-x}Zr_xO_3$ (x = 0 - 0.3) are shown in Figure 5.12 (a-e). The asymmetric stretch, in-plane and out-plane bending modes of CO_3^{2-} were observed at 1751.6, 855 and 693.5 cm^{-1}, respectively in all the compositions under study. Figures 5.13 ((i) – (iii)) and 5.14 ((i) – (iii)) show the relative variation in the intensities of characteristic CO_3^{2-} vibrational modes of as-prepared and CO_2 exposed samples (at 673 and 873 K) of $BaThO_3$ and $BaTh_{0.9}Zr_{0.1}O_3$, respectively. The increase in absorption of in-plane and out-plane bending modes of CO_3^{2-} with an increase in temperature in these compositions indicate the formation of carbonate species that complements the XRD spectra of the samples exposed to CO_2 as described earlier in this section. Similar observations were made in other compositions also. The variation of CO_2 interaction at 673 K with increasing Zr-content is shown in Fig. 5.15. It indicates that $BaTh_{0.9}Zr_{0.1}O_3$ has better resistivity towards CO_2 than pristine and 20 % Zr-substituted barium thorate. The exposed sample was ground and measured by ATR. Thus formation of carbonates in the bulk was established. Further, even though $BaTh_{0.7}Zr_{0.3}O_3$ exhibited enhanced resistivity towards CO_2, precipitation of ZrO_2 with the reduction in electrical conductivity (Fig.5.7) makes this composition of little use for the desired application. These studies indicate that the combined effect of ZrO_2 content and reaction temperature dependency on reaction with CO_2.

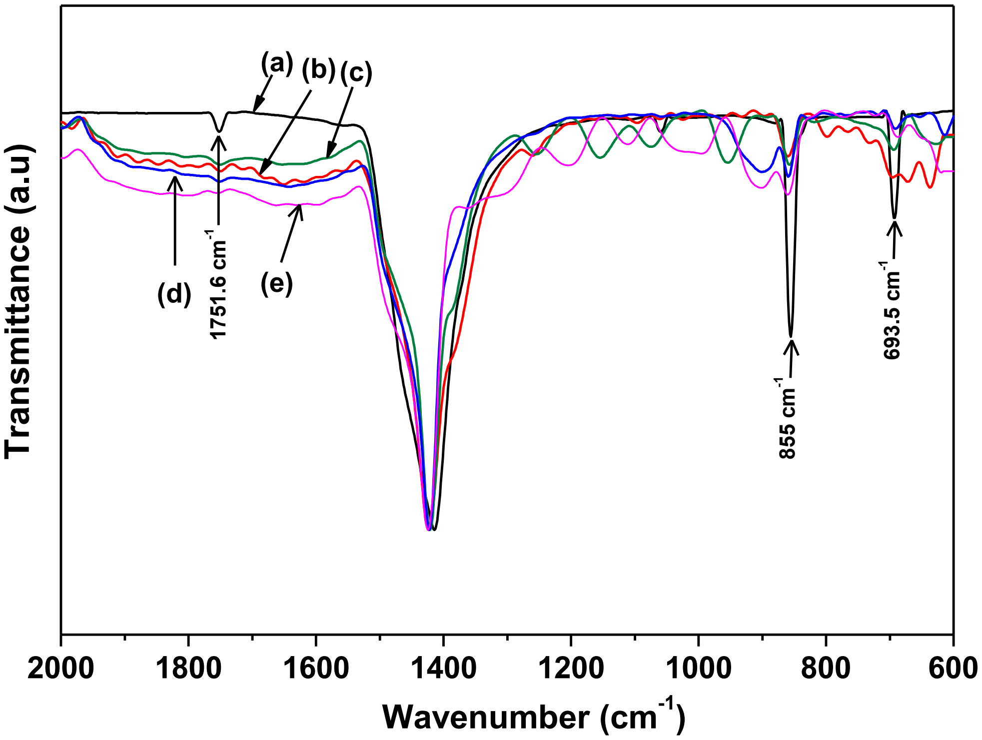

Figure 5. 12 IR spectra obtained for (a) $BaCO_3$, as-prepared (b) $BaThO_3$, (c) $BaTh_{0.9}Zr_{0.1}O_3$, (d) $BaTh_{0.8}Zr_{0.2}O_3$ and (e) $BaTh_{0.7}Zr_{0.3}O_3$

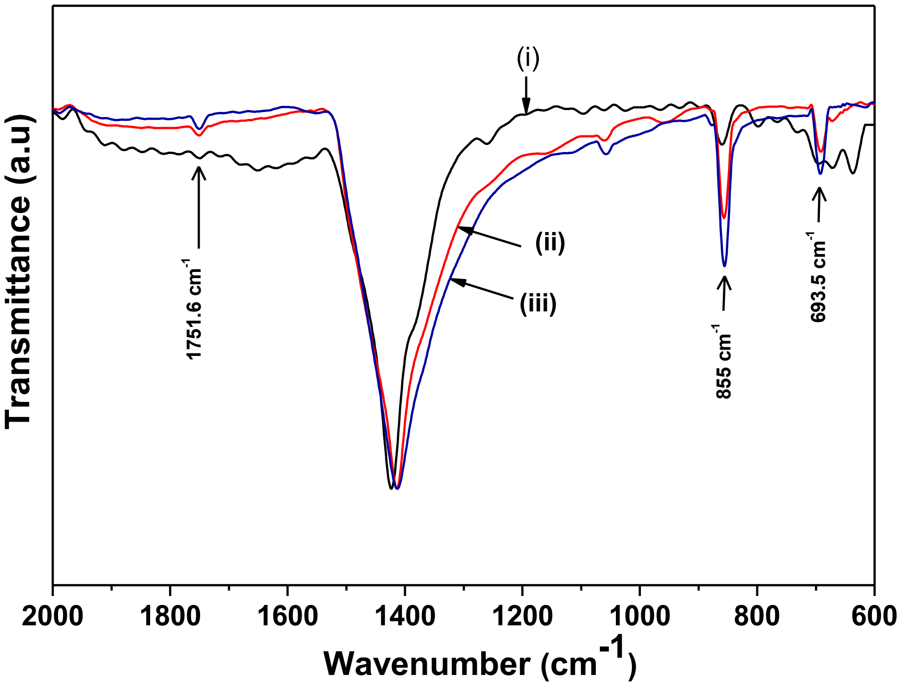

Figure 5. 13 IR spectra of $BaThO_3$ (i) as prepared and CO_2 exposed at (ii) 673 K and (iii) 873 K

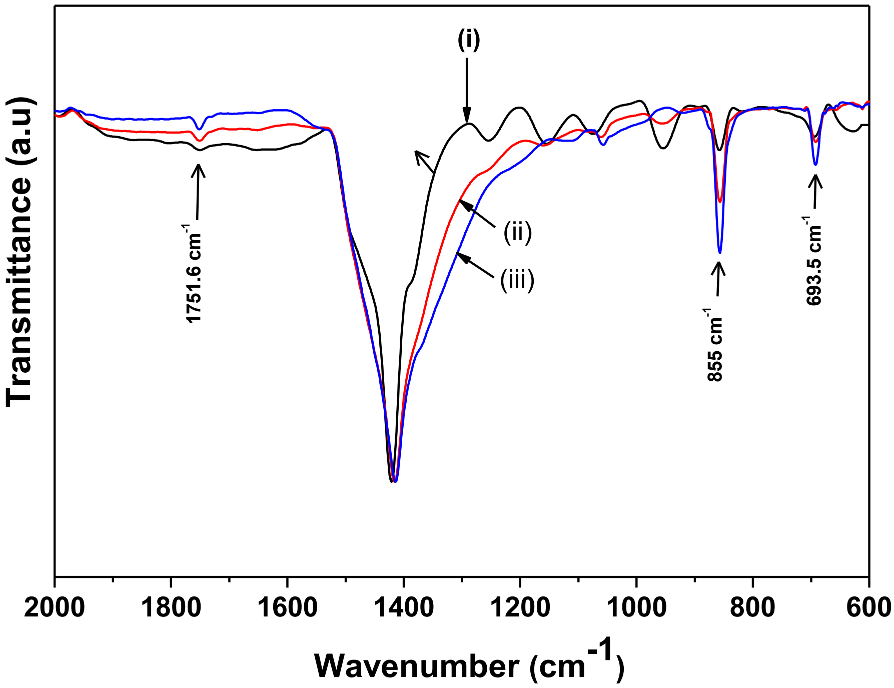

Figure 5. 14 IR spectra of the nominal composition of $BaTh_{0.9}Zr_{0.1}O_3$ (i) as-prepared and CO_2 exposed at (ii) 673 K and (iii) 873 K

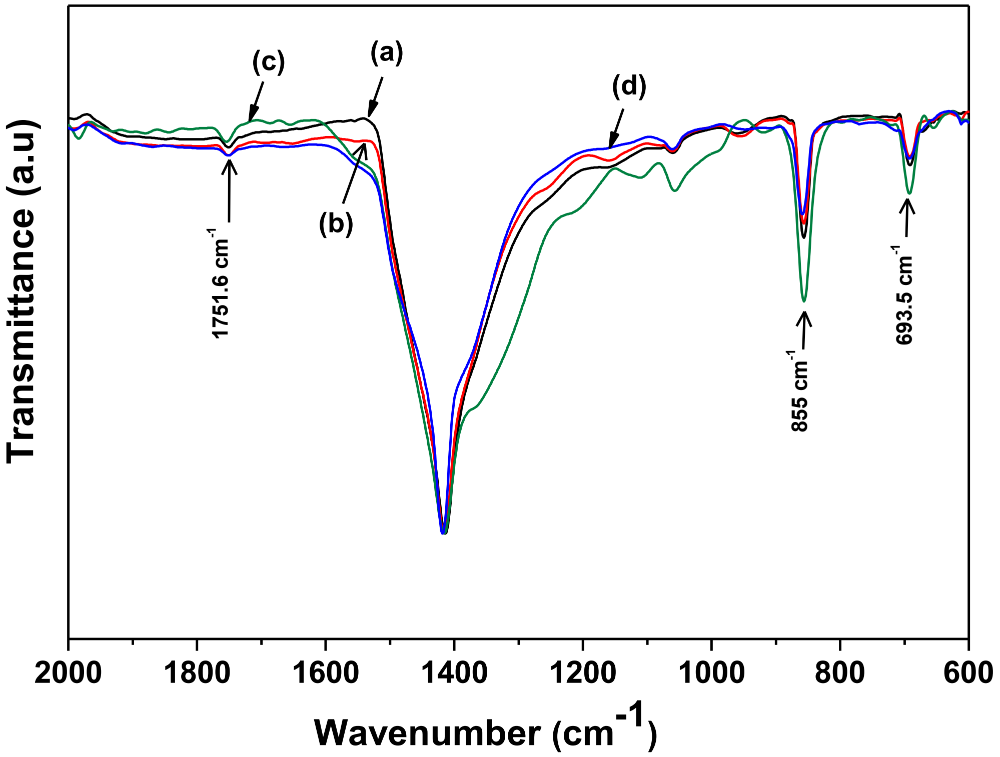

Figure 5. 15 IR spectra for CO_2 exposed (a) $BaThO_3$, (b) $BaTh_{0.9}Zr_{0.1}O_3$, (c) $BaTh_{0.8}Zr_{0.2}O_3$ and (d) $BaTh_{0.7}Zr_{0.3}O_3$ at 673 K

5.5. Conclusions

Zirconium substituted $BaTh_{1-x}Zr_xO_3$ (x = 0, 0.1 & 0.2) was successfully synthesized and reported for the first time. The formation of solid solution of Zr in barium thorate was found to be limited to 20 %. The density and grain size were found to decrease for Zr substituted compounds in comparison with the pristine barium thorate. The conductivity was influenced by the introduction of zirconium in the oxygen atmosphere, which was the highest for the composition, $BaTh_{0.9}Zr_{0.1}O_3$. In hydrogen, there was no significant difference observed in the conductivities between the pristine and Zr substituted compositions. Goldschmidt tolerance factor calculated for the zirconium substituted compositions corroborate well with conductivity values observed. Thermodynamic calculations show relative stability of Zr–substituted barium thorates over $BaThO_3$ in the presence of CO_2 at 673 K, which was also established by experiments. In addition to chemaical stability, Zr substitution helps to increase the conductivity in hydrogen without retrace of hydrogen in the matrix. Zr-incorporation in trivalent substituted barium thorates provides scope for our future work in search of a better proton conducting material for high-temperature applications.

5.6 References

[1] M. Bootharajan, R. Kumar, V. Jayaraman, Synthesis, characterization and electrical conductivity of $BaTh_{1-x}Yb_xO_{3-x/2}$, Ceramics International, 44 (2018) 11172-11179.

[2] K.H. Ryu, S.M. Haile, Chemical stability and proton conductivity of doped $BaCeO_3$–$BaZrO_3$ solid solutions, Solid State Ionics, 125 (1999) 355-367.

[3] K. Katahira, Y. Kohchi, T. Shimura, H. Iwahara, Protonic conduction in Zr-substituted $BaCeO_3$, Solid State Ionics, 138 (2000) 91-98.

[4] N. Taniguchi, C. Nishimura, J. Kato, Endurance against moisture for protonic conductors of perovskite-type ceramics and preparation of practical conductors, Solid State Ionics, 145 (2001) 349-355.

[5] X. Ma, J. Dai, H. Zhang, D.E. Reisner, Protonic conductivity nanostructured ceramic film with improved resistance to carbon dioxide at elevated temperatures, Surface and Coatings Technology, 200 (2005) 1252-1258.

[6] J. Zhang, Z. Wen, J. Han, J. Wu, S. Huang, X. Zhu, Synthesis and characterization of proton conducting $Sr(Ce_{1-x}Zr_x)_{0.95}Yb_{0.05}O_{3-\delta}$ by the citrate method, Journal of Alloys and Compounds, 440 (2007) 270-275.

[7] Z. Zhong, Stability and conductivity study of the $BaCe_{0.9-x}Zr_xY_{0.1}O_{2.95}$ systems, Solid State Ionics, 178 (2007) 213-220.

[8] C. Zuo, T.H. Lee, S.E. Dorris, U. Balachandran, M. Liu, Composite Ni–$Ba(Zr_{0.1}Ce_{0.7}Y_{0.2})O_3$ membrane for hydrogen separation, Journal of Power Sources, 159 (2006) 1291-1295.

[9] R. D. Shannon, Acta acta Crystallographica, A32, (1976) 751-767.

[10] Y. Ohishi, E. Yusnitha, K. Kurosaki, H. Muta, S. Yamanaka, Thermophysical properties of $BaThO_3$, Journal of Nuclear Materials, 448 (2014) 62-65.

[11] R.L. Cook, J.J. Osborne, J.H. White, R.C. MacDuff, A.F. Sammells, Investigations on $BaTh_{0.9}Gd_{0.1}O_3$ as an Intermediate Temperature Fuel Cell Solid Electrolyte, Journal of The Electrochemical Society, 139 (1992) L19-L20.

[12] P. Sawant, S. Varma, B.N. Wani, S.R. Bharadwaj, Synthesis, stability and conductivity of $BaCe_{0.8-x}Zr_xY_{0.2}O_{3-\delta}$ as electrolyte for proton conducting SOFC, International Journal of Hydrogen Energy, 37 (2012) 3848-3856.

[13] T. Schober, H.G. Bohn, Water vapor solubility and electrochemical characterization of the high temperature proton conductor $BaZr_{0.9}Y_{0.1}O_{2.95}$, Solid State Ionics, 127 (2000) 351-360.

[14] F.C. Fonseca, R. Muccillo, Impedance spectroscopy analysis of percolation in (yttria-stabilized zirconia)-yttria ceramic composites, Solid State Ionics, 166 (2004) 157-165.

[15] S.U. Dubal, C.H. Bhosale, L.D. Jadhav, Performance of spray deposited Gd-doped barium cerate thin films for proton conducting SOFCs, Ceramics International, 41 (2015) 5607-5613.

[16] W. Meng, A.V. Virkar, Synthesis and Thermodynamic Stability of $Ba_2B'B''O_6$ and $Ba_3B^*B''_2O_9$ Perovskites Using the Molten Salt Method, Journal of Solid State Chemistry, 148 (1999) 492-498.

[17] S.V. Bhide, A.V. Virkar, Stability of $AB'_{1/2}B''_{1/2}O_3$ - Type Mixed Perovskite Proton Conductors, Journal of The Electrochemical Society, 146 (1999) 4386-4392.

[18] R. Mishra, M. Ali, S.R. Bharadwaj, A.S. Kerkar, D. Das, S.R. Dharwadkar, Thermodynamic stability of barium thorate, $BaThO_3$, from a Knudsen effusion study, Journal of Alloys and Compounds, 290 (1999) 97-102.

[19] I. Barin, Thermochemical Data of Pure Substances, VCh Publishers, Inc, New York, NY (USA), 1995.

CHAPTER 6

Chapter 6: Demonstration of hydrogen separation using $SrZr_{0.95}Yb_{0.05}O_{2.975}$ as proton conducting membrane

6.1 Introduction

An electrochemical hydrogen pump using proton-conducting ceramics is a promising candidate for hydrogen purification. Figure 6.1 describes the operation of the hydrogen pump. When hydrogen gas is supplied to the anode compartment of an electrochemical cell using proton-conducting ceramic membrane and direct current is passed through it, hydrogen is ionized to form protons which are transported to the porous cathode where they get discharged to form hydrogen gas. Thus, only proton is extracted from the supplied gas using this electrochemical pump while the other ionic species in it are not transported through the membrane. Iwahara et al. [1] reported a series of perovskite type oxides which were found to be proton conductors under hydrogen-containing atmospheres at elevated temperatures. Tanaka et al. [2] reported a proton conducting ceramic made out of $CaZrO_3$ as a one-end closed tube and used the same for the recovery of tritium ($^3H_1$), an isotope of hydrogen in the fusion reactor. Hydrogen separation using perovskite-based mixed protonic and electronic membranes were reported [3]. Typical reactions at anode and cathode are expressed as below:

Anode:

$$\frac{1}{2}\,H_2 \rightarrow H^+ + e^- \qquad (6.1)$$

Cathode:

$$H^+ + e^- \rightarrow {}^{1}/_{2}\,H_2 \tag{6.2}$$

In the present work, separation of hydrogen from commercially sourced hydrogen in argon gas mixture was demonstrated using $SrZr_{0.95}Yb_{0.05}O_{2.975}$ as proton conducting membrane. The separated hydrogen was analysed by $Cr_{1.8}Ti_{0.2}O_{3+\delta}$ (at 623 K) based hydrogen sensor [4-6] developed in-house. This chapter presents in details of the conducted experiments and their associated results.

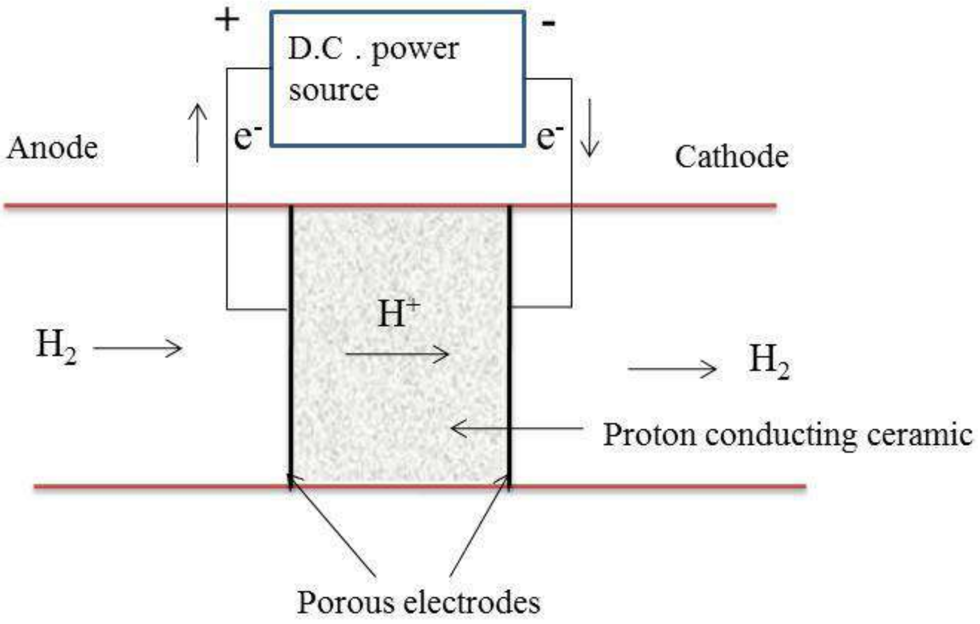

Figure 6. 1 A Schematic of electrochemical hydrogen pump using proton conducting ceramic

6.2 Experimental

6.2.1 Separation of hydrogen from argon

The commercially procured standard argon containing 1500 ppm hydrogen gas was purged and pressurized to ~ 1.2×10^5 Pa in the feed side of the outer chamber as shown in Figure 2.9 and discussed in chapter 2. The measurements were carried out in a static condition by isolating the valves of the outer chamber. The permeate side of the inner chamber was filled with ambient air and the valves were isolated. The temperature of the vessel was programmed to set at 623 ±1 K. The system was allowed to stabilize for an hour at a set temperature. The precision source measurement was connected to anode and cathode of the pumping apparatus and the hydrogen was pumped by sourcing approximately 90 μA current. The pumping was continued till the analysis of separated hydrogen gas at different intervals using home-built hydrogen sensor, as discussed below.

6.2.2 Hydrogen analysis using $Cr_{1.8}Ti_{0.2}O_{3+\delta}$

Chromium titanate with a nominal composition of $Cr_{1.8}Ti_{0.2}O_{3+\delta}$, which is a p-type semiconductor, has been found to be a useful gas sensor material. On exposure of hydrogen to this compound (porous disc, thin or thick film), its resistance changes due to the interaction and subsequent change in electron / hole concentration [4-6]. Samples collected from the experiments on hydrogen separation from argon (section 6.2.1) are presented to this sensor and the hydrogen concentration was evaluated. The sensor output response is in resistance, which was converted to voltage signal by suitable electronics instrumentation module developed in-house [7]. This sensor was used to analyse the separated hydrogen from argon mixture (discussed in section 6.2.1).

6.3 Results and Discussion

The typical response of the hydrogen sensor for corresponding concentrations (55 ppm) was plotted real time against the signal response (Figure 6.2). $Cr_{1.8}Ti_{0.2}O_{3+\delta}$ is p-type semiconductor, whose resistance increases on introduction with hydrogen. The calibration plot for the range of 3 to 75 ppm is shown in Figure 6.3. The background of the permeate chamber was obtained by sampling after an hour at 623 K, to ensure no diffusion of hydrogen when current was not passed. Figure 6.4 shows the response of the sensor, to the sample drawn from the permeate side after passing about 90 μA for a duration of 1 h (0.32 C). It is clear from the response profile of the sensor that about 11 vppm of hydrogen passed through the membrane. Similar exercise was carried out after 5 h of passing 90 μA current, the overall sourced charge was 1.62 C. From the response of the sensor (Figure 6.5), the concentration of hydrogen was found to be 54 vppm. The results are depicted in Table 6.1. These observations show that hydrogen passes through the $SrZr_{0.95}Yb_{0.05}O_{2.975}$ which suggests the feasibility of its separation from argon. Current efficiency was calculated and deduced for hydrogen separation (Table 6.1).

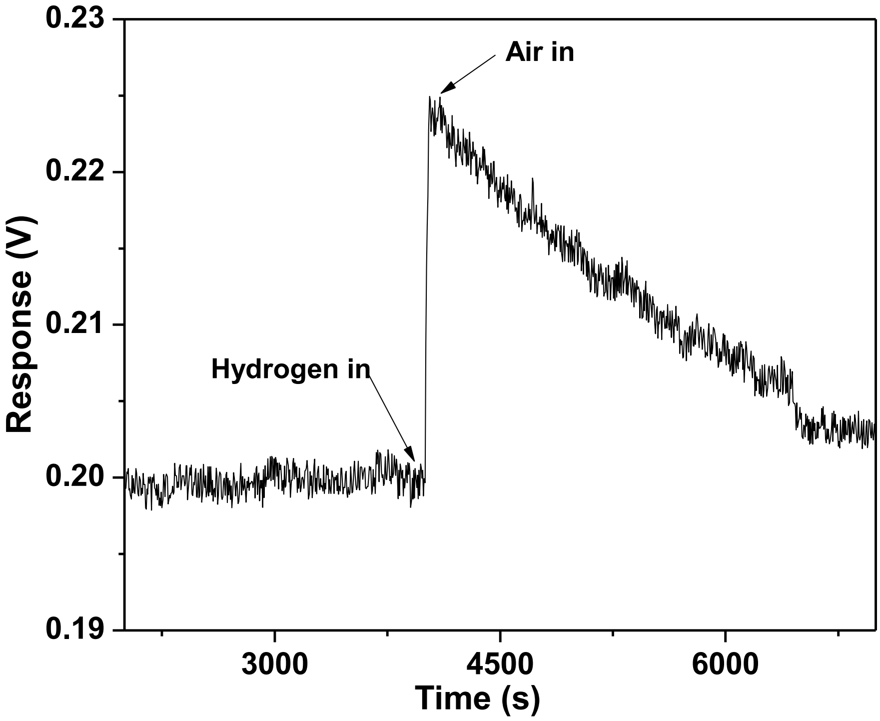

Figure 6. 2 A Typical response of hydrogen sensor ($Cr_{1.8}Ti_{0.2}O_{3+\delta}$ at 623 K) towards 55 v ppm of hydrogen

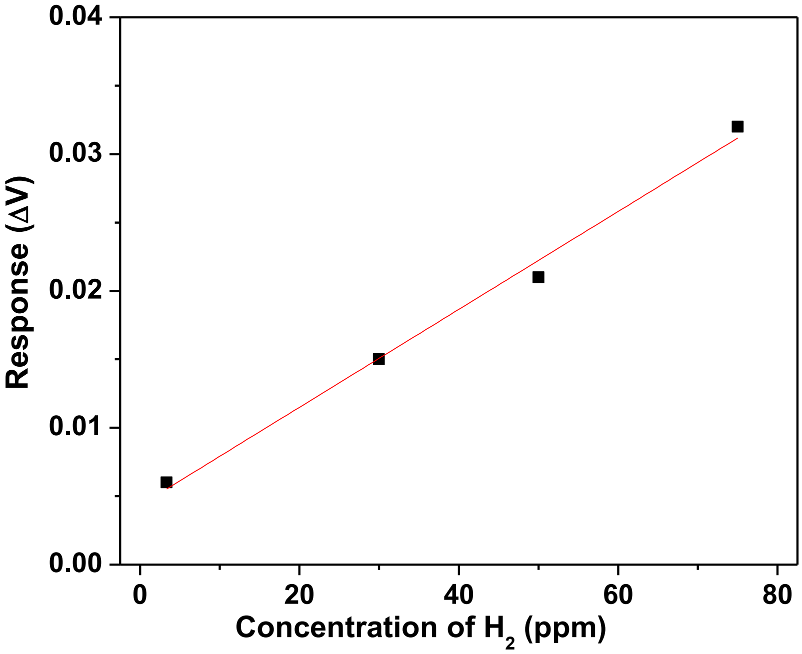

Figure 6. 3 Calibration plot of $Cr_{1.8}Ti_{0.2}O_{3+\delta}$ hydrogen sensor at 623 K

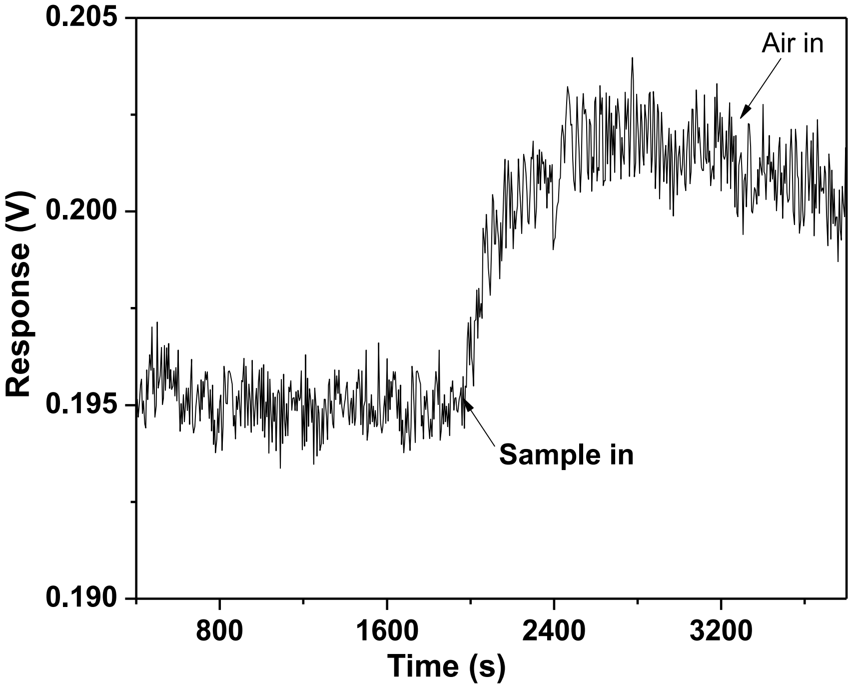

Figure 6. 4 $Cr_{1.8}Ti_{0.2}O_{3+\delta}$ hydrogen sensor (at 623 K) response of the sample after sourcing 90 μA current for 1 h through $SrZr_{0.95}Yb_{0.05}O_{2.975}$ membrane

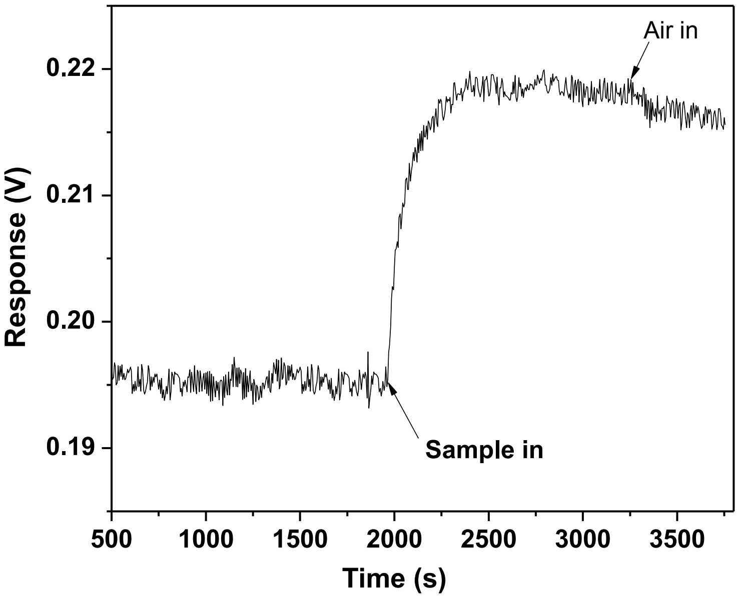

Figure 6. 5 $Cr_{1.8}Ti_{0.2}O_{3+\delta}$ hydrogen sensor (at 623 K) response of the sample after sourcing 90 μA current for 5 h through $SrZr_{0.95}Yb_{0.05}O_{2.975}$ membrane

Table 6. 1 Calculated hydrogen concentrations during pumping for 1 and 5 h intervals at 623 K

Time interval at which the sample is injected during pumping (h)	Charge Passed (C)	$Cr_{1.8}Ti_{0.2}O_{3+\delta}$ hydrogen Sensor Response (ΔV)	H_2 pumped (vppm)		Pumping efficiency (%)
			Theoretical	Experimental	
1st	0.321	0.008	13	11	85
5th	1.62	0.024	63	54	85

6.4 Conclusions

This preliminary investigation has established that $SrZr_{0.95}Yb_{0.05}O_{2.975}$ membrane can be a potential candidate for separating hydrogen from argon. Further investigation on the role of contact area of electrodes, sourcing current, different temperature etc., are expected to lead to more understanding of the behavior of the system.

6.5 References

[1] H. Iwahara, T. Esaka, H. Uchida, N. Maeda, Proton conduction in sintered oxides and its application to steam electrolysis for hydrogen production, Solid State Ionics, 3-4 (1981) 359-363.

[2] M. Tanaka, K. Katahira, Y. Asakura, T. Uda, H. Iwahara, I. Yamamoto, Hydrogen Extraction Using One-end Closed Tube Made of CaZrO3-based Proton-conducting Ceramic for Tritium Recovery System, Journal of Nuclear Science and Technology, 41 (2004) 61-67.

[3] H. Wang, X. Wang, B. Meng, X. Tan, K.S. Loh, J. Sunarso, S. Liu, Perovskite-based mixed protonic–electronic conducting membranes for hydrogen separation: Recent status and advances, Journal of Industrial and Engineering Chemistry, 60 (2018) 297-306.

[4] V. Jayaraman, K.I. Gnanasekar, E. Prabhu, T. Gnanasekaran, G. Periaswami, Preparation and characterisation of Cr2−xTixO3+δ and its sensor properties, Sensors and Actuators B: Chemical, 55 (1999) 175-179.

[5] V. Jayaraman, E. Prabhu, K.I. Gnanasekar, T. Gnanasekaran, G. Periaswami, Soft-chemical preparation and gas sensing properties of iron and manganese substituted Cr1.8Ti0.2O3+δ, Materials Chemistry and Physics, 86 (2004) 165-175.

[6] E. Prabhu, S. Muthuraja, K.I. Gnanasekar, V. Jayaraman, S. Sivabalan, T. Gnanasekaran, Ammonia sensing properties of thick and thin films of Ag6Mo10O33 and Cr1·8Ti0·2O3+δ, Surface Engineering, 24 (2008) 170-175.

[7] E. Prabhu, V. Jayaraman, K.I. Gnansekar, T. Gnanasekaran, G. Periyaswami, Pulsed Laser deposition made thin film sensor for monitoring hydrogen in gas streams, Asian Journal of Physics (2005).

CHAPTER 7

Chapter 7: Summary and conclusions

Research on proton conducting oxides is being carried out since the beginning of the nineties. Perovskites with suitable substitutions are found to be materials with potential applications in the fields such as fuel cells, sensors, separation membrane, etc. This thesis summarizes the results of the synthesis, characterization, electrical conductivity and chemical stability of $CaZr_{1-x}Yb_xO_{3-\delta}$, $SrZr_{1-x}Yb_xO_{3-\delta}$, $BaTh_{1-x}Yb_xO_{3-\delta}$ and $BaTh_{1-x}Zr_xO_3$ in the following sections.

7.1 Behavior of ytterbium substitution in calcium and strontium zirconate matrices

A series of ytterbium substituted calcium zirconates were synthesized via solid state reaction. The solid solubility of ytterbium in $CaZrO_3$ was found to be 10 mole %, and both the pristine and Yb substituted compound were crystallized in orthorhombic phase. Morphological studies showed the well-formed granules and their corresponding size were found to be in the range of 1-5 μm. The electrical conductivity of the pristine and ytterbium substituted compounds were studied in three different atmospheres in the temperature range of 798 - 973 K. There was a reduction in the conductivity for the nominal composition of $CaZr_{1-x}Yb_xO_{3-\delta}$ ($x = 0.01 - 0.1$) in comparison with the pristine $CaZrO_3$. The conductivity was also not influenced by the atmosphere in which the study was performed. The solid solubility of Yb in $SrZrO_3$ was found to be between 1 - 5 %. The pure $SrZrO_3$ showed a well formed dense grain with its varying size of 1-5 μm. On introduction of Yb, a significant reduction in the average grain size to ~ 500 nm was observed. On comparison with pristine, conductivity was increased for ytterbium substituted $SrZrO_3$ and the maximum conductivity was found to be ~ 0.5 $mScm^{-1}$ at 973 K in all the atmospheres studied in these experiments. Retention of hydrogen in the strontium zirconate matrix was established. In nutshell, the present studies reveal, that ytterbium plays a contrasting role in the solid solution formation range, grain growth and electrical conductivity in calcium and strontium zirconate.

7.2 Effect of ytterbium substitution in barium thorate matrix

The pristine and a series of ytterbium substituted barium thorates were synthesized via modified vacuum-aided solid state route followed by under argon flow at 1100 and 1373 K respectively. The nominal composition of $BaTh_{1-x}Yb_xO_{3-\delta}$ (x = 0-0.15) was found to crystallize in cubic phase (Pm3m). The density of the sintered pellets was found to be 95 % of the theoretical densities of these ceramic oxides. The surface morphology studies showed that there was no significant grain growth observed on introduction of ytterbium and all the compositions were found to be highly dense. Typical granule size was found to be in the range of 100-500 nm. The atomic ratio of thorium to ytterbium was semi-quantitatively calculated using EDX and the same were found to be in good agreement with theoretical values. The electrical conductivity was influenced by the introduction of ytterbium and the nominal composition of $BaTh_{0.85}Yb_{0.15}O_{2.925}$ exhibited the maximum conductivity (~1 $mScm^{-1}$) in oxygen atmosphere at 873 K. In hydrogen, the conductivity was found to be higher than that of oxygen and the maximum was found to be ~9 $mScm^{-1}$ for $BaTh_{0.95}Yb_{0.05}O_{2.975}$ at the same temperature. Incorporation of hydrogen / deuterium in the thorate matrix was established by both electrical conductivity as well as infrared spectroscopy analysis for the first time.

7.3 Electrical conductivity and chemical stability of pure and Zr substituted $BaThO_3$

The knowledge on stability of the barium thorate as discussed earlier in section 7.2 is essential for its application in any high temperature process. In the present study a series of zirconium substituted barium thorate were synthesized via modified solid state method. The solid solubility of ZrO_2 in barium thorate was established for the first time. All the Zr substituted compounds exhibit cubic structure. Introduction of Zr resulted, into the reduction of the density and the lowest density was exhibited for the nominal composition of $BaTh_{0.7}Zr_{0.3}O_3$. The larger grain size was observed for pristine and 10 mole % Zr substituted $BaThO_3$. Further, the grain growth was inhibited for other compositions i.e. $x = 0.2$ and 0.3. The conductivity was influenced by the introduction of Zr in oxygen atmosphere whereas no significant difference was observed between the pristine and all the Zr substituted compounds in hydrogen atmosphere. Thermodynamic calculations reveal the relative stability of zirconium substituted barium thorates over $BaThO_3$ in presence of CO_2 at 673 K, which was substantiated by the experiments. Thus, Zr incorporated trivalent substituted $BaThO_3$ can be a better proton conducting material for high temperature applications.

7.4 Demonstration of hydrogen separation using $SrZr_{0.95}Yb_{0.05}O_{2.975}$ as proton conducting membrane

The separation of hydrogen using proton conducting membrane at intermediate temperature is essential for the application, such as purification of hydrogen and its isotope in the nuclear related process. The preliminary study describes ytterbium substituted strontium zirconates as a potential material for the same. The experimentally obtained concentration was comparable with theoretical values. The pumping efficiency was found to be 85% while sourcing current of 90 μA for a duration of 1 and 5 h at 623 K.

7.5 Conclusions

Ytterbium substitution in $CaZrO_3$ and $BaThO_3$ did not lead to any grain growth, while it inhibited the grain growth in the case of $SrZrO_3$. Formation of solid solution in zirconate and thorate matrices follows the order: $BaThO_3 > CaZrO_3 > SrZrO_3$. Ytterbium substitution led to the enhanced electrical conductivity of $SrZrO_3$ and $BaThO_3$, while the same was reduced for $CaZrO_3$. On the other hand, $BaThO_3$ and $SrZrO_3$ matrices with ytterbium substitution showed retention of hydrogen in them. Stability of $BaThO_3$ in carbon dioxide ambience could be achieved by replacing 10 % of Th^{4+} ions by Zr^{4+}. Some of the matrices were found to be potential materials for separating hydrogen from argon.

CHAPTER 8

Chapter-8: Scope for future work

The perovskite based proton conducting membranes possess various challenges for adapting them for a specific application especially for the purification of hydrogen and its isotopes.

8.1 Ytterbium substituted zirconates and thorates

Ytterbium substituted strontium zirconate was synthesized, characterized and its application towards the separation of hydrogen from argon was discussed in the preliminary studies. Hence efforts can be made to improve the pumping efficiency of $SrZr_{0.95}Yb_{0.05}O_{2.975}$ by optimizing the various parameters such as contact area of the electrodes, sourcing current, and temperature for different concentrations of hydrogen in argon.

Similarly, the synthesis and characterization of ytterbium substituted barium thorate was established. The conductivity in hydrogen atmosphere was found to be higher for Yb substituted thorate than that of zirconate matrix. This provides scope for the separation of hydrogen from argon using optimized Yb substituted barium thorate.

It may be a worthwhile effort to investigate the hydrogen retention behaviour of zirconium matrix, while pumping in order to ensure the pumping of hydrogen without loss.

The role ytterbium as Yb^{3+} was considered in various matrices in the present investigations. It may be a worthwhile effort to take up research activities to evaluate the impact of Yb^{2+} on conductivity, in these matrices.

Finally, the above compositions with the optimized parameters can be used to purify the heavier hydrogen isotope $^{3}H_{1}$ from $^{3}He_{2}$, its decay product.

List of Abbreviations and Symbols

A.C	**Alternating current**
atm	**Atmosphere**
ATR	**Attenuated total reflection**
CIF	**Crystallographic file**
EDS	**Energy Dispersive X-ray analysis**
HPGe	**High Purity Germanium detector**
HUP	**Hydrogen uranyl phosphate**
KAMINI	**KAlpakkam MINI**
MSSR	**Modified solid state reaction**
NAA	**Neutron activation analysis**
PEFCs	**Polymer electrolyte fuel cells**
ppm	**Parts per million**
SEM	**Scanning electron microscopy**
SOFCs	**Solid oxide fuel cells**
SSR	**Solid state reaction**
vppm	**Volumetric Parts per million**
XRD	**X-ray diffraction**
YSZ	**Yttria stabilized zirconia**
ΔV	**Difference in vlots**
μA	**Micro amphere**
t	**Tolerance factor**

r_A	**Radius of A site cation**
r_B	**Radius of B site cation**
r_O	**Radius of oxygen**
CN	**Coordination number**
δ	**deficiency**
r_{cri}	**Critical radius**
Å	**Angstrom**
eV	**Electron volt**
Ω	**Resistance**
T	**Absolute temperature**
θ	**Bragg angle**
pm	**Pico meter**
wt. %	**weight percentage**
kW	**Kilo watt**
k_0	**Composite Nuclear constant**